Air Force Institute of Technology
AFIT Scholar

Theses and Dissertations | Student Graduate Works

9-13-2018

Reconstruction of the 3D Temperature and Species Concentration Spatial Distribution of a Jet Engine Exhaust Plume Using an Infrared Fourier Transform Spectrometer Hyperspectral Imager

Mason D. Paulec

Follow this and additional works at: https://scholar.afit.edu/etd

Part of the Optics Commons, and the Propulsion and Power Commons

Recommended Citation

Paulec, Mason D., "Reconstruction of the 3D Temperature and Species Concentration Spatial Distribution of a Jet Engine Exhaust Plume Using an Infrared Fourier Transform Spectrometer Hyperspectral Imager" (2018). *Theses and Dissertations*. 1953.
https://scholar.afit.edu/etd/1953

This Dissertation is brought to you for free and open access by the Student Graduate Works at AFIT Scholar. It has been accepted for inclusion in Theses and Dissertations by an authorized administrator of AFIT Scholar. For more information, please contact richard.mansfield@afit.edu.

www.manaraa.com

Reconstruction of the 3D Temperature and Species Concentration Spatial Distribution of a Jet Engine Exhaust Plume Using an Infrared Fourier Transform Spectrometer Hyperspectral Imager

DISSERTATION

Mason D. Paulec

AFIT-ENP-DS-18-S-025

DEPARTMENT OF THE AIR FORCE
AIR UNIVERSITY

AIR FORCE INSTITUTE OF TECHNOLOGY

Wright-Patterson Air Force Base, Ohio

DISTRIBUTION STATEMENT A.
APPROVED FOR PUBLIC RELEASE: DISTRIBUTION UNLIMITED.

www.manaraa.com

The views expressed in this document are those of the author and do not reflect the official policy or position of the United States Air Force, the United States Department of Defense or the United States Government. This material is declared a work of the U.S. Government and is not subject to copyright protection in the United States.

www.manaraa.com

AFIT-ENP-DS-18-S-025

RECONSTRUCTION OF THE 3D TEMPERATURE AND SPECIES CONCENTRATION SPATIAL DISTRIBUTION OF A JET ENGINE EXHAUST PLUME USING AN INFRARED FOURIER TRANSFORM SPECTROMETER HYPERSPECTRAL IMAGER

DISSERTATION

Presented to the Faculty

Graduate School of Engineering and Management

Air Force Institute of Technology

Air University

Air Education and Training Command

in Partial Fulfillment of the Requirements for the

Degree of PhD, Optical Sciences and Engineering

Mason D. Paulec, B.S.M.E., M.S.M.E.

13 September 2018

DISTRIBUTION STATEMENT A.
APPROVED FOR PUBLIC RELEASE: DISTRIBUTION UNLIMITED.

www.manaraa.com

AFIT-ENP-DS-18-S-025

RECONSTRUCTION OF THE 3D TEMPERATURE AND SPECIES CONCENTRATION SPATIAL DISTRIBUTION OF A JET ENGINE EXHAUST PLUME USING AN INFRARED FOURIER TRANSFORM SPECTROMETER HYPERSPECTRAL IMAGER

DISSERTATION

Mason D. Paulec, B.S.M.E., M.S.M.E.

Committee Membership:

Dr. Michael Marciniak
Chairman

Dr. Kevin Gross
Member

Dr. Benjamin Akers
Member

www.manaraa.com

AFIT-ENP-DS-18-S-025

RECONSTRUCTION OF THE 3D TEMPERATURE AND SPECIES CONCENTRATION SPATIAL DISTRIBUTION OF A JET ENGINE EXHAUST PLUME USING AN INFRARED FOURIER TRANSFORM SPECTROMETER HYPERSPECTRAL IMAGER

DISSERTATION

Mason D. Paulec, B.S.M.E., M.S.M.E.

Approved:

Dr. Michael Marciniak Committee Chair	Date
Dr. Kevin Gross Committee Member	Date
Dr. Benjamin Akers Committee Member	Date

www.manaraa.com

Abstract

The measurement of combustion byproducts is useful for determining pollution of any fuel burning application, efficiency of combustion, and determining detectability of aircraft exhausts. Both intrusive and non-intrusive techniques have been utilized to measure these quantities. For the majority of the non-intrusive techniques, the absorption and emission spectra of the gases are utilized for measurements. For this research, the use of the Telops Infrared Fourier Transform Spectrometer (IFTS) Hyperspectral Imager (HSI) was explored within the scope of combustion diagnostic methods, as an option for remote measurements of a jet turbine to determine concentration of species and temperature of the combustion byproducts. Other current state-of-the-art techniques were reviewed to compare and contrast advantages and disadvantages inherent to them.

Mid-wave infrared (MWIR) measurements of a well-characterized JetCat P-200 turbine engine were made using the Telops IFTS HSI which utilizes a 320 by 256 indium-antimonide (InSb) focal plane array (FPA), calibrated to give a spectral distribution of radiance for each pixel within the image. Measurements were also made using a Santa Barbara Focal Plane (SBFP) IR imager (InSb, 320 by 256 array) that reported integrated radiance values in the MWIR. These measurements were made at varying engine RPM and different nozzle orientations to determine temperature and concentrations of the flow. The use of these radiometric measurements are predicated on good calibrations and quantifying the measurement uncertainty. These calibrated measurements were then used to determine temperatures and species concentrations of carbon dioxide (CO_2) and water vapor (H_2O) produced by the combustion of the Jet-A fuel. The hyperspectral tomography (HT) algorithm, a technique developed for

www.manaraa.com

laser absorption measurements, was used here which combines multiple measurement paths and high-resolution spectral data to determine the temperatures and concentrations of CO_2 and H_2O throughout the volume. To use this algorithm, an absorption and emission spectrum for a given path length, gas concentration, and local temperature must be generated. Spectroscopic databases are employed for this purpose and their application is discussed. The HT algorithms were then used to generate solution sets for six exhaust planes throughout the exhaust flow of a 4 $in.\times$ 1 $in.$ rectangular exhaust nozzle of the JetCat. These were processed on a grid of 0.15-in. spacing based on the measurements made at 2 cm^{-1} spectral resolution. Corresponding local temperature and pressure readings were taken during the tests in order to corroborate the radiometric data. The HT process generated core plume temperature values within ± 35 K of measured thermocouple data for exhaust planes near the nozzle exit plane. Further downstream, turbulent effects of the flow impact the quantity measured by the IFTS HSI. These impacts were quantified and compensated for in multiple approaches in HT algorithms giving ± 35 K measurement agreement for all exhaust planes measured. These 3D temperature and concentration profiles are now able to be used for CFD validation as well as first principle physics models for infrared scene rendering applications.

www.manaraa.com

To Jack White, whose patient teaching reignited my passion for learning

And my wife, whose support enabled this journey

www.manaraa.com

Acknowledgements

To my advisor, Dr. Michael Marciniak, I truly appreciate your patience and guidance through the ups and downs of research and writing. Without your critiques, knowledge, and encouragement, this would not have been possible.

Mason D. Paulec

www.manaraa.com

Table of Contents

www.manaraa.com

Page

www.manaraa.com

Page

www.manaraa.com

List of Figures

www.manaraa.com

www.manaraa.com

www.manaraa.com

www.manaraa.com

www.manaraa.com

www.manaraa.com

RECONSTRUCTION OF THE 3D TEMPERATURE AND SPECIES CONCENTRATION SPATIAL DISTRIBUTION OF A JET ENGINE EXHAUST PLUME USING AN INFRARED FOURIER TRANSFORM SPECTROMETER HYPERSPECTRAL IMAGER

I. Introduction

As the computing power has increased, the prevalence of very capable Computational Fluid Dynamics (CFD) code exists to solve many flow problems. In order to compute a CFD solution, the governing equations, conservation of mass, momentum, and energy are employed, which are discretized at finite grid points to locally evaluate velocities, species concentrations, temperatures, and pressures.[10] In order to correctly compute these quantities, the grid length used for the calculations must be small enough to capture the molecular diffusion, *i.e.* the characteristic length where the inertial forces are balanced by the viscous forces, while still large enough to capture the largest eddies of the system which contain all the energy. The small grid dimension yields a local Reynolds number of unity.[5] In laminar flows with a low Reynold's number, approximations made to reduce the number of computations are often reasonable, while in turbulent flows with high Reynolds number, these approximations are not always accurate. The approximations made require a data set that informs on the spectral, spatial, and temporal content of the turbulent flow.

The analysis of systems which are not well known or easily accessible is another motivator for the measurement of turbulent flows. Some examples are measuring the pollution emitted from industrial smokestacks[14], determining the combustion efficiency from ship exhaust plumes[11], and determining major combustion components

www.manaraa.com

in aircraft exhaust[28]. In these cases, the accessibility of the radiation sources drove the means by which data was collected. In all these, concentrations and temperatures of the byproducts were remotely measured to draw conclusions about the combustion.

For aircraft, measurements of the engine exhaust plumes may be used to indicate their combustion efficiency. Additionally, the exhaust plume affects an aircraft's detectability against distant infrared threats. As such, remote measurements of the plume are relevant for understanding and reducing aircraft vulnerabilities.

To accomplish CFD comparisons and evaluate exhaust plumes in the context of aircraft signature, the byproducts of combustion that make up the plume must be measured. This measurement consists of the species and their concentrations, and temperatures throughout the flow. Intrusive techniques employ sensors placed directly in the flow to measure either species, pressure, or temperature. Often, as is the present case, there is a desire to not disrupt the flow in order to accurately capture the local concentrations and temperatures. For many applications, inserting sensors into the post combustion flow is simply impractical. Exploiting the emission spectra for the different molecules produced in combustion can be useful for this. The molecular rotational-vibrational transitions produce emission lines from H_2O, CO_2, CO, and NO in the infrared (IR) portion of the electromagnetic spectrum.[2] As a result, sensors making these measurements take advantage of these emission bands to detect and quantify these species. The methods discussed in Chapter III employ ways to take advantage of these lines, either through absorption or emission, from the different molecules in the flow.

In this research, an IR Fourier transform spectrometer (IFTS) Hyperspectral Imager (HSI) was used to collect spectral, spatial, and temporal data on a small-scale jet turbine. These data were then used, for the first time, to draw conclusions about the H_2O and CO_2 concentrations and local temperatures throughout the flow by applying

www.manaraa.com

the Hyperspectral Tomography (HT) algorithm. The local temperature distribution agreed well with in situ temperature measurements made during the tests.

To describe this, this document is organized as follows:

Chapter II: Background

Chapter III: Literature Review

Chapter IV: IFTS Hyperspectral Imager Measurements

Chapter V: Radiometric Calibrations

Chapter VI: Spectroscopic Databases and Spectrum Generation

Chapter VII: Hyperspectral Tomography

Chapter VIII: Turbulence Effects On Hyperspectral Tomography

Chapter IX: Conclusion

www.manaraa.com

II. Background

While the hyperspectral measurement and modeling of a representative exhaust plume are the chief aims of this effort, fitting this within the context of aircraft infrared signatures is essential. The contributions due to aircraft plumes are often neglected in approximations. The data collected under this test reveal scenarios in which those assumptions may be invalid. However, the importance of the exhaust plume portion of the infrared signature should be viewed in context of all the signature contributors. To this end, the terminology, signature contributors, measurement techniques, and basic challenges of representing an aircraft signature will first be discussed. Further background regarding IR principles can be found in [32] which is a supplementary text to the electronic warfare (EW) short courses, EW-101 and EW-102, which are taught at the Naval Air Warfare Center Weapons Division (NAWCWD), Point Mugu, California.

2.1 Measurement Application

Capabilities of threat infrared missiles to acquire, track, and inflict damage to aircraft continue to evolve. Additionally, many types of infrared missiles have been widely proliferated around the globe making them a significant lethal threat to US and allied aircraft. All of the services have invested substantially to develop robust countermeasures systems and techniques that improve survivability of aircraft against infrared missiles. The growing complexity and capability of the weapons coupled with the expense of field testing results in an ever growing demand for high-fidelity modeling and simulation.

All simulations of threat missiles and countermeasures start with a signature representation of the aircraft itself. The adequacy of these models to support the simulation

www.manaraa.com

depends on multiple factors including:

1. Spatial fidelity: particularly important at short ranges and for large aircraft. The aircraft is spatially extended and sources are non-uniformly distributed over the surface.

2. Spectral fidelity: aircraft signatures are primarily composed of airframe emissions and reflections, hot-parts emissions, and plume emissions. All have different spectral distributions and consequently propagate through the atmosphere differently. The model should represent the aircraft in both distribution and magnitude of power.

3. Temporal fidelity: important if modeling transient signature effects such as throttle chops and maneuvers.

4. Refresh rate: for purely software based simulations, signature refresh rate is rarely limiting, but for hardware-in-the-loop simulations involving real threat hardware, the signature representation must update at a rate that is real-time to the hardware (typically greater than or equal to (spin rate + carrier rate)*2) to satisfy Nyquist criteria.

Signatures can be measured with high fidelity, and there are multiple physics-based models that can be used to predict signatures as a function of power setting, flight condition, and environmental conditions. Some of the more common first-principles modeling tools include SPIRITS, CHAMP, IRIMAGE (Boeing), SIMIR (Lockheed Martin), FLITES V2, and MuSES. Physics-based models are extremely valuable since they enable realistic signature predictions at many conditions. Models are validated through a process of comparison with high fidelity measurement data.

Previous measurement techniques involved performing spatial/temporal measurements with infrared imagers and spectral/temporal measurements with spectrome-

www.manaraa.com

ters. Utilizing the Telops hyperspectral imager, spectral/spatial/temporal measurements were made of a JetCat turbine engine to collect a much more complete data set. Other instrumentation was utilized for verification of calibration techniques and corroboration of results.

2.2 Aircraft Signatures and Measurements

Signature Contributors.

The signature of an aircraft is a complex combination of direct emissions from airframe, hot engine parts, and plumes, and solar and terrestrial reflections. Signatures vary significantly with aspect angle. Hot engine parts generally dominating in the rear quadrants.

Source signature refers to the emitted and reflected signature at the aircraft. Airframe, engines, and plumes also have unique spectral distributions. Consequently, the signatures of the parts propagate differently through the atmosphere. Figure 1 shows the *apparent* (*i.e.*, as seen through the atmosphere) spectrum produced by hot engine parts and plume.

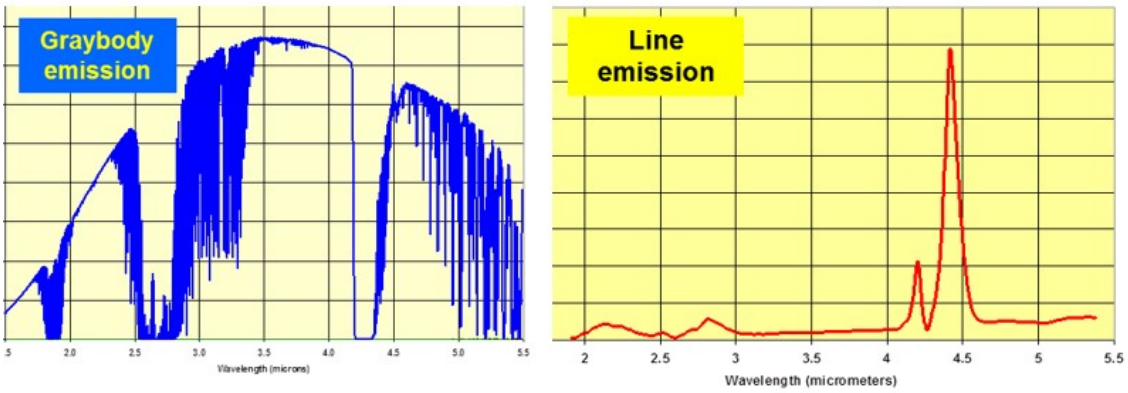

Figure 1: Apparent Spectral Distribution from Hot-Parts and Plume. Emissions from hot parts are graybody or spectrally broad in accordance with Plancks radiation equation. Emissions from plume are spectrally selective, created by molecular motion.

www.manaraa.com

Figure 2 is an atmospheric transmission curve for a standard day at 10kft altitude and a horizontal path of 2kft. As the distance between the attacking missile and the aircraft increases, the absorption regions broaden. In particular, the CO_2 absorption region expands to the long-wavelength side. Since the primary constituents of the plume are CO_2 and H_2O, the range to the aircraft has a significant impact on apparent plume signature. At long distances, especially at low altitudes where the atmospheric is dense with CO_2 and H_2O, the plume is almost completely absorbed. In these cases, the hot metal and airframe, because of their broadband emissions, persist over much longer distances.

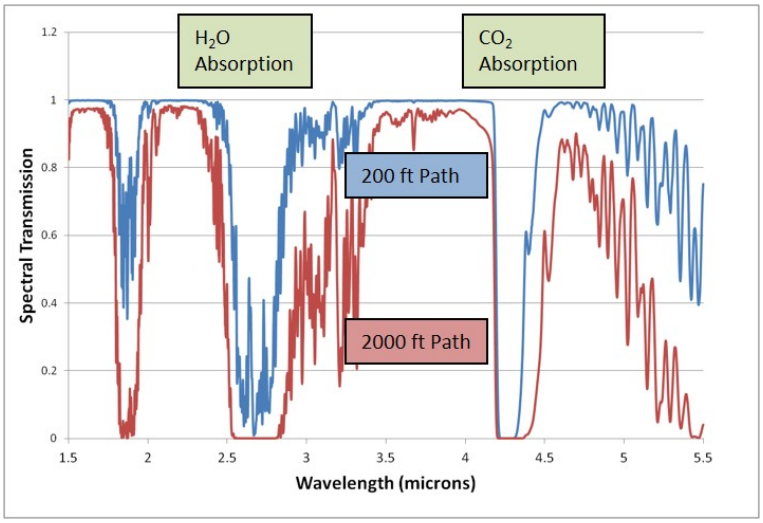

Figure 2: Atmospheric Transmission. As atmospheric path length increases, the carbon dioxide and water vapor absorption regions get broader. Carbon dioxide in particular gets broader to the long wavelength side. The effect of this is that plume diminishes rapidly as a function of distance as seen through the atmosphere.

The *absolute* signature of an aircraft is the sum of the power emitted by and reflected from the aircraft. Although absolute signature includes environmental contributions, it is independent of the background behind the aircraft. *Absolute signature* is always a positive quantity.

Contrast signature is the quantity perceived by a remote sensor. Mathematically, it is equivalent to the difference in the absolute signature of the aircraft and the

www.manaraa.com

intensity of an equivalent area of background. *Contrast* signature may be positive or negative depending on the relative level of the background.

Although real remote sensors perceive sources such as aircraft in contrast against background, signature models are best validated in absolute terms and with absolute measurements.

Real sensors, including missiles and measurement instruments, have non-uniform response in multiple domains. Missiles typically incorporate band-limiting filters to specifically isolate regions of the spectrum. These filters, combined with the inherent non-uniform response of the optics and detectors, weight the power received from a source. The technical term applied to such a case is *effective*. This can apply in other domains, *i.e.*, temporal, spatial. The term is an acknowledgement of the impact of the non-uniform response of the sensor.

Signature, commonly expressed as radiant intensity, is a function of temperature, emissivity, and projected area. Expressed in its ideal form, *radiant intensity* (I) is related to source *radiance* (power per unit area per unit solid angle) (L), projected area (A), *irradiance* (power per unit area at the receiver), and the square of distance.

$$I = L \cdot A = E \cdot R^2 \tag{1}$$

Intensity, *radiance*, and *irradiance* are all spectral quantities. Additionally, atmospheric attenuation, path radiance, source emissivity and reflectivity are all spectral quantities that must be included in the calculation of signature. The total signature of the vehicle is equal to the sum of the signatures of its individual components.

www.manaraa.com

Signature Measurements.

Aircraft signature measurement is a highly complex endeavor and a thorough description is beyond the scope of this effort, but generally the measurement of the vehicle involves a combination of calibrated spectral and spatial instruments. For cases involving rapidly changing temporal events, high sample rate radiometers are often used, but these are rarely required for aircraft measurements. For measurements of a highly spectral and spatially distributed source, like an aircraft exhaust plume, a hyperspectral imager can provide an extremely valuable data set. Each of these types of instruments has its inherent benefits and limitations.

Spatial and Temporal Measurements.

Imaging cameras are highly valuable for measuring the spatial distribution of energy and isolating individual contributors. Typically band-limiting filters will be installed in the camera to isolate specific spectral regions.

Figure 3 shows three different imaging cameras, configured with the filters shown in the figure, provide pseudo-spectral data for the whole aircraft and its parts. The 3.5 to 3.9 micron band provides a means to isolate hot parts emissions in an engine cavity from the plume because the plume does not emit substantially at these wavelengths. The 3.8 to 4.8 micron band is useful for measuring the plume emissions as it encompasses the CO_2 emission spectrum.

Figure 4 shows an image of an F-15A aircraft. When collected at close ranges to minimize atmospheric effects, the imagers provide the ability to isolate signature contributors from background and derive specific signature contributions. This is particularly valuable to support model validation efforts.

www.manaraa.com

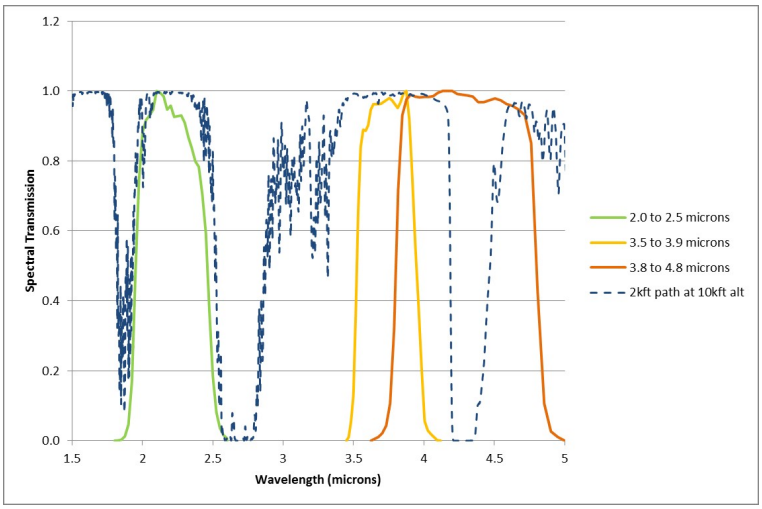

Figure 3: Measurement Bands. Multiple imager bands provide the means to isolate components spatially and spectrally. The 3.5 to 3.9 micron band provides a means to measure hot engine components without plume contamination and minimal solar contributions.

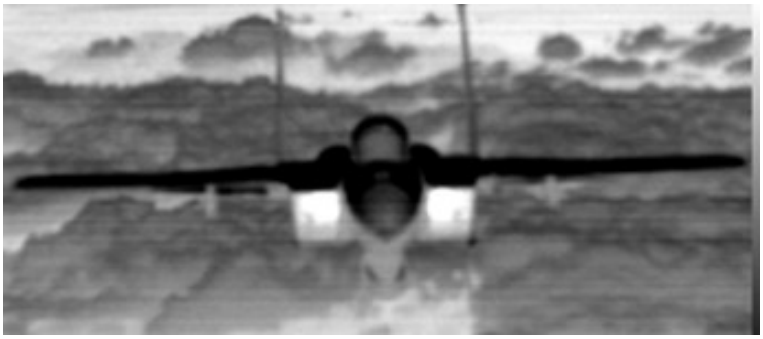

Figure 4: Close-In Imagery of Aircraft. The F-15A is in mixed contrast with the structured cloud background. The upper wing and fuselage areas are in negative contrast due to reflections of cold sky at grazing angles while the intakes stand out in stark positive contrast. Measurements taken at close, highly resolved conditions provide the means to isolate contributions and minimize atmospheric effects.

Spectral and Temporal Measurements.

Spectral instruments are highly valuable for measuring spectral contrast. Spectral instruments offer many benefits for signature measurement activities, but because of their typical highly non-uniform spatial response and relatively low scan rates, they are best used for measurements of high contrast sources that are not widely extended

www.manaraa.com

such as engines and plumes. Additionally, the spectral measurement is the aggregate of everything within the field of view of the instrument. Knowing precisely what lies within the non-imaging device's view can be challenging. In Figure 5, an example spectrum of hot parts and plume can be seen.

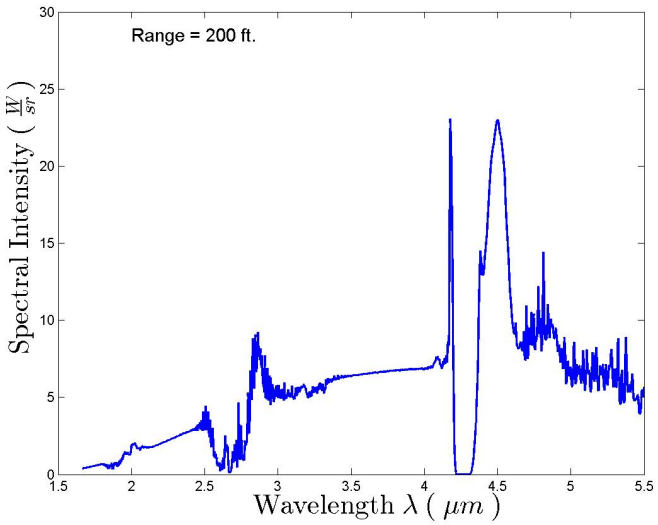

Figure 5: Spectral Measurements. The spectrum here shows the intensity produced by hot parts and plume within the field of view of the spectrometer attenuated by a 200 ft atmospheric path.

Spectral, Spatial, and Temporal Measurements.

Hyperspectral Imagers provide the means to make spatial, spectral, and temporal measurements of a scene. That is, for each pixel of the image (Figure 4 for example), a spectral distribution of radiance is produced (Figure 5). These data are stored in a 3D grid with spatial information in 2 dimensions and spectra in the 3rd. This structure, referred to as a data cube, is stored for each spectral scan. While this instrument is not without limitations, it provides a unique data set that allows for measurements of an exhaust plume that were previously not possible.

By analyzing the spectrum throughout the plume, one can determine concentra-

www.manaraa.com

tions of the species and temperature of the gas at any given point in the flow. This is done by utilizing a database of molecular cross-sections (HITRAN [25], HITEMP [26], and CDSD [31]) and measured path lengths to fit a spectrum to the collected data. Upon doing this fit, the relative intensities of the lines measured will define the temperature of the gas. By knowing the path length through the plume, the magnitude of the lines will dictate the concentration of each species.

With this rich data set, one can integrate the spectra under any band pass to compare with what an imaging camera would observe. Similarly, the spectra in an image can be combined spatially to compare with what a non-imaging spectrometer would measure. This provides the ability to readily compare data sets of different instruments.

2.3 Infrared Signature Models

The ideal aircraft measurement would include a 4π steradian spectral and spatial map of the entire aircraft. Although this is not possible given real-world instrument limitations and budget constraints, it is possible to develop a full spectral and spatial representation of the entire aircraft using a combination of measured data and modeling tools and techniques. For a high fidelity representation of the aircraft signature, the model must faithfully represent the signature in magnitude, spatially and spectrally.

Hard-Body Emission Modeling.

For surfaces on an aircraft, the direct emission is the most straightforward to model and is often used for first approximations to aircraft signatures. By knowing a material's properties, the surface's emission in a certain direction can be calculated

www.manaraa.com

by utilizing the temperature of the surface and Planck's equation,

$$B_\lambda(\lambda, T) = \frac{2hc^2}{\lambda^5} \frac{1}{e^{\frac{hc}{\lambda k_B T}} - 1} \ , \tag{2}$$

where the spectral radiance of a blackbody B_λ, is defined for a temperature T, wavelength λ, the speed of light c, Planck's constant h, and Boltzmann's constant k_B.[20] This is used with a spectral emissivity, dictated by the material's properties, to calculate the hemispherical emission from a given surface. Facetized models of aircraft are used to assign these materials and temperatures to the different surfaces to then be rendered in a scene. Each surface within the model is oriented with a surface (or vertex) normal associated with it for computations. Both the airframe and hot parts within the engine are represented in this way to account for their difference in spectral emission, which is temperature dependent.

Reflections and Atmospheric Modeling.

For opaque surfaces, any irradiance incident on the surface is either absorbed or reflected, conserving energy. The reflectance of a material is a function of both the observation angle and incident angle of irradiance. This reflectance of a surface, and ultimately the source signature of that surface, is dependent on all the incident irradiance over the 2π steradians. For engine cavities, the incident irradiance is primarily due to other hot surfaces within the cavity as well as emissions from the plume. For airframe signature, the primary contributors of irradiance are sky and terrestrial illumination and contributions from plume emission. When the incident irradiance is due to another surface, all these calculations muST be considered for the second surface as well. This multiple-bounce reflection must be continued until the contributions are negligible. All these sources reflected in the direction of the observer dictate the source signature that is rendered.

www.manaraa.com

For the sky and terrestrial illumination, atmospheric codes like MODTRAN[1] are used to generate spectral distributions of radiance. This data is used to determine the irradiance reflected off a given surface based on the orientation of the surface and location of the viewer.

In addition to irradiance incident on the surfaces, an atmospheric code (MODTRAN) is used to propagate a signature from the source to the observer, making it an apparent signature. This accounts for transmission losses as well as radiance from the atmospheric path itself. Because the detectable signal is viewed as a contrast to a background, the code must also include a background radiance to view the signature against.

Plume Modeling.

There are multiple approaches to the modeling of a plume. For the first approach, a wireframe of the plume is constructed as the result of plume modeling code runs or empirical tracing of an actual plume. Spectral content is assigned to each facet based on the assumption that the plume spectral distribution is spatially uniform at all segments of the plume and as a function of viewing angle. That is, only the magnitude changes. Spectral measurements provide the overall distribution of plume energy. For each segment of the plume wireframe, the magnitude of the spectrum is adjusted such that the integrated value matches the equivalent segment measured with a band-filtered infrared imaging camera. Another approach to modeling the plume in a real-time model is fitting the measurement data to an axi-symmetric plume. Geometrically, this is a simplified approach but allows for the radiative transport calculations to be done relatively quickly.

An approach utilizing volumetric plumes that is both spatially and spectrally accurate has been developed that allows for real-time rendering of the scene. The

www.manaraa.com

approach uses OpenGL textures and ray-tracing to render the plume in an accurate way. The volume is populated by a grid of an in-band radiance and absorption coefficients. As a ray enters the volume, Beers law is used to calculate the absorption and emission marching through the plume for each pixel rendered in the scene.

Population of this 3D grid requires multiple measurements, spectral and spatial. The geometry of the nozzle can be used to inform on some symmetry that may exist to reduce the number of measurements. This requirement has motivated the use of the hyperspectral imager to measure a turbine exhaust plume. With multiple hyperspectral views through a high aspect ratio nozzle, flame layer assumptions can be tested and the use of elliptical symmetry in construction of the volume can be evaluated for accuracy. The hyperspectral tomography (HT) algorithm employed by Ma *et. al.* [18] will be employed here as well to reconstruct this volume.

2.4 Hardware-In-The-Loop Application

The data collected by the HSI shows the spectral shift of the plume as a function of position downstream of the nozzle. While the decreasing intensity can be measured in an imager, the spectral difference will affect the propagation through the atmosphere.

With hardware-in-the-loop applications, entire fly-out simulations are performed to evaluate countermeasure effectiveness throughout an engagement scenario. As the missile approaches the target, shorter distances are encountered, where the plume can be a significant contributor to the aircraft signature and must be adequately represented. A representative aircraft signature and its range dependence is illustrated in Figure 6. The same source signature with an exhaust plume temperature of 850K is propagated through a 1000-, 5000-, and 10000-foot atmospheric path. As the path length decreases, the contribution from the plume can be seen more prominently.

In Figure 7, plumes of varying temperature are seen to propagate through the same

www.manaraa.com

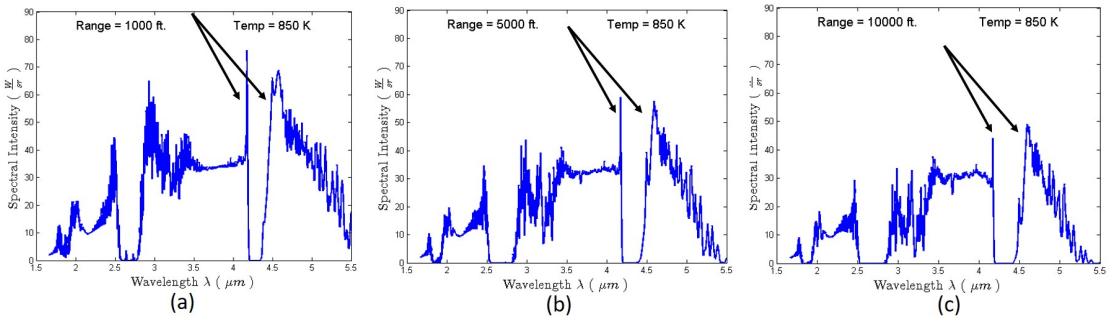

Figure 6: Signature Propagation. A representative aircraft signature with a plume of temperature 850K propagated through a 1000-, 5000-, and 10000-foot atmospheric path. Plume CO2 features are noted with arrows.

atmosphere quite differently. Plume temperatures of 700K to 1000K are propagated through a 3000-foot atmospheric path. This shows the necessity of applying the correct spectral distribution to the different spatial portions of the plume.

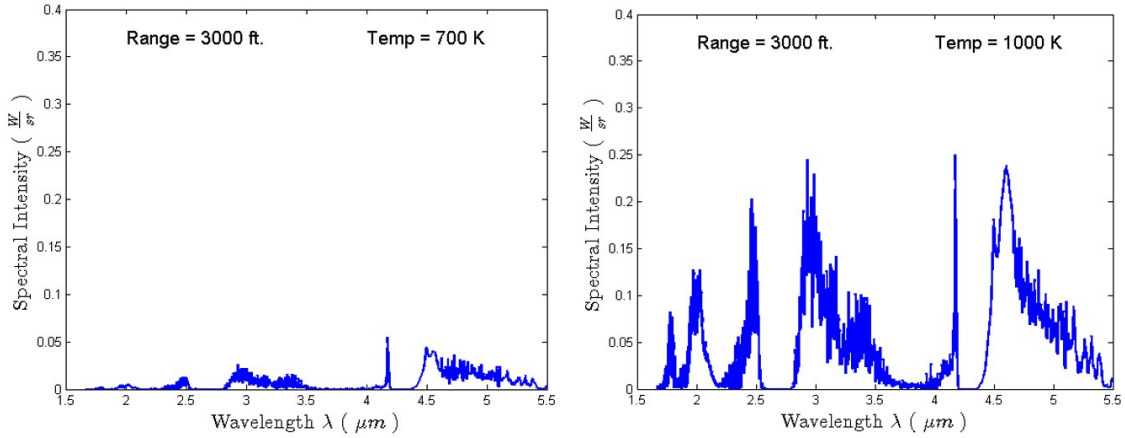

Figure 7: Plume Temperature. Exhaust plume of temperatures of (left) 700K and (right) 1000K propagated through a 3000-foot atmospheric path.

2.5 Background Summary

This chapter has explored the context in which an aircraft exhaust plume is relevant to its overall IR signature. This includes the exhaust plume as a signature contributor, how it is measured, how it is modeled, how it is used in infrared ap-

www.manaraa.com

plications, and the importance of accurately measuring and representing it. With regard to these considerations, a controlled measurement of a representative exhaust plume will be developed and used as a test case to prove reconstruction and representation techniques and the generation of data for infrared scene rendering and CFD model comparison. First current state-of-the-art measurement techniques are reviewed next.

www.manaraa.com

III. Literature Review

3.1 Combustion Diagnostic Methods

The measurement methods used in combustion diagnostics can generally be broken into two classes. In the first, a known coherent monochromatic light source, a laser, is fired through a sample to stimulate an emission that can be measured by a sensor. Conversely, the laser can be directly viewed to measure the amount of attenuation caused by passing through the sample; absorption at this specific wavelength can then be determined. Through the measurement of absorption at multiple wavelengths, the temperature profile can be determined.[29]

In the second class of measurement methods used in combustion diagnostics, the measurement is made by observing the radiation emitted by the gases in the sample. This emission occurs at the same wavelength as the absorption spectra, but the signal measured is now driven by the emission of the gas itself.

Laser-Based Methods.

Lasers may be used to measure both the actual combustion (flame measurements) and the spectroscopy of the byproducts. The laser can be tuned to a wavelength corresponding to the energy level transition of a particular atom or molecule, then swept over a wavelength range at small increments to collect very high spectral resolution data. An advantage with lasers is the intensity can be adjusted to generate a large signal making the detectability of a species easier.

For one of these laser techniques, the laser is used to cause fluorescence in the flame or byproducts. The laser excites an atom or molecule into an elevated state, from which it then fluoresces to a lower energy level (still above the ground state). This fluorescent emission intensity is then detected as a function of the input laser

www.manaraa.com

frequency. This technique is called laser-induced fluorescence (LIF). This approach is then extended to a laser sheet where a 2D image of the fluorescence is then measured. This extension is plane LIF (PLIF). These LIF approaches provide very high collection rates, high spectral resolution, and good signal-to-noise ratio (SNR).[16]

Another laser-based approach that is much simpler in implementation is laser absorption spectrometry (LAS). In this, a laser, again specifically aligned to the wavelength of an atomic or molecular transition of interest, is fired through the sample and collected with a sensor. The difference with and without the sample can provide the data necessary to measure the absorption of that laser line. [16]

Ma *et al.* performed hyperspectral tomography (HT) which utilized three lasers which were tuned to sweep through a wavelength range in the water absorption band of 1346 nm to 1362 nm to directly measure the H_2O absorption spectrum. By scanning the laser at a very fine resolution, over a 10 cm^{-1} band, a hyperspectral data set was captured. Then, a 15×15 grid pattern was set up using fiber optics to measure multiple paths at once. This technique allowed for a 2D plane measurement of H_2O concentrations in the flow; then the apparatus was shifted down stream to collect another plane of data in the exhaust plume of a G.E. J85 jet engine. [19] The laser intensities, I_{abs}, were measured with sensors opposite each laser. By knowing the intensity of the laser source, I_0, the ratio $\frac{I_{abs}}{I_0}$ yields the transmittance, τ, of the path traversed by the laser through Beer's law, [20]

$$\tau = \frac{I_{abs}}{I_0} = e^{-\sigma_{12}(\lambda)\cdot N_1 \cdot L}, \tag{3}$$

where $\sigma_{12}(\lambda)$ is the absorption cross section of a particular energy transition from the ground to an excited state. These cross sections can be obtained through accepted spectral databases such as HITRAN [25]. N_1 is the population of the ground state for this transition and L is the path length through the plume. The concentration of

www.manaraa.com

H_2O can then be determined for a specific path length.

Equation 3 assumes a homogeneous exhaust gas throughout the path L, which is not accurate for turbulent flows. Although, over small enough measurement increments, the exhaust gases can be segmented into layers with the assumption of local homogeneity. This was used to reconstruct the 3D concentrations and temperatures from the 2D measurements performed. A single sensor measurement represents multiple layers of the exhaust gases collapsed along the measurement path. However, when these measurements are performed from multiple viewing geometries, the intermediate values can be determined. Additionally, the hyperspectral nature of the measurements allows for a quicker convergence to a solution to this nonlinear problem with fewer aspects needed in measurements. [18] This is the process of HT discussed in Chapter VII, where it is of particular interest beyond laser-based measurements as the data processing technique used here since it is independent of how the data is collected.

Laser-based techniques are particularly valuable in that they can collect data at very high data rates. Ma *et al.* collected their data at 50 kHz for a given collection plane, simultaneously. [19] Additionally, over a narrow wavelength band, they can collect very high resolution data to be able to resolve the rotational lines within a vibrational transition. This resolution is key to the ability to determine the temperature of the particular species. The relative intensities of the rotational lines collected in the spectra define a temperature of a given species based on the temperature dependent Boltzmann distribution.[2] However, the spectral range over which laser-based methods collect is much more limited for a given setup. The setup and the sensors are tuned to operate over very narrow bands and as such, multiple lasers are often needed to capture different transitions or species. The Ma *et al.* setup required 32 laser beams and sensors to perform multiple different path measurements

www.manaraa.com

concurrently. Even with this, the setup was only collecting one 2D plane of data at a time.

Another major limitation with laser-based techniques is the need to have the laser and sensors near the flow, or even on opposing sides of the flow, which makes many of the applications of laser-based methods impractical where remote sensing is necessary to acquire the data. SNR with laser techniques is not of particular concern as the laser power can be increased for a particular measurement. In directly measuring the emission of the hot gases themselves, it is necessary to have much more sensitive detectors.

Emission-Based Methods.

The degree to which a gas emits is a function of its concentration, the path length through it, and its temperature. As in the laser-based methods, high spectral resolution is of particular importance for combustion diagnostics to resolve emission lines to then calculate concentrations and temperatures of species in the flow. While there are several spectral instruments that utilize these sensitive IR detectors, if sub-wavenumber resolution is desired, their spectral resolutions preclude them. To achieve a better spectral resolution, an IR Fourier transform spectrometer (IFTS) can be employed. [9] The IFTS typically employs a Michelson interferometer in which the incoming radiation is split along two paths and then recombined. One path is then varied so that there is an optical path difference (OPD) that causes the incoming radiation to interfere with itself. At zero path difference (ZPD), the signal is at a maximum as it produces a signal with full constructive interference. This interference pattern, or interferogram, is measured with a detector over time as the moving mirror varies the one optical path. By performing a Fourier transform of the interferogram, the output of the detector is converted into the spectral domain and the source

www.manaraa.com

spectral distribution is arrived at.[9] The operation of the interferometer is important in understanding some of the limitations of the instrument. Of particular interest is with no band limiting filters, the detector is receiving all the radiation within the detector response curve at once. This can impact the sensitivity depending on the source being examined. For example, if the field of view of the sensor includes both a broad band emitter and a spectral emitter, the instrument's sensitivity must be decreased so as not to saturate the detector at ZPD. This limit will then drive the ability of the instrument to measure the spectral emitter.

Solomon *et al.* collected data at 4 cm^{-1} for CO_2, H_2O, ethylene, methane, butane, and acetylene using an IFTS for combustion diagnostics of a laminar ethylene diffusion flame and showed that the IFTS was a viable instrument for collecting data on gases as well as soot particles. They noted the inability to follow turbulent fluctuation with the instrument but showed it was accurate for temperature measurements to $\pm 50K$. [30]

Shafer *et al.* used IFTS emission spectroscopy to perform remote diagnostics of aircraft exhaust plumes in 1995. [27] Dai *et al.* applied these ideas of remote sensing with an IFTS that utilized an IR imager connected to the optics for selecting the target. [8] In 2004, Schafer extended the use to an IFTS that used an azimuth-elevation-scanning mirror to point the interferometer through the scene of an IR imager to collect multiple spectra throughout the gases of an aircraft's exhaust to incorporate a spatial element to the measurement whereby the concentrations and temperatures of the flow at multiple points could be measured. While not concurrent, this provided a better overall picture than was previously possible with an IFTS. [28]

www.manaraa.com

3.2 IFTS HSI

Telops Inc. of Quebec City, Canada introduced their first IFTS HSI in 2004. Their field-portable imaging radiometric spectrometer technology (FIRST) instrument was capable of making spectral measurements for every pixel of an IR detector with a spectral resolution down to 0.25 cm^{-1}. While not without technical challenges, this instrument was capable of collecting credible data.[6] A Telops IFTS HSI sensitive in the MWIR as shown in Figure 8.

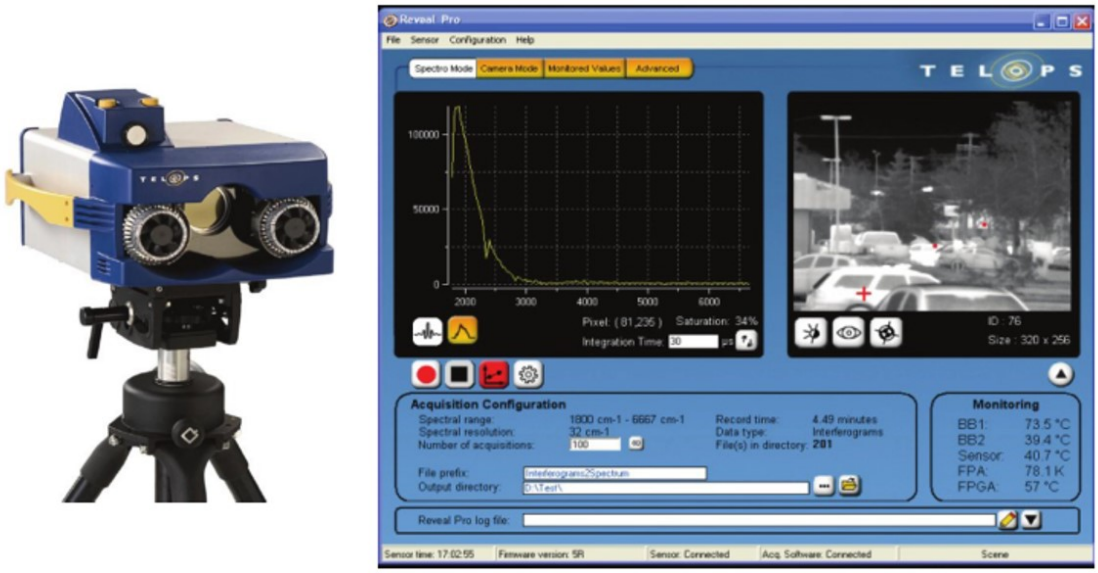

Figure 8: Telops IFTS HSI instrument and data collection.[21]

Gross *et al.* used a Telops IFTS HSI to measure the effluent gases from an industrial smokestack, in which they discussed the process of going from a collected interferogram to a calibrated spectrum, to the concentrations of species and temperatures that, when combined, produce the spectra measured. Beer's Law, Equation 3, was again used over the length of the emission plume to calculate the emission due to the gases. This source signal was then propagated through the atmospheric path to the sensor based on measured atmospherics of the day. For both of these path lengths, a homogeneous path was assumed. In generating the spectra, the line shapes

www.manaraa.com

of each emission line are a function of pressure, temperature, and relative concentration of the gas species. This line shape is used with the line strength to calculate the absorption cross section used in Equation 3 for each emission line. [14] Gross later used this device to track the D.C. offset term in the interferogram to observe the intensity rise and fall throughout the detonation in an internal combustion (IC) engine. This utilized the fact that while the individual frames of data collected do not contain spectral data, the data contained within them can be used to track intensity over time in a given pixel.[13]

To this point, measurements explored the calibration techniques necessary to arrive at calibrated spectra utilizing an IFTS HSI and showed challenges that exist with using it. Moore *et al.* explored one of these challenges by looking at scene change artifacts (SCAs) as the instrument was collecting the interferogram of a turbulent exhaust flow. That is, the source for a given pixel changed by the time the next frame of data was collected. They showed that the stochastic fluctuations in source intensity translate into high-frequency "noise." Temporal averaging of the data cubes collected afforded a significant reduction in noise associated with the SCAs. [21] Harley *et al.* exploited these SCAs when performing a measurement of the exhaust of a G.E. F109 turbofan engine at a spectral resolution of 32 cm^{-1} and at a frame rate of 2.86 kHz. By applying a high-pass spectral filter to the collected interferogram, they were able to isolate the D.C component of the data which contained these intensity fluctuations on a pixel-by-pixel basis. In viewing the entire image, they were able to track the turbulent eddies of the exhaust flow as shown in Figure 9. He collected data at a spectral resolution of 32 cm^{-1} and at a frame rate of 2.86 kHz.[15] While temperature and concentration estimations were not made for this work, it showed how the IFTS HSI could be used to track intensity changes throughout a measurement scene.

Bowen *et al.* applied Moore's noise-reducing techniques to make species and tem-

www.manaraa.com

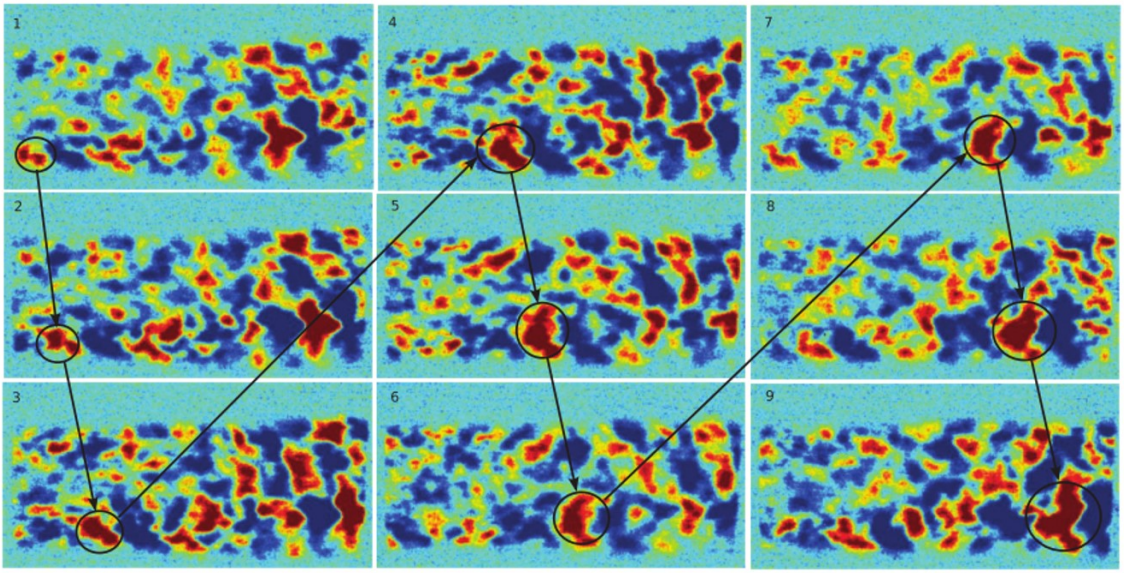

Figure 9: Telops IFTS HSI data collection of a G.E. F109 turbofan engine tracking turbulent eddies.[15]

perature measurements of a small scale jet turbine, in which they were able to assign concentrations and temperatures throughout the flow by using the temporally averaged scans. They locally monitored the temperature of the flow using thermocouples to corroborate the radiometric results, and also showed the effect that fuel types used in the small-scale engine had on CO production.[4]. This showed the direct use of an IFTS HSI as a diagnostic tool of combustion byproducts.

Rhoby *et al.* measured a partially premixed ethylene flame produced on a Hencken burner at varying equivalence ratios, in which they made species measurements of a laminar flame near the base of the flame where a single layer flame assumption could be reasonably made. In generating the spectra to correlate to the measured values, they utilized the HITEMP [26] and CDSD-4000 [31] spectroscopic databases which incorporate values of absorption cross sections at higher temperatures. Rhoby applied these techniques further by adding multiple flame layers to the laminar flame relieving the assumption of homogeneity throughout the flame. [23] This approach is similar

www.manaraa.com

to that used in HT for laser-based methods. However, in Rhoby's approach, an axi-symmetric assumption relieves the need for measurements at multiple aspects.

Gagnon *et al.* used a similar Telops IFTS HSI to measure the combustion efficiency of exhaust plumes of ships, in which they showed the MWIR IFTS HSI allowed for quantitative chemical imaging of ship plumes to characterize their species and efficiency. [11] Gagnon also used both a MWIR and long-wave IR (LWIR) IFTS HSI to concurrently image gas emission of ground sites from an airborne platform in which they collected CO concentrations from an aluminum smelter and H_2O and CO_2 concentrations of a waste incinerator and paper mill. [12]

3.3 Literature Summary

In the field of combustion diagnostics, the absorption and emission spectra of the molecules within the byproducts can be utilized to measure their concentrations and temperatures. Among the available non-intrusive techniques, laser-based methods and interferometer based methods for hyperspectral imaging provide the spectral resolution necessary for the measurement of combustion byproducts. While this resolution requirement is relative to application, the sub-wavenumber range is adequate to narrow these two selections. The laser-based techniques have matured more and are more often employed for single measurements, but the IFTS is certainly at the forefront of hyperspectral imaging techniques. Although not without weaknesses, the Telops IFTS HSI has shown to be a valuable tool for measuring concentrations of species, temperature, and intensity fluctuations. For turbulent flows, the IFTS HSI can be temporally averaged to reduce the noise due to scene change artifacts. Because these methods are often employed by different groups, it appears some of the techniques used in laser-based approaches could be utilized in the IFTS HSI. For example, the algorithms for hyperspectral tomography could be applied to multiple

www.manaraa.com

views of IFTS HSI measurement.

For this research, the IFTS HSI will be used to provide a dense data set on a representative turbine exhaust plume. This data will in turn be used to produce a high fidelity real-time representation of the exhaust plume. By utilizing multiple hyperspectral measurements and the HT algorithms, a first-principle model will be used to reconstruct the temperatures and species concentrations throughout the volume of the plume flow.

www.manaraa.com

IV. IFTS Hyperspectral Imager Measurements

4.1 IFTS Hyperspectral Measurements

In collaboration with Pratt & Whitney of East Hartford, CT and Test Devices Inc. of Hudson, MA, mid-wave IR (MWIR) measurements were made of a well-characterized JetCat P-200 using a Telops IFTS HSI, calibrated to give a spectral distribution of radiance for each pixel within the image. Naval Air Warfare Center Weapons Division (NAWCWD) provided personnel and instrumentation to make measurements using a Santa Barbara Focal Plane (SBFP) IR imager (InSb, 320 by 256 array) that reported integrated radiance values in the MWIR. These measurements were made at varying engine RPM and different nozzle orientations to determine temperature and concentrations of the flow. The different orientations allow for the determination of the degree of asymmetry in the flow in two dimensions. The spectral information from these measurements was utilized to determine temperature and species concentrations of CO_2 and H_2O produced by the combustion of the Jet-A fuel. Using the HITRAN and CDSD-4000 databases of molecular cross-sections and measured path lengths to fit a spectrum to the data, values were determined for every pixel of the hyperspectral imager. Corresponding local temperature and pressure readings were taken in order to corroborate the radiometric data.

4.2 Jet Turbine Measurements

JetCat P-200 Description.

The JetCat P-200 was modified from its standard configuration by adding a mixing chamber and high-aspect-ratio nozzle to create the desired flow field at the exit. The nozzle was a custom manufactured high-aspect-ratio nozzle with a rectangular $4\ in. \times 1\ in.$ inch exit-plane cross-section opening. The JetCat P-200 used Jet-A fuel

www.manaraa.com

with five percent Aeroshell Turbine Oil 500 by volume added for bearing lubrication. Static pressure ports were placed near the exit plane on the nozzle as well. These modifications are shown in Figure 10.

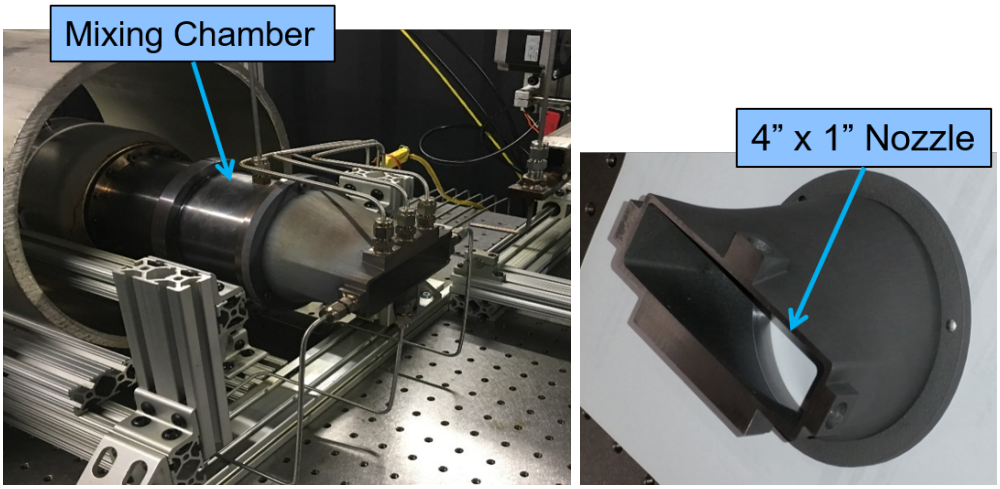

Figure 10: The JetCat P-200 turbine engine mounted to an optical table operating in an indoor facility by TDI of Hudson, MA. A mixing chamber and high aspect ratio nozzle with a rectangular 4x1 inch opening were added to the standard engine.

Instrumentation and Setup.

To characterize the exhaust flow of the JetCat turbine, sensors were placed outside the JetCat container to protect them from the vibration, contaminates, and temperature changes within the container. The exhaust plume was viewed through a port cut in the side of the JetCat container. The radiometric sensors were placed on a rotation stage for measurement repeatability and ease of calibration. Two blackbody sources were used between each measurement to calibrate the gain and offset of the sensor. By using a known low and high temperature source, the raw counts of the sensor were converted to radiometric units. This is depicted in Figure 11.

The Telops IFTS HSI had approximately a 25-degree field of view. The imager was calibrated to give a spectral distribution of radiance for each pixel within the image. This calibration requires two known radiometric blackbody sources to map

www.manaraa.com

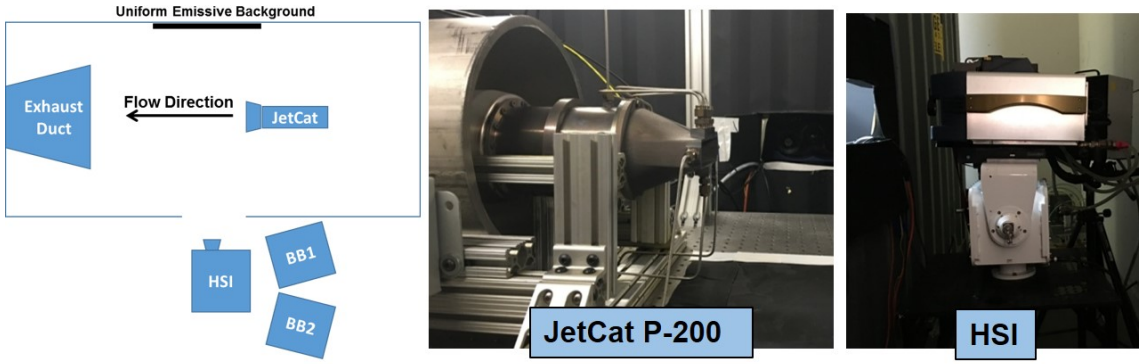

Figure 11: Instrument Setup. The measurement sensors were placed outside the engine container and viewed through a port in the side. Blackbody sources were positioned for the sensor calibration.

the response of the detector for each wavelength measured by each pixel. Data were collected at 2-cm^{-1} resolution which required approximately 1 second per data cube. For each power setting, 100 scans were collected to get a good statistical variation.

The SBFP IR imager utilized a cold filter to limit the response from 3.8 μm to 4.8 μm to focus on the emission due to CO_2. With a 50-mm lens, this imager had approximately an 11-degree field of view and collected frames at 180 Hz. Similar to the HSI, this imager was calibrated utilizing the two blackbody sources to give an in-band radiance value per pixel. One of these images collected with the JetCat turbine operating at 112,000 RPM can be seen in Figure 12 (a) and (b). These images can be averaged over time to give a mean flow. In Figure 12 (c) and (d), 1000 frames have been averaged together to produce the images presented. From this, the standard deviation can be calculated to show the fluctuations of the exhaust gases throughout the flow field.

Local temperature and pressure readings were taken for four RPM settings of the JetCat turbine throughout the flow-field in order to corroborate the radiometric data. These data provide a 3D grid of values from the exit plane to approximately 4.25 inches downstream. Figure 13 shows the setup used for these measurements.

www.manaraa.com

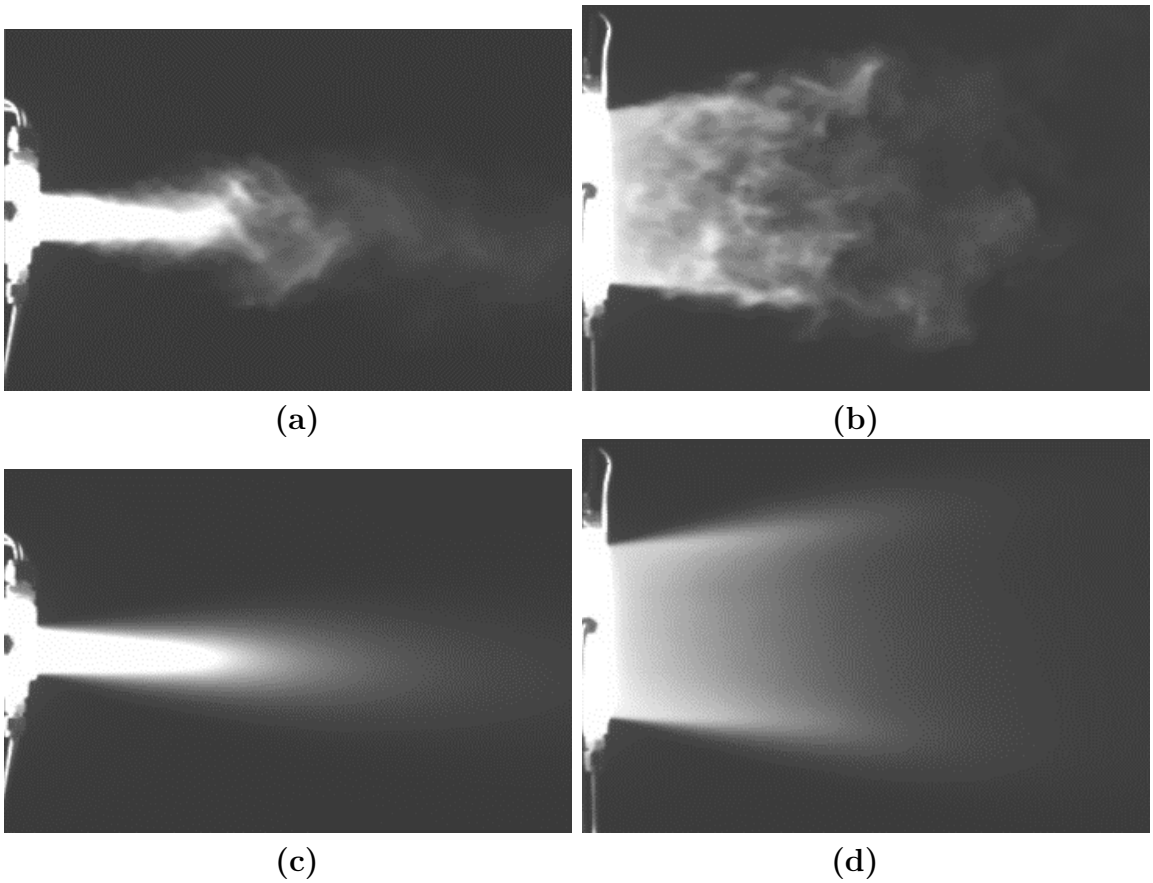

Figure 12: Imager Data. (a) and (b) A single image of data collected at two aspects from the SBFP Imager. (c) and (d) These images are a time average of 1000 frames from the SBFP Imager.

SBFP Imager Data.

The temperature data were collected on a three dimensional grid using a Pitot/static and total temperature probe (United Sensor, Inc.). The tube was mechanically varied through the flow to collect the horizontal slices of temperature seen in Figure 14. The data are from the center-plane from when the JetCat turbine was operating at 112,000 RPM (maximum power).

www.manaraa.com

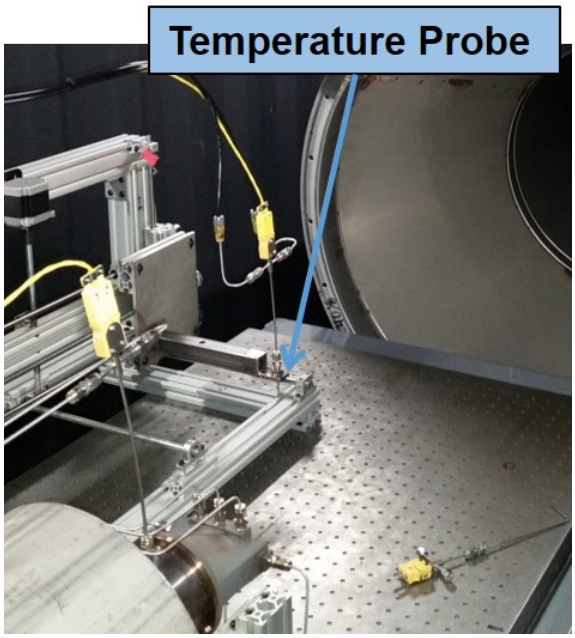

Figure 13: Temperature measurements were performed throughout the exhaust flow-field.

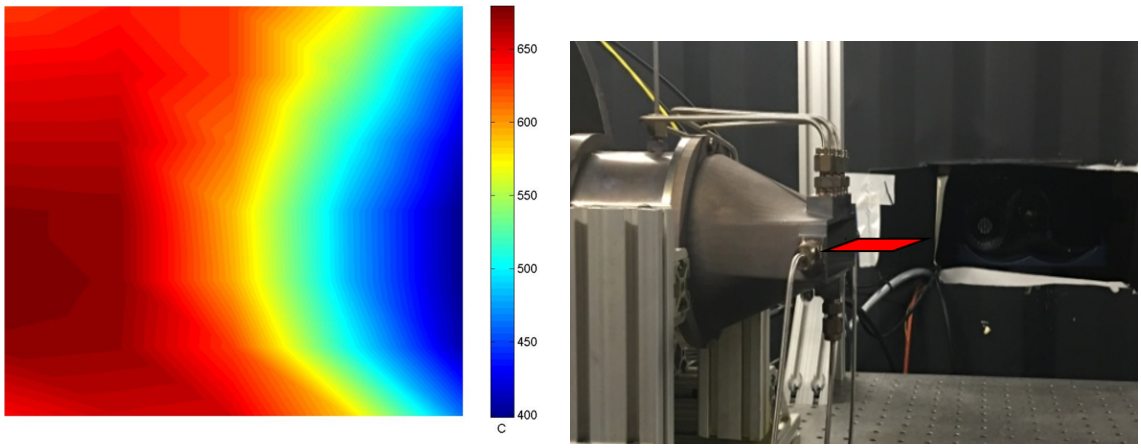

(a) **(b)**

Figure 14: Temperature Data. (a) These temperature profiles show the measured points through the center plane of the JetCat exhaust. (b) The plane of measurement is depicted.

Hyperspectral Data.

The spectral information from these measurements will be utilized to determine temperature and species concentrations of CO_2 and H_2O produced by the combustion

www.manaraa.com

of the Jet-A fuel for every pixel of the HSI. These data provide detailed information for the construction of a volumetric representation of the flow and also about turbulent eddies of the exhaust gases.

The HSI data was collected and stored in data cubes which when calibrated represent an entire spectrum of data for each pixel on the array. The spectral radiance collected for each pixel can then be analyzed. In Figure 15 (a), a portion of the spectrum spanning part of the CO_2 emission spectrum was added together. In Figure 15 (b), the spectra for the selected pixels in Figure 15 (a) are shown; the CO_2 emission spectra is shown to change as a function of the position down stream in the flow. The intensity and spectral distribution are influenced by the temperature and diffusion of the flow. These characteristics are important to correctly represent an exhaust plume.

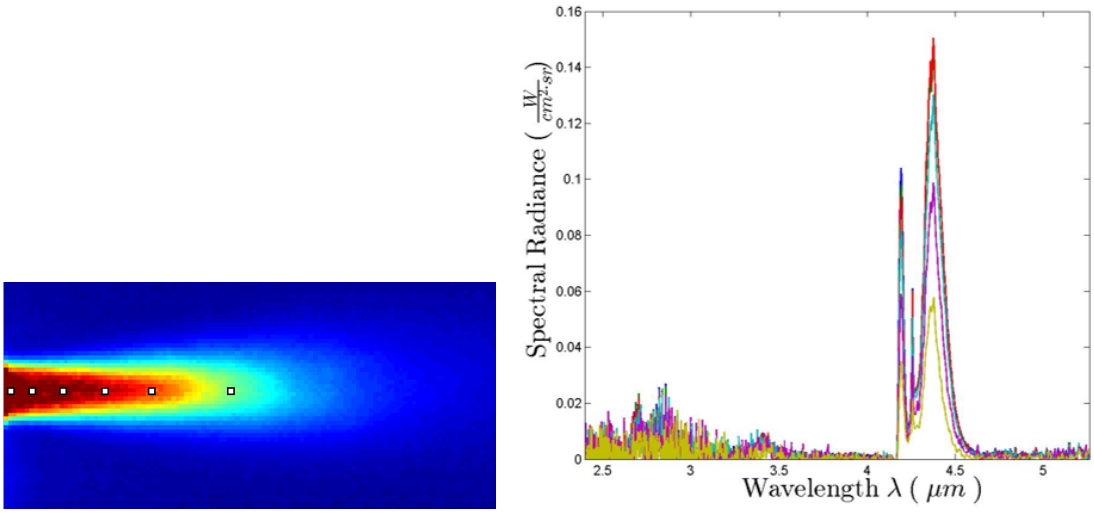

(a) **(b)**

Figure 15: Hyperspectral Data. (a) This image shows a band integrated image of a portion of the data cube. (b) This image shows the spectra collected for each of the pixels selected in (a).

www.manaraa.com

4.3 HSI Data For Plume Model Development

The spectral, spatial, and temporal data collected by the HSI can be used to populate a volumetric representation of the plume. Having the concentrations of species and temperature data as a function of position enables rendering of a plume that fully represents the plume characteristics. By measuring multiple aspects of the plume, the gradients measured in one direction inform on the data collected from the other. The layers of the plume that collapse into a measured pixel can then be determined thus reconstructing the volume that produced the measurement.

4.4 Summary of Measurements

The large amount of instrumentation available for the JetCat testing resulted in data, with sufficient calibration, consistent with physically expected values. The initial analysis of the data collected showed consistent results and good agreement between instruments. In Figure 16, the data collected from the Imager and HSI have been calibrated to radiometric units ($W/sr/cm^2$) as will be discussed in Chapter V. The HSI data cube was integrated under the spectral response of the infrared imager so a radiance comparison could be made. The (a) imager and (b) HSI are on the same radiance scale and the (c) percent difference is plotted as well. Because the instruments have different spatial resolution, a bi-quadratic interpolation was used to put the data on the same grid spacing for comparison. In this difference plot, the noise floor for the two instruments is substantially different so where there is little signal from the exhaust gases, the percent error is very large. The average percent difference of measured plume radiance was less than 5% which speaks well to the measurement devices, calibration techniques, and the repeatability of the engine setup.

www.manaraa.com

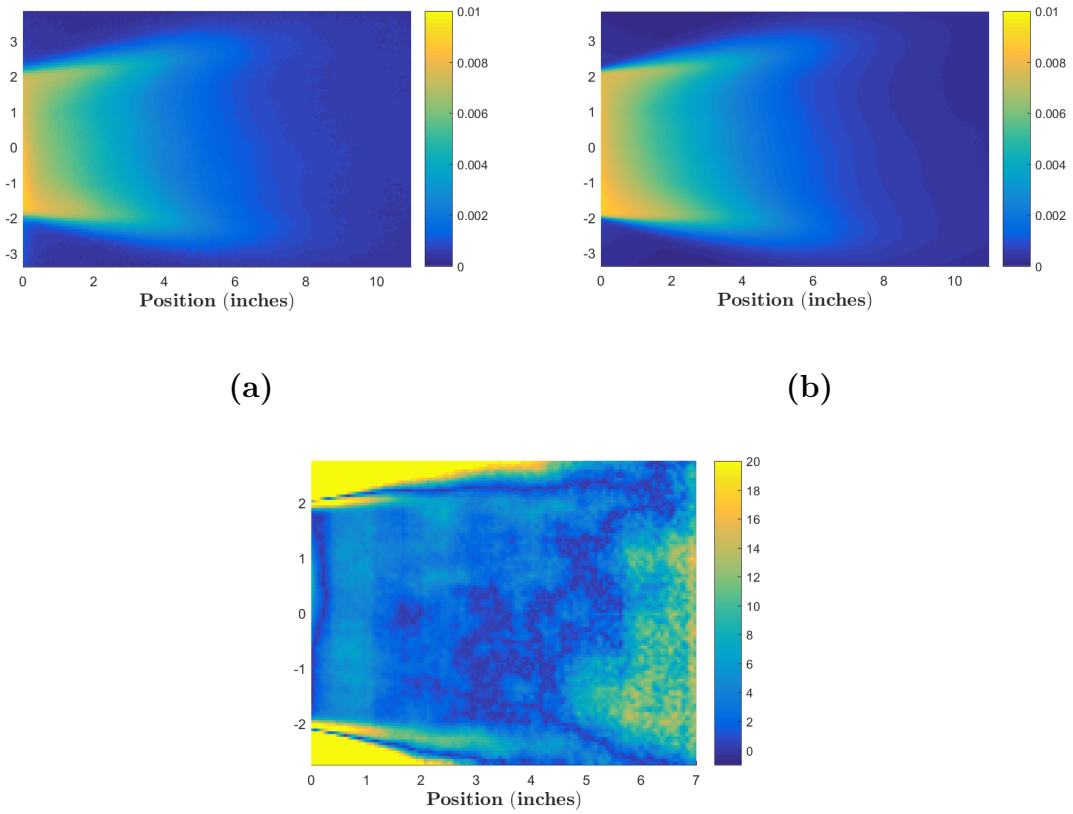

(a) (b)

(c)

Figure 16: Imager and HSI Comparison. Radiance plot of the (a) HSI, (b) Imager, and (c) the percent difference between them.

www.manaraa.com

V. Radiometric Calibrations

5.1 Introduction

In order to use the radiometric data collected for the JetCat P200 exhaust plume, careful calibration of each instrument is necessary. Data collected from infrared imagers and spectrometers are reported in raw digital counts. These count values are generated by converting an analog signal received by the instruments detector to a digital value determined by the gain, bias, and integration time of the detector. To make use of this digital data, calibration is necessary to connect a digital count value to a radiometric quantity. This chapter will show the methodology to radiometrically calibrate data from an IR imager and IFTS HSI. Instrument drift, noise, dark current, and radiative contributions from optical elements can make this endeavor a significant challenge. The errors caused by these quantities will be quantitatively assessed.

5.2 Calibration Approach

Calibration is performed by assigning a radiometric value to a digital count value collected by an instrument. In order to make this connection, a know source of radiation must be accessible. By completely flooding the field of view of an instrument with a known source and neglecting atmospheric influence and instrument response, the radiance on the detector can be correlated back to the radiance of the source. For black-body radiators, this spectral radiance is a function of its temperature through Planck's radiation law

$$B_\nu(\nu, T) = \frac{2h\nu^3}{c^2} \frac{1}{e^{h\nu/(k_B T)} - 1} \ , \tag{4}$$

www.manaraa.com

where ν is the frequency, c is the speed of light, T is the Temperature, k_B is Boltzmann's constant, and h is Planck's constant. As the temperature increases this curve grows in magnitude and its peak shifts towards shorter and shorter wavelengths. This change is depicted in Figure 17.

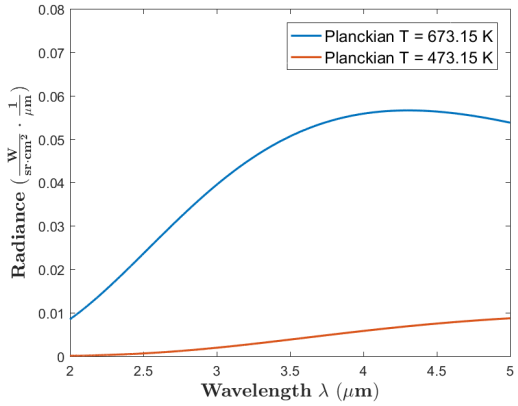

Figure 17: Planckian radiation curves at varying temperatures showing spectral shift and magnitude due to temperature.

This radiance is affected by attenuation through the atmosphere, path radiance and the instruments response curve. For an imager, the response curve defines how it responds to radiation at specific wavelengths. It is a combination of optical element response curves, detector response, and any wavelength limiting filters that may be placed in the optical path. With these taken into account, the Planckian radiation can be used with these considerations to calculate the radiance the instrument is seeing. This approach is taken for both imaging instruments as well as spectral instruments. For imagers, the calculated radiance is spectrally integrated for comparison with measurements. For a non-imaging spectrometer, the scene is spatially integrated over the field of view of the instrument and is calibrated spectrally. For imaging spectrometers, each pixel is treated as a narrow field of view spectrometer and thus each pixel has a spectral calibration.

www.manaraa.com

5.3 SBFP Imager Calibration

For an infrared imager, this radiation is spectrally integrated so that all the radiation that falls within the instrument's response is reported. No discrete wavelength information can be gathered from the instruments output, however the imager provides spatial resolution. The radiance that an imager will observe is

$$L(T) = \int_{-\infty}^{\infty} [\varepsilon(\nu) \cdot B_\nu(\nu, T) \cdot \tau_{atm}(\nu) + L_{path}(\nu)] \cdot R(\nu)\ d\nu\ , \tag{5}$$

where $\varepsilon(\nu)$ is the blackbody spectral emittance, $\tau_{atm}(\nu)$ is the atmospheric transmission, $L_{path}(\nu)$ is the path radiance, and $R(\nu)$ is the instruments spectral response curve.

Graphically, the components of this integral are shown in Figure 18 where the Planckian is propagated through a short atmospheric path, the path radiance of air at 300K is added (in this case minimal impact) and then integrated under the instrument's band pass filter. This integral provides a singular radiance value ($L(T)$) that the imager should see.

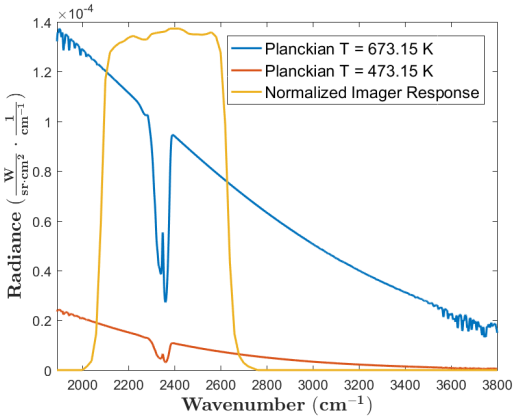

Figure 18: Planckian curves with atmospheric influence used for calibration and the normalized SBFP imager spectral response, $R(\nu)$

The integrated value computed is then compared to digital data collected by

www.manaraa.com

the imager. With a uniform source flooding the field of view of the imager, one would expect a uniform output. This is not the case due to electronic noise, read-out influences, detector non-uniformity, and optical distortion and aberrations. As a result of these non-uniformities, calibration must also include a mitigation for these errors where possible. Ultimately, the noise of the detector electronics will be a limiting factor and its impact will be addressed at a later point. Assuming the noise is random, a temporal average over a number of frames will be used for the calibration and is a statistical mean. Within the noise threshold, this is the pixel value that can be expected in an independent measurement.

A calibration attempts to map digital count values to a radiometric quantity, namely radiance. In order to do this, a minimum of two radiance sources are needed to do this correlation. This assumes a linear response of the detector which in this case, Indium Antimonide (InSb), is a satisfactory assumption. The two calibration sources would ideally span the entire dynamic range of the instrument so that any measurement made using the calibration would be an interpolation of the calibration sources.

With measurements of two sources and utilizing the simplifying assumption of linearity, radiance is related to the detector digital count value with the linear relationship

$$N_{i,j}(T) = G_{i,j} \times L_{i,j} + O_{i,j} \ , \tag{6}$$

for each pixel at row i and column j. The offset term ($O_{i,j}$), contains a radiance offset due to dark current as well as the other contributions from the optic elements that do not affect the gain of the imager. In the infrared portion of the spectrum (particularly the longer wavelengths), changes in optics temperature can affect the measured count value and if not compensated for, will lead to an error in the measurement. This change over time of the instrument offset is described as instrument drift. The gain

www.manaraa.com

term ($G_{i,j}$) contains the gain due to the detector, readout electronics, and A to D converters. While equation 6 is the correct form of the equation for physical understanding, a more useful relationship uses $N_{i,j}$ as the independent variable. In this setup, the gain and offset terms are redefined for simplicity but linear relationship still holds.

$$L_{i,j}(T) = G_{i,j} \times N_{i,j} + O_{i,j} \tag{7}$$

This relationship can then be applied on a pixel by pixel basis over the entire 2D image. As a result of this calibration, the two images are correlated to a uniform value and thus a 2-point non-uniformity correction has been performed as well. This process can be done in two individual steps which provides simpler calculations of statistical quantities. Again assuming linearity, the normalized count value can be related to the unnormalized image through a pixel gain and an pixel offset term as seen in the relationship,

$$N_{N\ i,j}(T) = Gp_{i,j} \times N_{Ii,j} + Op_{i,j}\ , \tag{8}$$

where the pixel gain $Gp_{i,j}$ and pixel offset $Op_{i,j}$ are calculated to correct each individual pixel to some representative mean count value. For this calibration, the mean of the entire image was used. Two images were normalized for use in the calibration and are shown in Figure 19. The normalization procedure gives uniform images as expected with count values of 12543.2 and 2106.7 for the blackbody references at 673.15 K and 473.15 K respectively.

Using these two normalized images, one can linearly fit these to an apparent effective radiance value which results in the same value for the gain ($G_{i,j}$) and offset term ($O_{i,j}$) in Equation 7 for every pixel. For this gain (as defined from Eqn 7) is calculated to be $4.249 \times 10^{-6}\ \frac{Radiance}{Counts}$ which represents the minimum radiance

www.manaraa.com

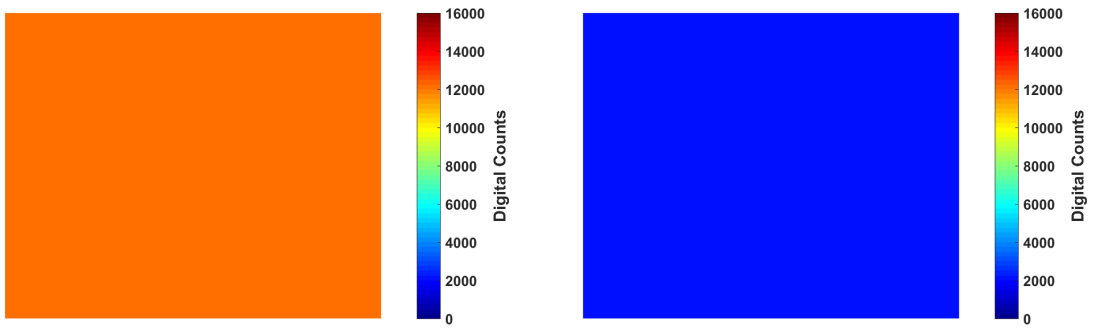

(a) **(b)**

Figure 19: Non-Uniformity corrected calibration images for (a) a 673.15 K blackbody with a mean count value of 12543.2 and (b) a 473.15 K blackbody with a mean count value of 2106.7

value that could be measured, i.e. the precision of the instrument. Using this same equation, the offset term (-2.578×10^{-3} $\frac{W}{sr \cdot cm^2}$) is always a negative number. This means that there are other contributions on the detector so that even with a zero radiance source, a count value is reported. This is not to imply that a negative radiance can be measured. The detector will not report counts below this threshold value as long as the imager is properly calibrated.

5.4 SBFP Imager Noise

To asses the noise influence, we look at the temporal variation of a given pixel while viewing a uniform source. Because the standard deviation of the count value is a function of the source radiance, both calibration source images were used. The standard deviation for each pixel was calculated over the 100 individual frames. The average of these values was taken for an overall assessment of the noise of the detector. Because the calibration was performed on a pixel by pixel basis, the individual pixel standard deviations were calibrated using the individual gains and offsets and then averaged to arrive a noise equivalent radiance. This radiance was used to calculate a change in temperature necessary from each source that would produce this radiance,

www.manaraa.com

i.e. the noise equivalent delta temperature ($NE\Delta T$). For the 673.15 K and 473.15 K sources the noise in terms of counts was 3.2 and 1.3. In terms of radiance, the noise is 1.37×10^{-5} and 5.62×10^{-6} $\frac{W}{sr \cdot cm^2}$ and the $NE\Delta T$ is calculated to be 0.04 and .02 K respectively. Below in Figure 20, the noise for each pixel can be seen. The average over this entire image was used for the previous calculations.

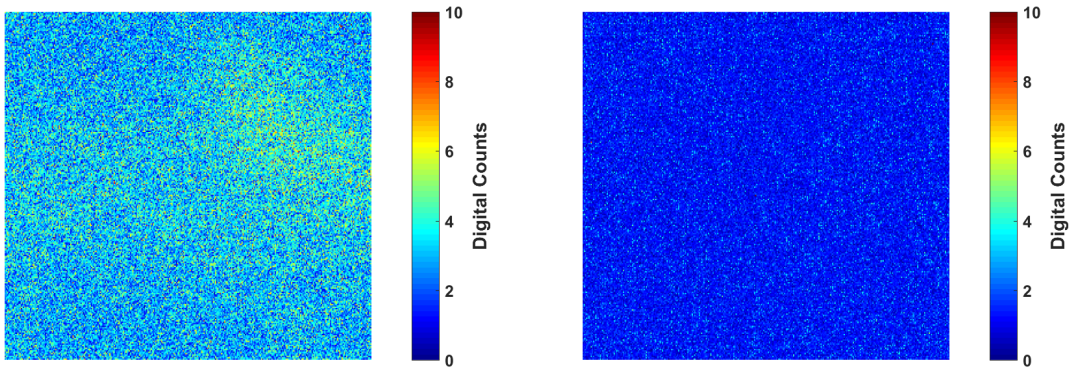

(a) **(b)**

Figure 20: Standard deviation in counts for 100 non-uniformity corrected images for (a) a 673.15 K blackbody and (b) a 473.15 K blackbody.

5.5 SBFP Imager Uncertainty

Applying the non-uniformity correction to another calibration image at 673.15 K image, the correction is not perfect. If the correction were perfect we would expect another uniform image. However, Figure 21 shows the normalized image which has a standard deviation of 4.1 counts which correlates to a radiance difference of 1.707×10^{-5} $\frac{W}{sr \cdot cm^2}$.

To get idea of this uncertainty, we compare the difference in radiance to an in-band apparent effective radiance value of 4.89×10^{-2} $\frac{W}{sr \cdot cm^2}$ for a 673.15 K source. This comes to less than a 0.1% error due to scene variation on a normalized uniform image.

www.manaraa.com

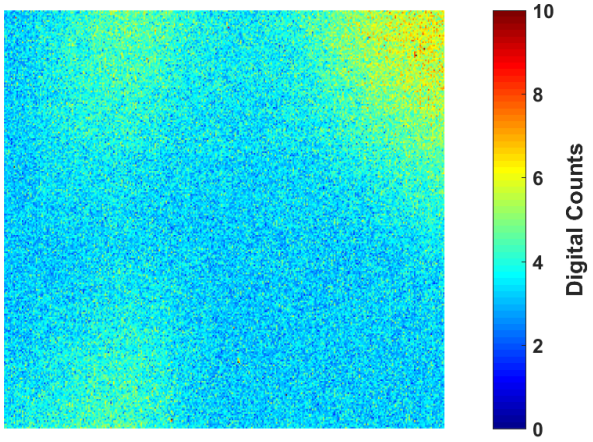

Figure 21: Uniform Calibration Images

Additionally, there is error due to changes in gain of the instrument. This error can be caused by many different sources; the detector may not behave linearly, the electronics temperature can change the gain of the imager, or a temperature change in optical elements during may manifest itself like a gain change. The mechanism of the instruments nonlinearity is unable to be determined from these data alone, however, by examining repeated calibrations, the magnitude of the change possible can be quantified. For two calibration sets performed on different days, the gain terms where 4.249×10^{-6} and 4.118×10^{-6} $\frac{Radiance}{Counts}$, approximately 3% different. While this does not directly relate to the uncertainty, this can be used to give an upper bound of potential errors associated with the gain. With the linear calibration, this error is directly proportional to uncertainty in radiance.

A first order approximation due to the maximum offset error is determined by comparing the drift between different calibrations. The values -2.578×10^{-3} and -2.929×10^{-3} $\frac{W}{sr \cdot cm^2}$ were used from the different day calibrations giving a difference of 3.5×10^{-4}. This error does not scale with the source being measured, so as a percentage, the lower the radiance measured, the higher percent uncertainty. For the

www.manaraa.com

two calibration sources which span the range of measurements, the errors are 5.9% and 0.7% for the 473.15 K and 673.15 K source respectively.

These calculations are for an upper bound based on the measurements available, however, many of the errors are mitigated by the measurement procedure. The calibrations were performed immediately after the measurements, before and after the measurements and only after the imager was adequately cooled and stable. This uncertainty does not account for any systematic errors that are present in the calibration setup, errors in spectral emittance and temperature of the blackbody, and uncertainty in path transmission. For these reasons, multiple measurement devices are often useful for identifying suspect data.

5.6 IFTS HSI Calibration

For a non-imaging spectrometer, everything within the field of view of the instrument is spatially integrated into the signal reported. The IFTS HSI gathers its spectral information by way of a Michelson interferometer. This splits the incoming radiation into two optical paths, one fixed and one changing, and recombines the signal to form constructive and destructive interference patterns temporally varying on the detector. These interferograms, shown in Figure 22 (a) are then Fourier transformed into the spectral domain to analyze the frequencies associated with the incoming radiation in (b). By knowing the spectral distribution of the incoming radiation, a calibration can be performed wavelength by wavelength (or in frequency). For the IFTS, all the spectral quantities must be preserved and the radiance is expressed similarly to Equation 5 but without the integral as

$$L_{\nu,T} = [\varepsilon(\nu) \cdot B_\nu(\nu, T) \cdot \tau_{atm}(\nu) + L_{path}(\nu)] \cdot R(\nu) \ . \tag{9}$$

www.manaraa.com

Any spectral weighting present will be calibrated out as the calibration is being performed at each wavelength. The effect of this response is to limit the wavelength range over which the IFTS responds. As will be shown, this is not a distinct cutoff, and noise will increase as the detector becomes less and less sensitive.

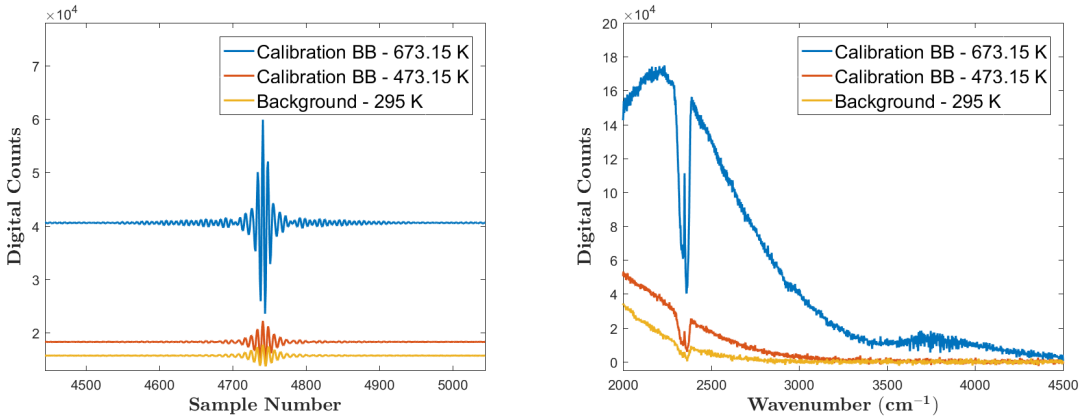

Figure 22: (a) Interferograms and (b) raw spectra for blackbody calibration sources at 673.15 K and 473.15 K.

Equation 9 is used to calculate the apparent effective spectral radiance values to correlate to a count values for each wavelength. This was done precisely in the same way as the imager using Equation 7. Instead of iterating over each pixel of an image, which was a spectrally integrated quantity, a gain and offset for each wavelength is calculated. For the IFTS, the non-uniformity and calibration were done together.

As can be seen in the raw spectra, the radiation from the calibration sources is being absorbed by the CO_2, centered at 2349 cm^{-1}. As the blackbody is emitting according to Equation 5, it should be a continuum through this portion of the spectrum if not for the atmospheric path (this assumes the detector and optical element transmissions are smooth through this portion as well). This degree to which the continuum is attenuated defines $\tau_{atm}(\nu)$. As long as the signal is not completely attenuated, the calibration can still be performed at these wavelengths. For these measurements the integration time for the detector is set to be fast enough so as not

www.manaraa.com

to saturate when measuring hot exhaust gases and as a result the background of the measurements is within the noise of the instrument. Therefore, the path radiance term is neglected and the radiance is calculated using Equation 9.

With a spectral radiance, the gain and offset of the instrument are computed spectrally with the gain assumed to be smooth throughout the CO_2 absorption region as shown in Figure 23 (a). When this calibration is applied to the raw spectra the calibrated spectra are generated in Figure 23 (b). The background, which appears at the noise threshold of the instrument, produces negative radiance at the CO_2 absorption region. Knowing this is an error in the calibration and that the background should be at the noise floor, the offset term can be adjusted for each wavenumber where this occurs. With this correction in place the corrected calibrated spectra are shown in Figure 24.

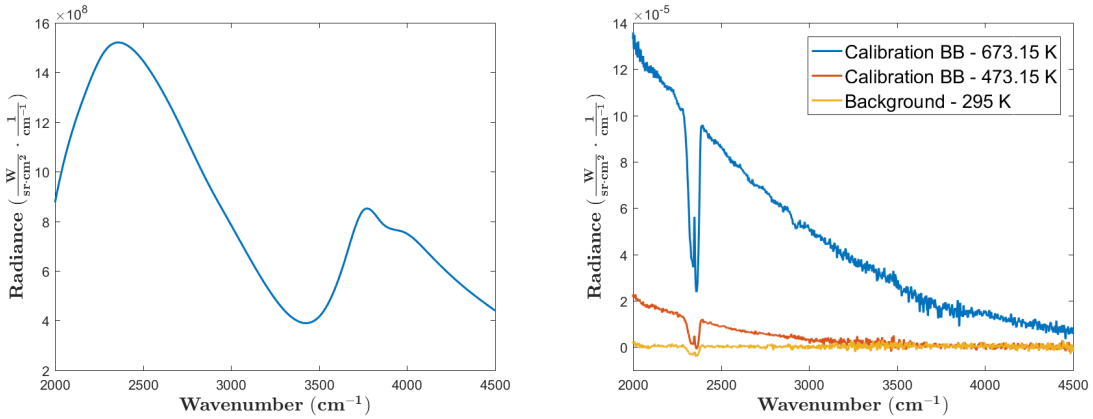

Figure 23: (a) Single pixel gain curve and (b) gain and offset applied to the raw spectra of calibration sources.

For the IFTS HSI, this process is repeated for each pixel of the imager. Similar results were produced throughout the array and result in a calibrated hyperspectral data cube.

www.manaraa.com

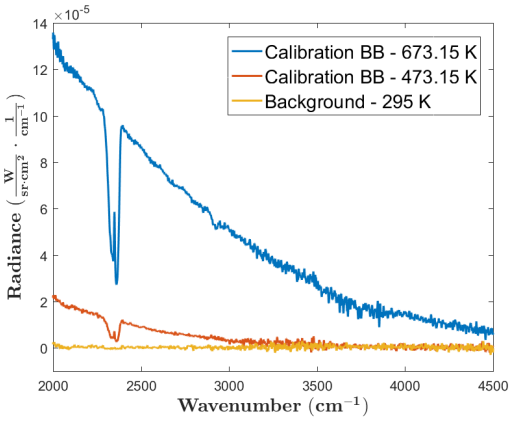

Figure 24: Gain and offset applied to the raw spectra of calibration sources with noise floor correction.

5.7 IFTS HSI Noise and Uncertainty

For the IFTS, which has a different gain and error at each wavenumber, noise must be considered spectrally as well. The standard deviation was performed for 10 scans of the high temperature calibration source and the noise equivalent counts is plotted in 25. Using the calibration gain and offset, the noise equivalent counts (NEC) curve in Figure 25 is converted to radiometric units and the noise equivalent radiance (NER) is plotted in Figure 26 (a) and the percent error plotted in (b). The noise is significantly lower at the lower wavenumbers, as the signal is much higher in this portion of the spectra and the detector is more responsive as well (a higher gain). Where the signal is much lower (at the higher wavenumbers), the percent error rapidly increases.

As a linear assumption has been used for the IFTS HSI calibration, the uncertainty due to noise is directly proportional to the radiance measure. Here at the longer wavelengths (smaller wavenumbers), where the CO_2 measurements are being made, the uncertainty associated with the noise is less than 5%. Where the H_2O is measured in larger wavenumbers, the error is approximately 20%. This should be considered in the analysis and any use of the data.

www.manaraa.com

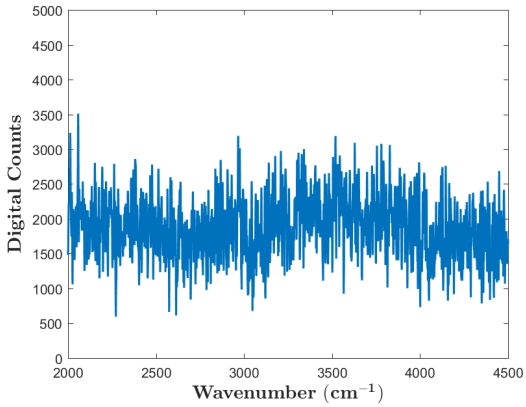

Figure 25: Single pixel noise equivalent counts for 10 scans.

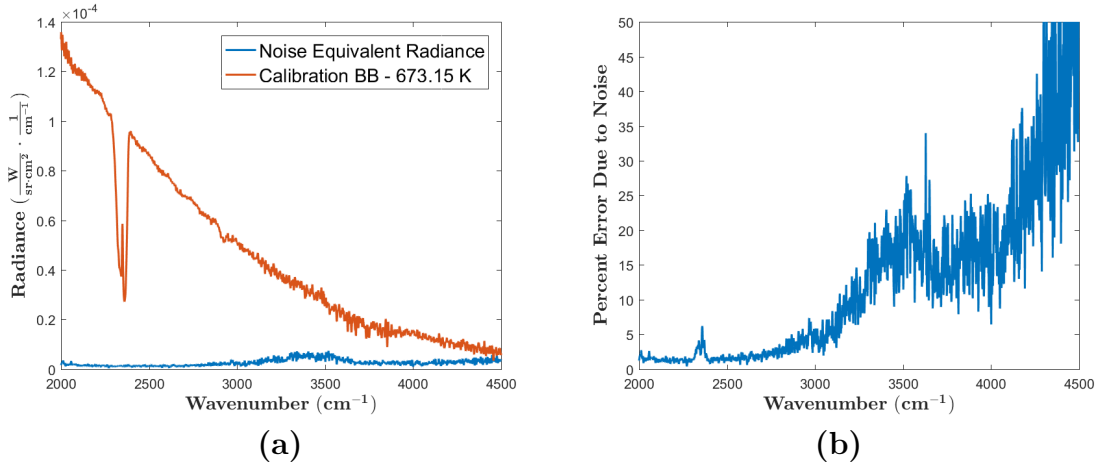

(a) (b)

Figure 26: (a) Single pixel noise equivalent radiance for 10 scans and (b) its associated percent error compared with the calibration source.

5.8 Calibration Summary

These calibration techniques and implementation have shown to be very effective for both the $3.8 - 4.8\mu m$ SBFP imager and the IFTS HSI. The error associated with both of these instruments are on the order of 5% percent while operating within the range of the calibration sources. Some limitations exist in the calibration of the HSI as the calibration sources provided limited signal at high wavenumber. With such a broad spectral range, it is a challenge to get a high signal at high wavenumbers without saturating the interferogram. This results in higher errors in these ranges

www.manaraa.com

which encompass an H_2O emission band. This could be mitigated by using band-limiting filters to focus on specific portions of the spectrum. Additionally, the spectral resolution could be lowered to increase signal to noise. By trading resolution, high frequency noise is reduced due to a decreased OPD from shorter mirror translation. As a result, the the number of scans that could be collected over the same time would increase. This would additionally increase the signal-to-noise ratio (SNR) in the time-averaged measurement.

As shown in Chapter IV, the agreement between these two instruments when compared to one another is on the order of the uncertainty associated with each. This allows for confidence in the use of this data for the tomography algorithms to follow.

www.manaraa.com

VI. Spectroscopic Databases and Spectrum Generation

6.1 Introduction

Using calibrated hyperspectral measurements, the concentration of a species and its temperature can be determined by comparing the measured spectrum to theoretical and empirically derived values in the literature. Using available spectroscopic databases, like HITRAN [26], a given temperature, pressure, concentration of species, and path length will dictate a transmission and emission spectrum associated with a gas. The spectra generated from these databases are then compared with the measured values and then adjusted until agreement is reached. Interestingly, these parameters affect the spectrum produced by the gas in different ways such that a unique solution exists for each measurement within instrument and measurement uncertainty.

6.2 Spectroscopic Databases

The spectroscopic databases used for comparison are readily available in the literature. The most complete database of atoms and molecules is the HITRAN database [25]. This database of line positions and associated parameters is used as the starting set by many other databases. However, further research is often used to augment or add to this database. For example, the carbon dioxide spectroscopic database (CDSD) [31] has shown to be more accurate for high temperature carbon dioxide spectra and is often employed for research where this may be of importance. The Atmospheric and Environmental Research (AER) spectroscopic database uses these two databases as well as further published research to obtain an even more accurate database. In addition, they develop and maintain code like the line-by-line radiative transfer model (LBLRTM) to generate needed spectra from the databases [7]. The

www.manaraa.com

line positions and parameters reported in these databases are analytic in nature but are adjusted or augmented to fit empirical data. Where possible, the parameters associated with a specific line of a species are used. When this approach is too inaccurate, the databases use measured cross-section data of a molecule for the computations.

Line Position.

For a given atom or molecule, the transition of an electron from one energy state to another will result in an absorption or emission of radiant energy at a wavelength corresponding to the energy associated with this change. The relationship between this change in energy and the wavelength of the radiation absorbed or emitted is described by the Planck relation

$$\Delta E = \frac{hc}{\lambda} \ , \tag{10}$$

where ΔE is the change in energy, h is Planck's constant, c is the speed of light, and λ is the wavelength of the energy absorbed or emitted. This relationship is key in understanding the spectrum produced by the atoms and molecules in a measured gas.

This change in energy can be a result of an electronic transition whereby an electron goes from one energy state to another (which is seen as a change in quantum number). An electron in an atom in a ground state can be elevated to a higher energy state by the absorption of a photon. This transition is seen in a measurement when a radiation source is absorbed by a gas at a wavelength that corresponds to this energy difference. Laser absorption measurements take advantage of this and are a common method of absorption spectroscopy. In addition, an electron can relax from a higher energy state to a lower state and a photon will be emitted at a corresponding wavelength in a process of spontaneous emission. Specific selection rules govern whether electronic transitions are allowed or forbidden [2]. For an atom, a reasonable list (on

www.manaraa.com

the order of tens to hundreds) can be made of the allowable transitions that would be observable. At too high of an energy, the electron will dissociate from the atom and the absorption spectra will not be seen. The energy associated with electronic transitions corresponds to wavelengths that are in the visible wavelength range. For atoms, these are the only transitions observable.

For molecules, the change in energy can also be a result of a difference in vibrational and rotational energy states. These states are a result of atomic motion within a molecule. According to the Born-Oppenheimer approximation, compared with the movement of massive particles (like the nucleus of an atom), the small-mass electrons will effectively respond instantaneously. This approximation shows itself when the energy differences due to changes in the vibrational and rotational states can be observed in the absorption and emission spectra of the molecules. The energy difference associated with these transitions are seen in the infrared portion of the spectrum.

In Figure 27, the Carbon Monoxide Molecule absorption lines are given for this wavelength range as obtained from the HITRAN database [25]. For clarity, some of the lower intensity lines were removed from the plot. The vibrational transition of the CO molecule determines the center of this spectrum located at a wavelength of 4.66 μm. The transitions between rotational energy levels govern the positions of all of the lines relative to this line-center. These line positions and intensities are valid only for this pressure (1 atm) and temperature (296 K).

Line Strength.

The intensity distribution for the different rotational transitions are dictated by the Boltzmann distribution. The probability of an energy state, p_i, is defined as

$$p_i = \frac{1}{Q} e^{-E_i/kT} \ , \tag{11}$$

www.manaraa.com

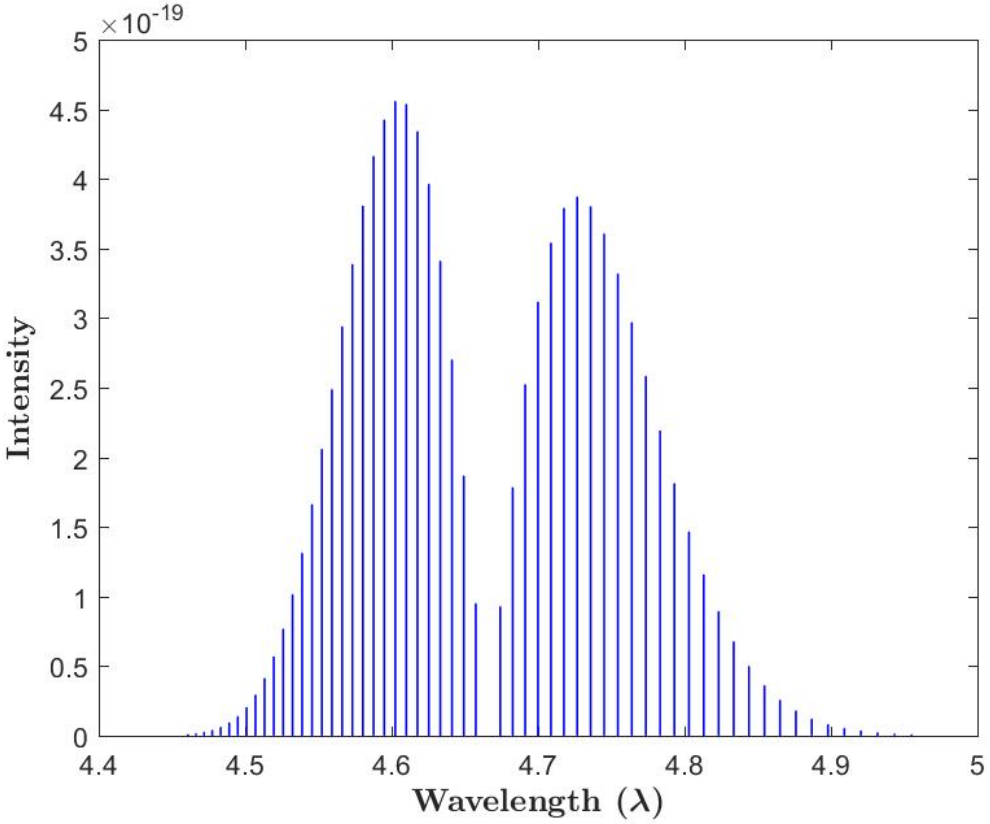

Figure 27: CO line positions and intensities from HITRAN database.[25]

in terms of the energy of that state (E_i), the temperature (T), the Boltzmann constant (k), and the partition function (Q).[2] The partition function can be thought of as a normalizing factor in that it is the sum of the exponential term for all states (i). This gives a sum of the probabilities for all states equal to 1.

This distribution function describes the relative strength of each of the rotational energy levels. As the gas is heated, higher energy levels become more accessible and the distribution spreads. This relationship of temperature to the intensities of the lines manifests itself in measurements when hot gases propagate through a cooler atmosphere. The hotter gases emit a broader spectrum of radiation that will be less affected by the propagation through cooler gas. This is particularly relevant when considering an abundant atmospheric gas like CO_2.

www.manaraa.com

Line Shape.

With the line position and prescribed intensity, the spectral distribution, or line-shape, describes the actual absorption spectrum. While many factors contribute to the line shape, the two main contributors are temperature and pressure. Where one of these effects dominate, the line shape conforms to one of two equations. For the high pressure cases, collisions between the molecules occur at a faster rate than the spontaneous emission, which forces some photons to be released shorter times, broadening the absorption line. This collision broadening is the driving mechanism and the line shape conforms to a Lorentz profile as specified as

$$\kappa_\eta = \frac{S}{\pi} \frac{\gamma_L}{(\eta - \eta_0)^2 + {\gamma_L}^2} \tag{12}$$

where S is the integrated line intensity, η is the wavenumber of interest, η_0 is the line position (or line center) in wavenumber, and γ_L is the half width half maximum (HWHM) of the absorption line.[20]

When pressures are low, collisions occur less often and the broadening of the absorption line is a result of the Doppler effect due to the moving molecules in all directions. This Doppler broadening is a Gaussian curve described by

$$\kappa_\eta = S \frac{\sqrt{ln2}}{\gamma_D \sqrt{\pi}} \; exp\Big[- (ln2) \Big(\frac{\eta - \eta_0}{\gamma_D} \Big)^2 \Big] \; . \tag{13}$$

These two equations are normalized so that the integral of them over all wavenumbers is equal to S, the line intensity.

In reality, the effect of temperature and pressure are not separable as these equations have implied. The convolution of the Lorentz and Doppler profiles construct the Voigt profile. Because there is no closed form solution to the equation describing the Voigt profile, look up tables or approximate equations are often employed to

www.manaraa.com

describe the profile. In Equation 14, the full width half maximum (FWHM) of the Voigt profile, α_V, is defined as

$$\alpha_{_V} \;=\; 2\cdot\gamma_{_V} \;=\; .5346\cdot(2\cdot\gamma_{_L}) + \sqrt{.2166\cdot(2\cdot\gamma_{_L})^2 + (2\cdot\gamma_{_D})^2}\;, \qquad (14)$$

a function of the Doppler and Lorentz HWHM. Although an approximation of their relationship, Eq. 14 is accurate over the entire range to within 0.02%. [22]

In Figure 28, these three types of profiles are plotted around a line center of zero. For each curve, the HWHM is equal to 1 and the line intensity S are all the same. This is to say, that the integrals of each curve over all wavenumbers are equal so as to conserve energy. For the Voigt profiles (dashed lines), the ratio of $\gamma_{_L}/\gamma_{_D}$ is useful in relating how influenced the profile is by the Doppler or Lorentz broadening. This ratio is noted on the graph for each Voigt curve.

By defining the HWHM and the line shape type, the absorption spectrum for a given line can be spectrally defined. This broadened line is extended over a finite wavenumber range. Beyond this range, the contributions from the particular line are assumed negligible. Because it is difficult to define where the contributions are no longer significant, codes often leave this range as an input in terms of the HWHM. The choice in this parameter can significantly affect the time associated with computation, thus trading time for accuracy. The process of generating the absorption spectrum is repeated for every line provided in a spectroscopic line-by-line database. These spectra are then summed over a defined spectral range to give a total absorption spectrum for a single homogeneous atmospheric layer.

Spectroscopic Database Parameters.

The spectroscopic databases are reported in terms of parameters that define the position (in wavelength), strength (or intensity), and line-shape (distribution) for a

www.manaraa.com

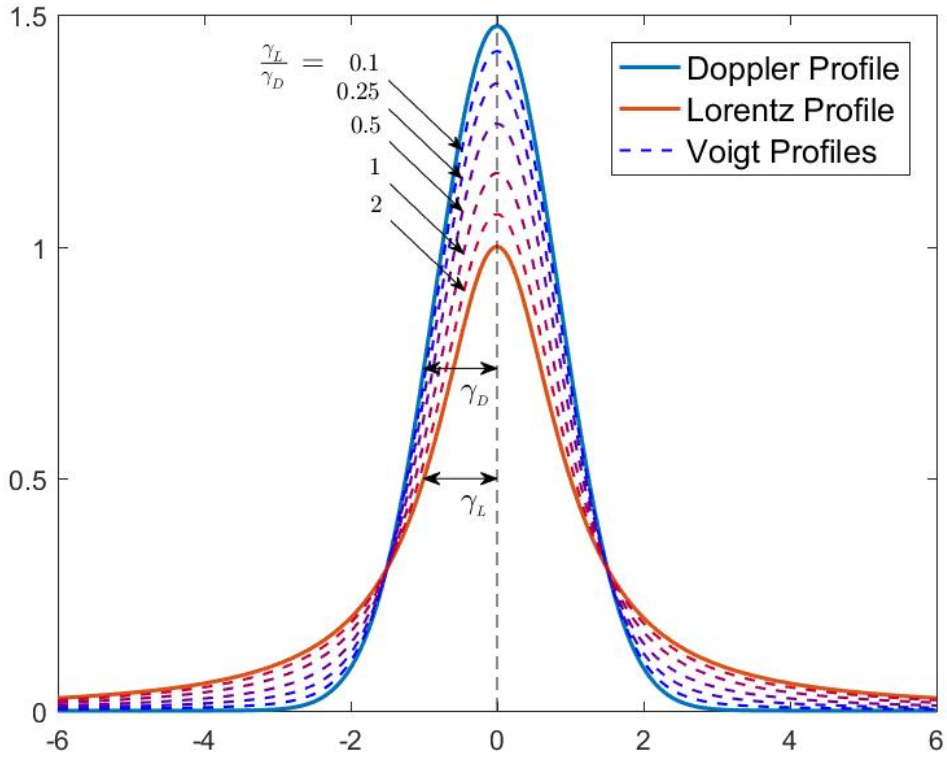

Figure 28: Line Shape profiles.[20]

given gas absorption line as a function of its temperature, pressure, concentration, and path length. The parameters listed in Table 1 are those provided by the HITRAN line-by-line database.

These parameters in Table 1 are given relative to a reference temperature (296 K). This approach allows for a simplified calculation for the intensity of a line at a new temperature. Using Equation 11, the new intensity can be simplified to

$$S_{ij}(T) = S_{ij}(T_{ref})\frac{Q(T_{ref})}{Q(T)}\frac{e^{-E_{ij}/kT}}{e^{-E_{ij}/kT_{ref}}}\frac{1-e^{-\nu_{ij}/kT}}{1-e^{-\nu_{ij}/kT_{ref}}} \ . \tag{15}$$

This requires only referencing the total sum partition function of the new temperature,

www.manaraa.com

Parameter	Description
Mol	Molecular Species identification (ID) Number.
Iso	The isotopologue ID number.
ν_{ij}	The wavenumber of the spectral line transition (cm^{-1}) in vacuum.
S_{ij}	The spectral line intensity (cm^{-1}/(molecule·cm^{-2})) at T_{ref}=296K.
A_{ij}	The Einstein-A coefficient (s^{-1}) of a transition.
γ_{air}	The air-broadened half width at half maximum (HWHM) (cm^{-1}/atm) at T_{ref}=296K and reference pressure p_{ref} = 1 atm.
γ_{self}	The self-broadened half width at half maximum (HWHM) (cm^{-1}/atm) at T_{ref}=296K and reference pressure p_{ref} = 1 atm.
E''	The lower-state energy of the transition (cm^{-1}).
n_{air}	The coefficient of the temperature dependence of the air-broadened half width.
δ_{air}	The pressure shift (cm^{-1}/atm) at T_{ref}=296K and p_{ref} = 1 atm of the line position with respect to the vacuum transition wavenumber ν_{ij}.
g'', g'	The lower and upper state statistical weights.

Table 1: HITRAN line-by-line parameters and descriptions.[24]

and the reference temperatures and the parameters provided. HITRAN provides a Fortran code called total internal partition sum (TIPS) which uses tabulated values to give the $Q(T)$ for the current temperature [24].

The Doppler broadening HWHM for a temperature T is given as

$$\gamma_D(T) = \frac{\nu_{ij}}{c}\sqrt{\frac{2N_A kT \cdot ln2}{M}} \ , \tag{16}$$

where M is the molar mass of the isotopologue in grams and N_A is Avogadro's constant .

The Lorentzian HWHM for a pressure p and temperature T is specified as

$$\gamma_L(p,T) = \left(\frac{T_{\text{ref}}}{T}\right)^{n_{\text{air}}} (\gamma_{\text{air}}(p_{\text{ref}},T_{\text{ref}})(p-p_{\text{self}}) + \gamma_{\text{self}}(p_{\text{ref}},T_{\text{ref}})p_{\text{self}}) \ , \tag{17}$$

where p_{self} is the partial pressure of the isotopologue.

The line position for each can be affected by the pressure of the isotopologue.

www.manaraa.com

This shifted position, ν_{ij}^*, is

$$\nu_{ij}^* = \nu_{ij} + \delta_{air}(p_{\text{ref}})p \ . \tag{18}$$

Using these equations and the HITRAN parameters, an absorption spectrum can now be generated for a homogeneous atmospheric layer in a software implementation like line-by-line radiative transfer model (LBLRTM).

6.3 Line-By-Line Radiative Transfer Model (LBLRTM)

As discussed LBLRTM uses the HITRAN database parameters among others to perform the radiative transfer through not only a single homogeneous layer, but then multiple homogeneous layers as well. LBLRTM is a Fortran written code maintained by AER. In order to use the HITRAN parameters, another code called LNFL (line file) creates an input file from the database file for LBLRTM in a format that it requires. Because the parameters can sometimes change or are augmented with others, the version of the atmospheric database, LNFL, and LBLRTM must all be compatible. For both of these programs, a TAPE5 file is created. For LNFL, this ascii file describes the wavenumber range of interest and the species within the database to maintain. The output of this program is a TAPE3 file which serves as the binary input database correctly formatted for LBLRTM. The TAPE5 file for LBLRTM specifies (among many other options) the wavenumber range, spectral resolution, type of computation, and different layers. Further uses and capabilities are listed in the AER documentation [7]. When the LBLRTM program is run, a TAPE12 binary output file is created. In one mode of operation, specified in the TAPE5 file, the TAPE12 file contains a wavenumber and associated optical depth. In another mode, it contains a wavenumber and associated radiance and transmission value.

www.manaraa.com

Optical Depth.

Running LBLRTM for a concentration, N_1, of a single isotopologue at a specified temperature and pressure, an optical depth is obtained. In Figure 29, the optical depth of CO_2 can be seen whereby LBLRTM applied a line shape and intensity to the line positions from before. This spectrum was generated for a temperature of $300K$ and pressure of 1 atm.

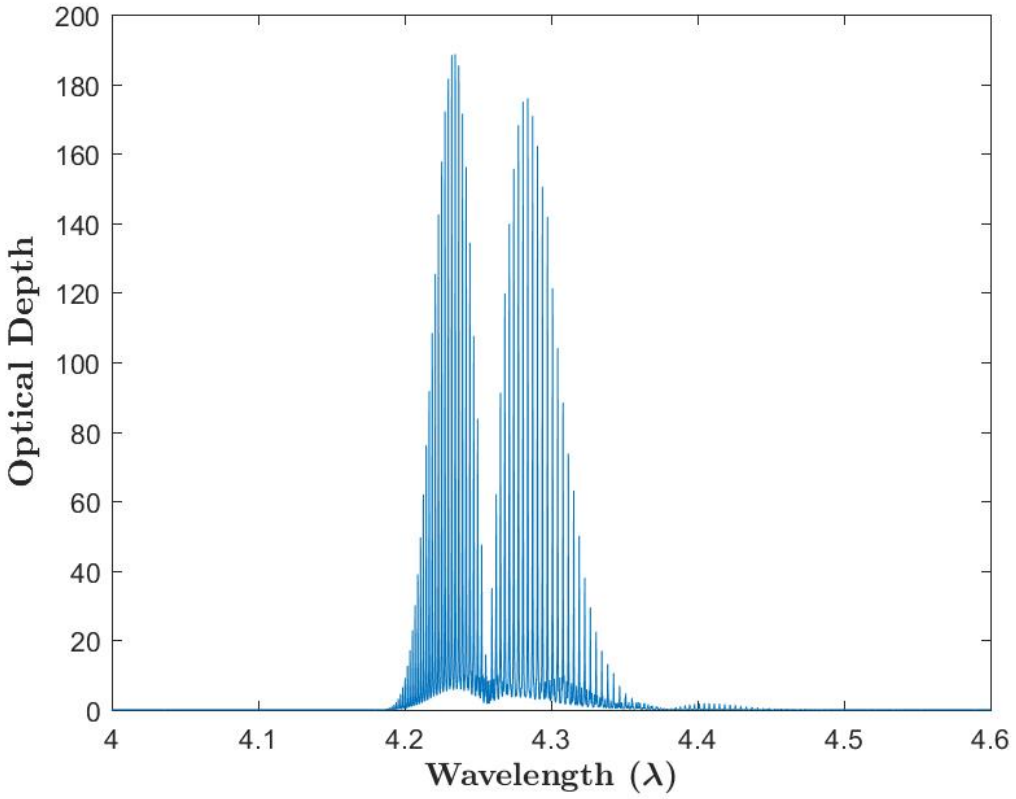

Figure 29: CO_2 Optical Depth.

Transmission Spectrum.

Using Beer's law, seen in Equation 19, the spectral transmission, τ_λ, of the CO_2 can be calculated as

$$\tau_\lambda = e^{-OD} \tag{19}$$

www.manaraa.com

from the optical depth (OD) obtained from LBLRTM. The calculated transmission of the CO_2 gas can be seen in Figure 30 for a path length of 10 m and concentration of 500 ppm. Over this path length and concentration, complete absorption occurs at wavelengths just over $4.2\mu m$ where the transmission curve goes to zero.

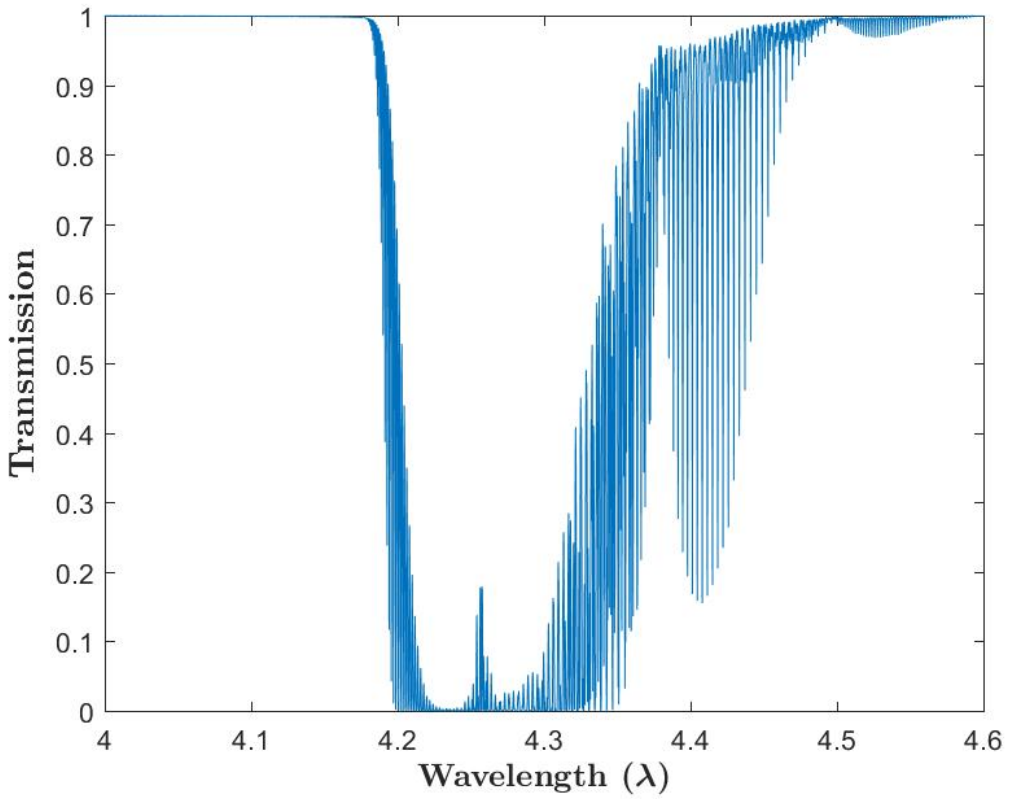

Figure 30: CO_2 Spectral Transmission.

Absorption Cross-Section.

Because the optical depth is associated with a specific concentration and path length of a gas, it is often convenient to calculate the cross-sectional area of a given gas. This absorption cross-sectional area, $\sigma_{12}(\lambda)$, is related to the optical depth by

$$OD \;=\; \sigma_{12}(\lambda) \cdot N_1 \cdot L \;, \tag{20}$$

www.manaraa.com

where N_1 is the population of the ground state for this transition and L is the path length through the gas. With the absorption cross-sectional, a transmission spectrum can be calculated for varying path lengths and concentrations of a single species at a single temperature.

Emission Spectrum.

In the case of local thermodynamic equilibrium (LTE), and a non-scattering medium, the gas will emit radiation to the same degree that it absorbs. While the gas absorbs the radiation from the source, it emits radiation in accordance with its local temperature as described by Planck's equation (Equation 2) for a blackbody $B_\lambda(\lambda, T)$. Thus the path radiance of the gas (L_{path}) is defined as

$$L_{path} = B_\lambda(\lambda, T) \cdot (1 - \tau_\lambda) \ , \tag{21}$$

for the local temperature and at a specific wavelength (calculated per unit wavelength).

Applying this Eq 21 to the transmission curve generated in Figure 30, the path radiance is presented in Figure 31. Where the CO_2 had complete absorption, the path radiance seen in Figure 31 matches a blackbody curve associated with the local gas temperature. The assumption of LTE can be invalid in the event of large fluctuations in temperature, or if the path length has large variations in temperature. The errors associated with this assumption can be quantified by reducing the path length to an adequate level to resolve the temperature gradients so as to achieve LTE.

Multiple Layers and Propagation.

The case has been so far limited to the spectrum of single homogeneous layer with a concentration of a single species over a specific path length. With the data

www.manaraa.com

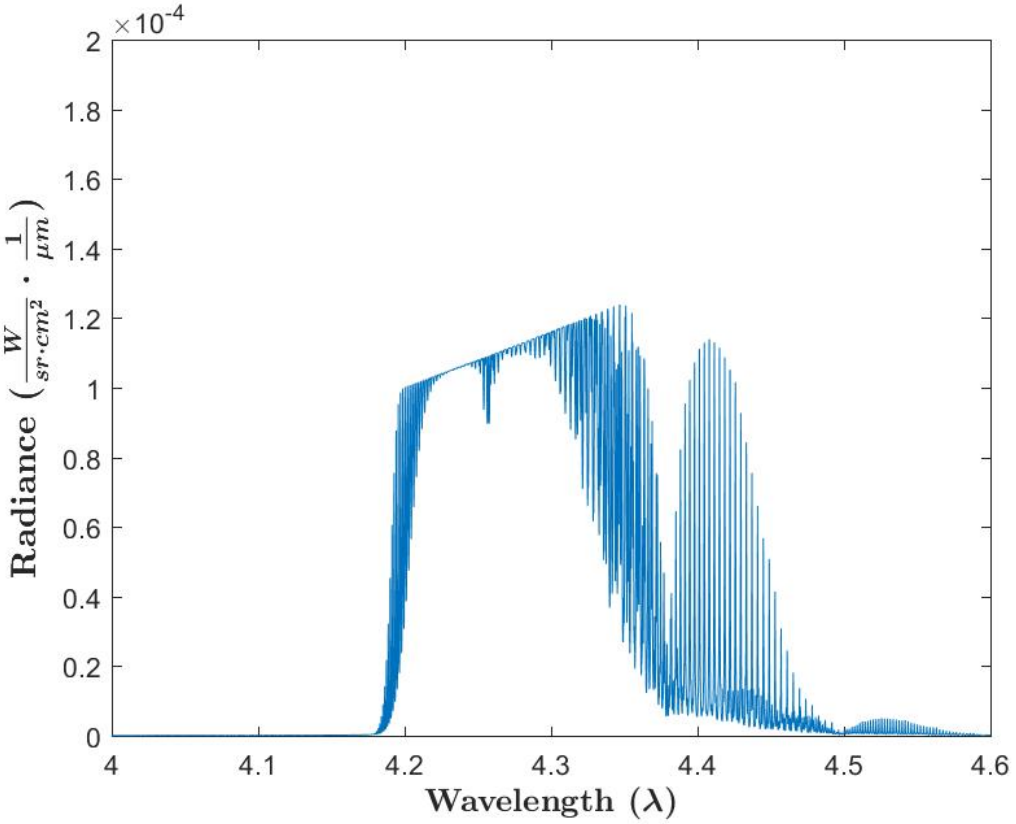

Figure 31: CO_2 Path Radiance.

generated or calculated using LBLRTM, multiple homogeneous layers may be combined to construct a single non-homogeneous path in a very straightforward way. The transmission of the entire path is simply the product of the individual transmissions for each layer. The path radiance is constructed from back to front with the first layer emitting radiation according to its local temperature (B_1). This radiation is attenuated by the second layer (τ_2) and the emission of the second layer ($(1-\tau_2)\cdot B_2$) is added to it. This total is now attenuated by the third (τ_3) which emits as well. This is continued through all the layers according to the local transmission and emission components as

$$L_{path} = \Big[\Big(\big((1-\tau_1)\cdot B_1\big)\cdot\tau_2 + (1-\tau_2)\cdot B_2\Big)\cdot\tau_3 + (1-\tau_3)\cdot B_3\Big]\cdot\tau_4 + \dots\,. \qquad (22)$$

www.manaraa.com

If a source exists behind the first layer (like earth) or any other spectral source, it can act as the starting point which will be attenuated by the first layer and added to its self emission. However, with the total path transmission and path radiance already calculated, any background can easily be inserted by attenuating the source radiance by the total (τ_{path}) and and adding back the total path radiance (L_{path}).

Fitting the Spectrum to Measurements.

Measured spectral data of a radiation source (like combustion exhaust) is usually performed through some atmospheric path and against some background. As such, even the simplest case of a single homogeneous exhaust layer is complicated by background contributions, and atmospheric propagation. When computing this spectra that would match the measured results, these factors cannot be neglected. In Figure 32, a single CO_2 layer at $400K$ is in front of a uniform blackbody at $325K$, and propagated through an atmosphere at $300K$. This figure shows how the original background is attenuated by both the exhaust and the atmosphere. At some wavelengths, the exhaust is completely attenuated by the atmosphere while at others, the elevated emission can still be seen. On the edges, where no CO_2 is present, the background black body continuum can be seen.

By running LBLRTM at many temperatures, pressures, and species, a database of cross-sections can be generated. With this multi-dimensional database, interpolation can be used to quickly converge on a solution to the measurements for simple cases. Difficulties in arriving at solutions can emerge when fundamental assumptions about LTE are invalid.

www.manaraa.com

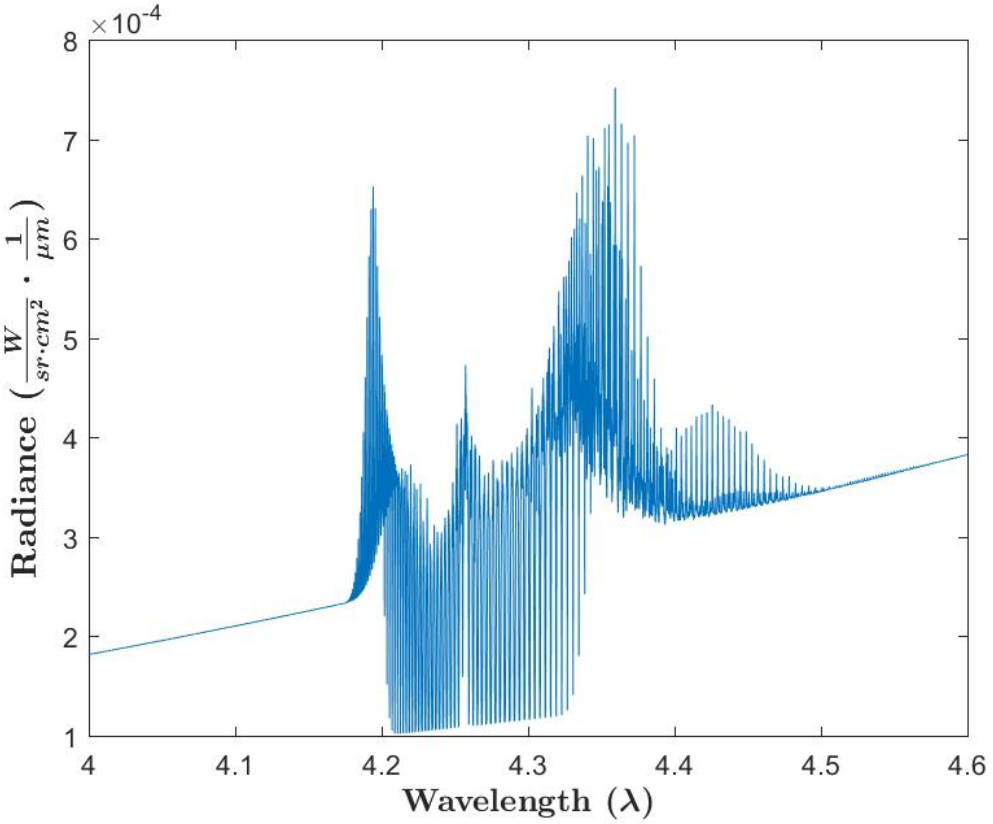

Figure 32: CO_2 propagated through an atmosphere.

6.4 Summary of Spectroscopic Database and Spectrum Generation

The spectroscopic databases described here are employed to generate an absorption spectrum for a given temperature and concentration over a homogeneous path. This spectrum is used to determine the spectral transmission as well as the emission spectra. By combining multiple homogeneous layers an emission spectrum produced along a non-homogeneous path is generated. With this spectrum generation process, this first-principle model can be fit to real measurement data. This process called hyperspectral tomography, is discussed next in Chapter VII.

www.manaraa.com

VII. Hyperspectral Tomography

7.1 Projections and Geometry

The methods discussed in Chapter VI show how a single line-of-sight measurement can be broken into multiple homogeneous layers and combined. Using the spectroscopic database, temperatures and concentrations of species are arrived at. As layers are added to better represent the measured path, the complexity aggregates. Because of the number of unknowns in a multi-layer solution, the answer for a single line-of-sight is no longer unique. This is then applied for multiple lines of sight from different viewing geometries through the same volume of gas. Hyperspectral tomography is the process by which these multiple measurement aspects of hyperspectral data are used to arrive at values of temperature and concentrations throughout the volume. The generated domain is a grid established from the measurement resolution or reduced to limit computations for a solution. For measurements made over a multi-layered path, the radiation that arrives at the detector of the instrument is a 2D projection of the scene. These measured projections made by the IFTS HSI act as the solution set to which calculated projections are compared. The computational domain is discretized into 3D points, or voxels, in which a single homogeneous temperature and concentration is assumed throughout. Similar to the work performed by Ma [19], the calculated values are compared back to measured ones while the temperature and concentration solutions are constrained to only realistic values. From this, a minimization function is generated whereby the best solution is converged upon.

Measured Projections.

Radiance images are shown in Fig. 33 for a measurement made from orthogonal directions of the rectangular high-aspect-ratio nozzle. The exit plane is selected from

www.manaraa.com

the flame to use as the measured projection set in the HT algorithm. Each pixel in these images represents a spectrum which is shown in Figure 34. Given the spatial resolution of the IFTS HSI, the data collected in a given pixel represents a spatially averaged spectrum. This is a result of gradients existing within the pixel that the instrument is incapable of resolving. As the data collected is temporally averaged as well, both these averages have a smoothing effect on the data and their impact will be discussed further in Chapter VIII. As a result of this smoothing, a subset of the collected measurement data can be used to represent the computational domain. This is helpful to significantly reduce the number of unknowns.

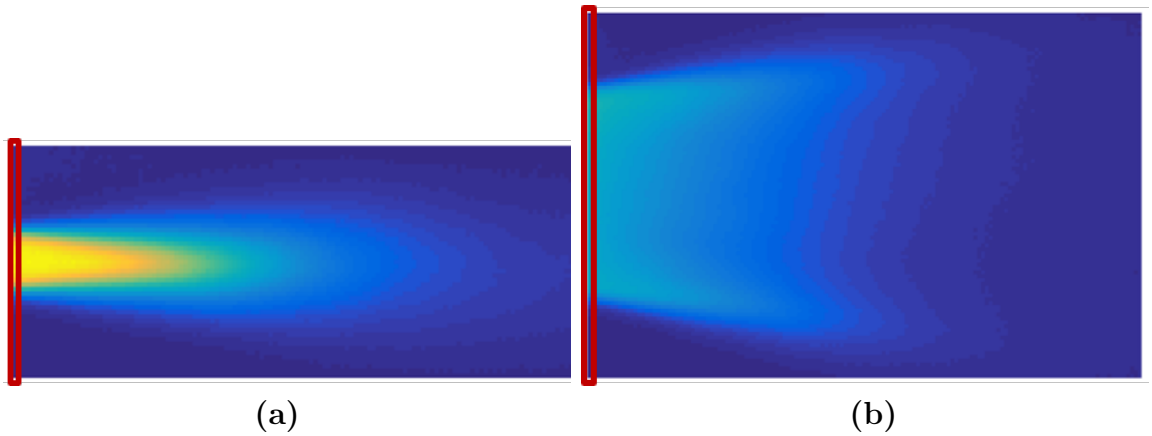

Figure 33: Selection of the solution plane for HT algorithm in the (a) horizontal and (b) vertical measurements. The red box indicates the selection of the exit plane.

Computation Geometry.

The computational domain for temperature T is shown in Figure 35 where a rectangular domain of $N \cdot M$ voxels is used to discretize the space. For each voxel, a temperature and concentration of both H_2O and CO_2 exist. The calculated and measured projections are labeled with the following convention. Projection 1 represents the projection of the first row viewed from the right, where projection 2 is the second row measured from the right. Projection $N + 1$ represents the projection

www.manaraa.com

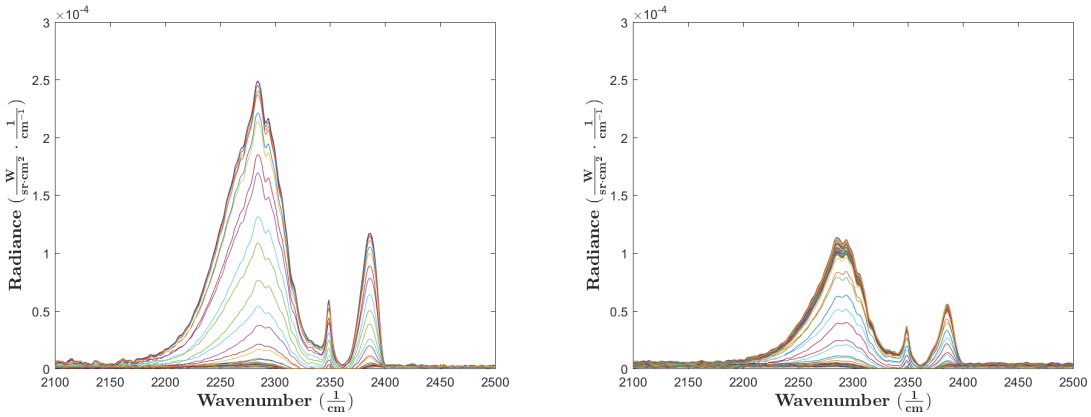

Figure 34: Exit plane spectra from the (a) horizontal and (b) vertical measurements.

of column 1 measured from the bottom, and projection $N + 2$ is the second column measured from the bottom and so forth. This defines $M + N$ projections to compare to the measured spectra. As the measurements were performed with a horizontal and vertical view only, no other projections were needed to be computed. However, this is not a limitation of the technique. An oblique path through the domain could similarly be calculated where the path length through a given homogeneous voxel is no longer simply the horizontal or vertical dimension.

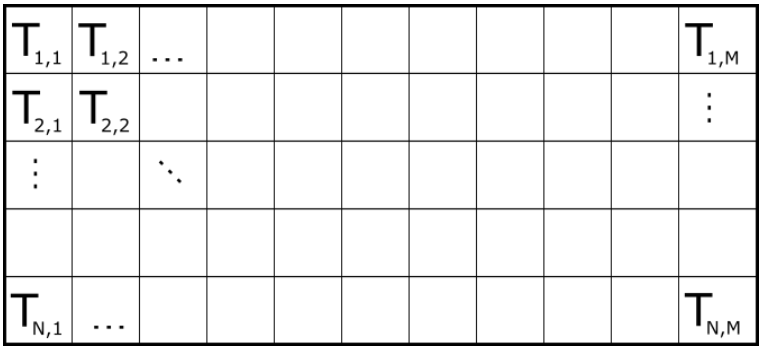

Figure 35: Computational domain for temperature T where a rectangular domain of $N \cdot M$ voxels is used to discretize the space.

www.manaraa.com

Atmospheric Influences.

The measurements analyzed here were made through an atmospheric path containing H_2O and CO_2. While the ambient air temperature and path length were measured, the concentrations of species were not. This complication must be considered when attempting to converge to the measured solution. In addition to measuring the exhaust gases, the exhaust nozzle itself was also present in the field-of-view of the HSI. Because the nozzle is not a selective emitter like the gases, it will emit broad-band radiation in accordance with Planck's law in Equation 5. As such, in the presence of no atmospheric influence, one would expect a continuum throughout the H_2O and CO_2 emission bands of interest. By observing the attenuation of the radiance measured in these bands, the concentrations can be determined. A gray-body curve was fit to approximate the emission spectrum of the nozzle, and with the spectroscopic databases, propagated through an atmospheric path. The concentration of this assumed homogeneous path of known length and temperature is iterated upon to determine the optimal concentration that aligns the calculations to the measured values. This is shown in Figure 36 where the source signature, computed apparent (as seen through an atmosphere), and measured values are plotted.

Projection Computations.

For the discretized grid in Figure 35, the projection computed for the first row with m homogeneous layers is given by

$$L_{proj_1} = \sum_{i=1}^{m} B_i(T,\nu) \cdot (1 - \tau_i(T, X_{1,2}, \nu)) \prod_{j=i+1}^{m} \tau_j(T, X_{1,2}, \nu) \ , \tag{23}$$

where $B_i(T,\nu)$ is the temperature- and wavelength-dependent Planckian (blackbody radiation) curve for voxel i, and $\tau_i(T, X_{1,2}, \nu)$ is the wavelength-dependent transmis-

www.manaraa.com

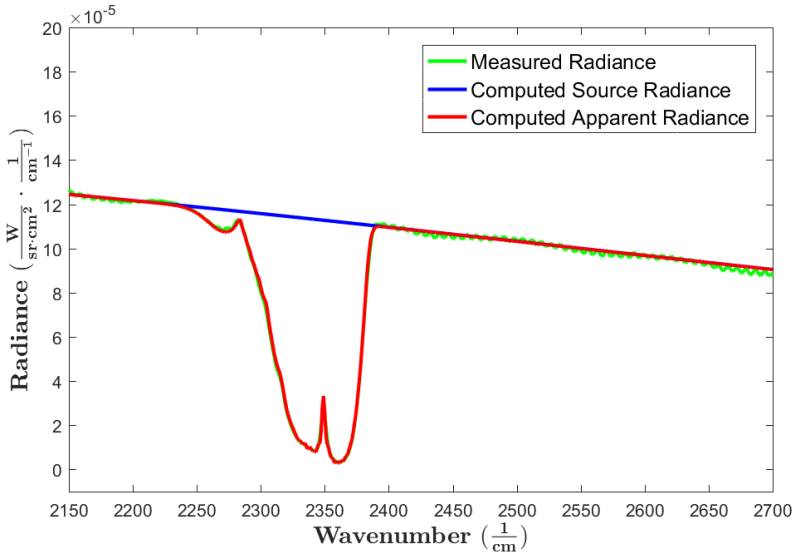

Figure 36: Measured apparent, computed source, and computed apparent spectral radiances for an in-scene gray-body emitter.

sion for voxel i for a given temperature (T) and concentrations ($X_{1,2}$). The product term simply shows that the radiation emitted from a particular voxel is propagating in the direction toward the observer and only has to go through subsequent layers.

The calculation at this point is known as the source quantity, where all the radiation so far is from the computational domain of interest. For a "distant" observer, this source is propagated through the atmosphere to the instrument aperture. The path that exists between the source and observer attenuates the source and also re-emits radiation according to its temperature. Thus the apparent (as seen through atmosphere) radiance arriving at the instrument aperture (L_{app}) is given by

$$L_{app} = B_{atm}(T,\nu) \cdot (1 - \tau_{atm}(T, X_{1,2}, \nu)) \; + \; \tau_{atm}(T, X_{1,2}, \nu) \cdot L_{source} \; , \qquad (24)$$

where $B_{atm}(T,\nu)$ is the Planckian for the atmospheric path at temperature T, $\tau_{atm}(T, X_{1,2}, \nu)$ is the transmission computed for the atmosphere, and L_{source} is a generic source radiance.

www.manaraa.com

The apparent radiance at the instrument aperture is now observed with the instrument itself. The instrument detects the radiation from the source, but not without affecting it. The optical elements in the system attenuate and re-emit themselves, and the detector has a response to radiation that is wavelength dependent. Also, noise terms associated with the detector and source radiation affect the signal reported. These effects of the system are addressed in the calibration of the instrument whereby the raw counts from the system are converted to radiometric units. Because all these system effects are present when the calibration is performed, the calibration gain and offset (assuming a linear detector response) for the system account for them. This calibration is performed by viewing multiple known radiation sources that span the dynamic range of the scene to be measured. This is discussed in further detail in Chapter V on the calibration of an IFTS HSI.

For an IFTS HSI, spectral resolution is a function of the mirror displacement from zero path difference (ZPD) [9] and is typically adjustable. Trade-offs of required resolution, time necessary to collect the data, and computational time must be considered when determining instrument resolution. For these computations, data was collected at 2 cm^{-1} which compromises some spectral resolution for collection time.

The apparent spectral radiance computed as in Eq. 24 must now be convolved with the spectral resolution of the imager. This decreases the resolution of the computed spectrum to match that of the instrument. This convolution is performed by transforming the computed spectra into the temporal domain and multiplying it by an apodization function. The Hann apodization function

$$w(n) = \frac{1}{2}\left(1 - \cos\left(\frac{2\pi n}{N-1}\right)\right) , \tag{25}$$

where $n \in \{0, 1, ...N\}$ for N samples, was chosen here to match that chosen during the calibration process where the raw temporal data was transformed into the spectral

www.manaraa.com

domain. Because the radiance projection is in the spectral domain, the inverse Fourier transform ($\mathcal{F}^{-1}$) is used to transform L_{app} from the spectral domain, into the temporal domain, where it is multiplied by $w(n)$ and the the Fourier transform ($\mathcal{F}$) is used to transform the product back to the spectral domain,

$$L_{con} = \mathcal{F}\big(\ \mathcal{F}^{-1}(L_{app}) \cdot w(n)\ \big)\ . \tag{26}$$

Because the Fourier transforms require periodicity in the function, the range of the measurements is used as a finite domain which is effectively repeated for infinity to allow this non-periodic function to be transformed. Also, the initial function in the transform must be smooth. If it is not, the transform will introduce high frequencies to approximate a jump in the data. For these reasons, the Hann apodization function in Eq. 25 is often a good choice. This function forces the temporal data to zero at the first and last sample. By doing this, it reduces the dispersion and aliasing errors. However, it is not without compromise. By forcing the interferogram to zero at the edges, some frequency content is lost and thus the resolution is decreased beyond what the mirror displacement would have dictated. In practice, this integral is evaluated at discrete points, and for computational efficiency, is padded with zeros to be in a domain range that is a power of 2. The FFT (fast Fourier transform) algorithm was used here for this computation.

The resultant convolved spectrum, L_{con}, is now directly comparable to a calibrated measured spectrum along a particular line of sight. All the projections are calculated in this same manner giving a set of $M + N$ spectral curves for comparison.

Resolution of Computations.

In order to capture the correct attenuation and radiation in the projection computations described above, the spectroscopic database used must be of adequate

www.manaraa.com

resolution to resolve the individual lines. With this resolution, the absorption or cross-section spectrum becomes a smooth function and will allow for correct radiative transfer computations. To adequately resolve the H_2O and CO_2 rotational-vibrational lines seen in the MWIR spectrum, the spectrum was generated at 0.125 cm^{-1}. In Figure 37, the CO_2 optical depth is shown at the spectroscopic database resolution and instrument resolution.

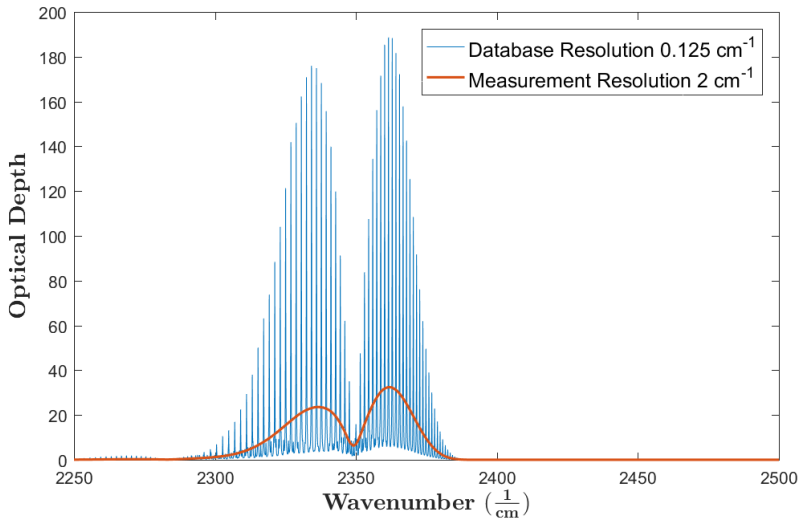

Figure 37: Optical depth of a 10-meter path length of 300K CO_2 at (blue) spectroscopic database resolution of 0.125 cm^{-1} and (red) instrument resolution of 2 cm^{-1}.

When the convolution of Eq. 26 is performed, spectral content is lost which affects the results computed. While high-resolution databases can drastically increase the number of computations, the convolution cannot be performed earlier in the process without introducing artifacts or giving an incorrect at-aperture spectral radiance. This impact is shown in Figure 38 where the radiative transfer was performed at both the instrument resolution and the database's high resolution. These computations were performed with a uniform grid temperature of $900K$ and a uniform CO_2 concentration of 0.02 mixing fraction, and a voxel linear dimension of 1 cm. Even in this simple scenario, the impact of high resolution computations can be clearly seen.

www.manaraa.com

By performing the convolution at each voxel throughout the domain, the spectral information regarding attenuation and re-emission is lost and the errors compound along the path. Based on the computation procedure, this result should not be surprising. This nonequivalence is to recognize that the convolution described in Eq. 26 to decrease the resolution does not commute with the radiative transfer performed in Equation 23. From this result, calculations are performed at the high resolution to reduce errors.

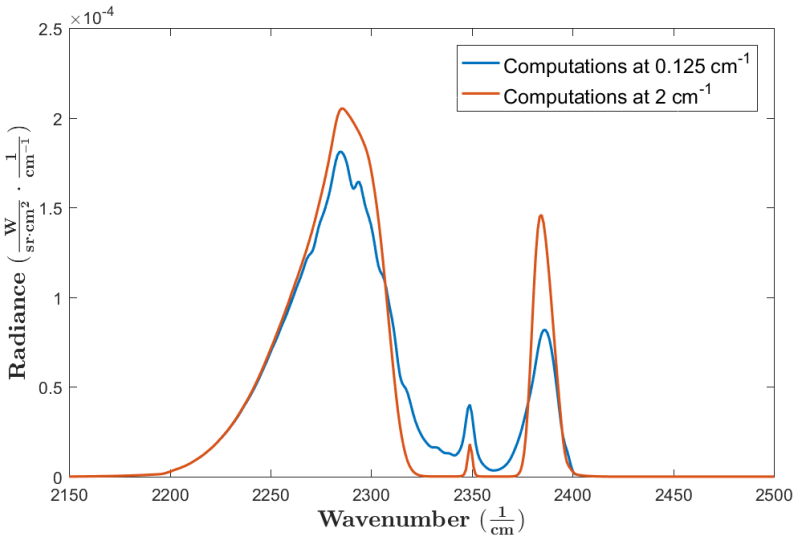

Figure 38: Projection calculations at (blue) database and (red) instrument resolutions.

7.2 Minimization Function

The minimization function (**F**) is developed to evaluate the goodness of a solution set and to compare calculated projections with measured data as well as enforce physical realities into the solution. A solution set is comprised of the unknown temperatures and concentrations for H_2O and CO_2. For the domain shown in Figure 35, there are $3 \cdot N \cdot M$ unknowns for which to minimize this function. This minimization function is similar to the approach used by Ma where it was developed for HT us-

www.manaraa.com

ing laser absorption measurements [17]. Modifications where made to accommodate measurement differences and assist in computations.

Projection Function.

The comparison to measured spectral data is the primary mechanism for evaluating a solution set of temperatures and concentrations for the domain. The radiance values are compared at the measured wavelengths, which motivated the projection computations of Eq 23. The difference function

$$\mathbf{D}(T^{dom}, X^{dom}) = \frac{1}{N+M} \sum_{i=1}^{N+M} \sum_{j=1}^{K} \left(p_m(L_i, \lambda_j) - p_c(L_i, \lambda_j)\right)^2 \tag{27}$$

is evaluated by squaring this difference for each projection i and each wavelength λ_j, where p_m is the measured projection and p_c is the computed projection.

The second sum spans the measured spectral range. This form appears similar to a 2-norm calculation with the exception that the squared difference is not divided by the square of the measured projection. This would have the effect of normalizing the error by the particular projection. If the projections were expected to be approximately the same value, or if the projections were not equally important, this method would be appropriate. By not dividing by the squared projection, the function will not weight the squared projection differences, which will prioritize large errors regardless of the measured projection values. Additionally, the $\frac{1}{N+M}$ term acts to normalize the total by the number of projections used to remove the effect that the dimensions would have on the error value so that the result given by $\mathbf{D}$ is the mean squared difference for a single projection. This is beneficial over Ma's approach [17] because it allows the grid spacing (or measurement resolution) to vary while still directly comparing the minimization function values.

www.manaraa.com

Smoothing Functions.

For the case of an IFTS HSI, the temperatures and concentrations within the domain for computation represent a mean value over time. The impact that fluctuations in the scene have on the measurements will be further analyzed in Chapter VIII. As a mean, the values are expected to be smooth from one voxel to the next, that is, not have drastic changes. To enforce the smoothing, a measure of how much a given temperature varies from the surrounding voxels must be generated. In Figure 39, the temperature at a voxel $T_{n,m}$, is compared with the average of all of the voxels surrounding it, eight in this case. Where the voxel is close to the boundaries, only the surrounding voxels, five for edges and three for corners, are considered in computing the average. This is mathematically shown in the smoothing function for temperature,

$$\begin{aligned} \mathbf{R}_T(T) &= \frac{1}{N \cdot M} \sum_{n=1}^{N} \sum_{m=1}^{M} \Big[T_{n,m} - \frac{1}{8} \cdot \big(T_{n-1,m-1} + T_{n-1,m} + T_{n-1,m+1} \\ &\quad + T_{n,m-1} + T_{n,m+1} + T_{n+1,m-1} + T_{n+1,m} + T_{n+1,m+1} \big) \Big]^2 , \end{aligned} \tag{28}$$

where the sum of the squared difference is summed for each voxel. Similar to the projection function, the sum is divided by the total number of voxels $(N \cdot M)$ to get a mean measure per voxel.

Equation 29 was used to enforce smoothing for concentrations of both H_2O and CO_2.

$$\begin{aligned} \mathbf{R}_X(X) &= \frac{1}{N \cdot M} \sum_{n=1}^{N} \sum_{m=1}^{M} \Big[X_{n,m} - \frac{1}{8} \cdot \big(X_{n-1,m-1} + X_{n-1,m} + X_{n-1,m+1} \\ &\quad + X_{n,m-1} + X_{n,m+1} + X_{n+1,m-1} + X_{n+1,m} + X_{n+1,m+1} \big) \Big]^2 \end{aligned} \tag{29}$$

www.manaraa.com

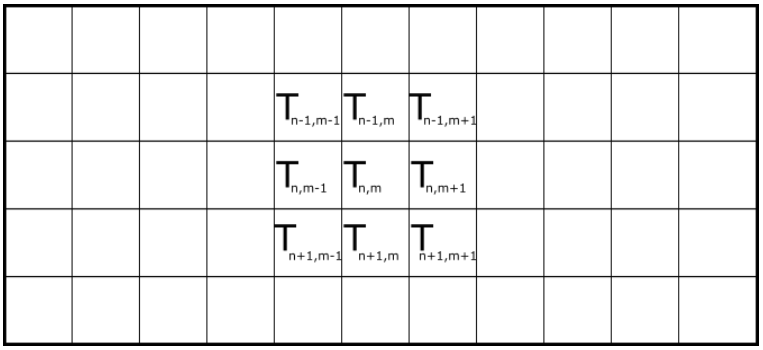

Figure 39: Temperature $T_{m,n}$ is compared with the average of all the surrounding voxels.

Total Minimization Function.

The minimization function is defined by combining the projection and smoothing functions,

$$\mathbf{F} \;=\; \mathbf{D} \;+\; \gamma_T \cdot \mathbf{R}_T \;+\; \gamma_{X_{H_2O}} \cdot \mathbf{R}_X(X_{H_2O}) \;+\; \gamma_{X_{CO_2}} \cdot \mathbf{R}_X(X_{CO_2}) \;. \qquad (30)$$

These smoothing equations give a measure of the smoothness, but this measure is in proportion to the values considered. Comparing temperature and concentration values, there are five orders of magnitude difference where the scaling parameters, γ, are necessary not only to adjust the quantities to be of the same order, but in order to specify the degree to which the smoothing is enforced. Comparisons with measured values were used to arrive at good values of these scaling parameters. Equation 30 is evaluated for a given solution set of temperatures and concentrations. By enforcing smoothing here, the non-physical solution sets that exist are eliminated.

7.3 Minimization Algorithm

A minimization algorithm is employed to adjust the solution set and reevaluate **F**. For this function, a unique solution does not necessarily exist and there may also

www.manaraa.com

be local minimums to which the solver can converge. The solver itself should employ some strategy so as not to get caught in a local minimum. In addition, the initial values of the solution set can affect the trajectory of the solver and should be chosen to be as close as possible to the actual solution so to approach the global minimum.

Algorithm.

Ma used the simulated annealing algorithm to minimize his function for HT [17], where (1) The minimization function **F** is evaluated for the initial conditions in the solution set (consisting of the temperatures and concentrations). (2) The solution set is then modified by a random amount in a random direction. (3) **F** is re-evaluated and this new value is compared with the first. (4) If the modification improves **F**, by making it smaller, the change is accepted. If **F** becomes larger, the change is either rejected or accepted based on a random variable with a probability proportional to how large a change in **F** was produced. That is, if the value of **F** increased dramatically, it would be much less likely to accept this change. (5) Steps (2) through (4) are repeated until a stopping criterion is met.

The stopping criterion for this algorithm occurs when the function **F** is at its minimum value. However, one can also stop when the changes that the algorithm finds acceptable are small enough compared to other sources of error. An example of the convergence of **F** for a 7×11 voxel domain is shown (on a log-log plot to see the rate of convergence) in Figure 40 where the x-axis is the error of **F** at iteration N (steps (2) through (4)) and the y-axis is error of **F** at the previous iteration (N-1). As the error gets close to the machine precision (approximately 10^{-16}), the favorable changes are more rarely found. This plot shows a linear convergence, as the slope of this line is less than one.

www.manaraa.com

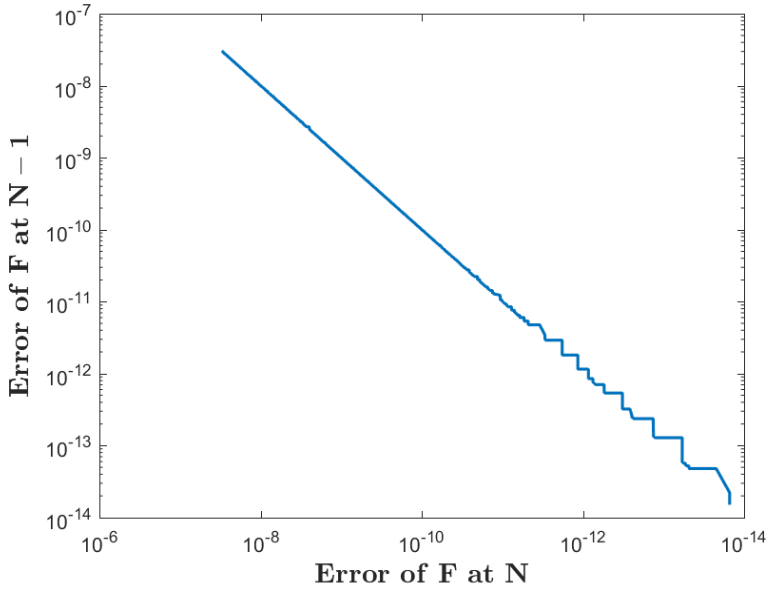

Figure 40: Solution convergence of **F** for a 7×11 voxel domain.

Initial Guess.

Initial values for all the temperatures and concentrations in the domain affect both the final solution and the iterations necessary for convergence. As such, it is important to initialize these values as closely as possible to the final solution. To this end, the temperature is first considered using a uniform concentration for the species. Since the temperature of the gas affects the relative line strengths driven by the Boltzmann distribution, by looking at the shape of a portion of the CO_2 spectrum measured, a temperature can be estimated. The temperature of all the voxels in the entire column is adjusted. The column temperature is continually adjusted until it is closest to the measured projection shape. This is then performed for all the columns. The same temperature estimations are then done for the row direction. At this point, the temperature relation is maintained from the column direction and all the row temperatures are adjusted by the same amount for each voxel in the row to affect the calculated CO_2 shape. In portions of the emission spectra of both H_2O

www.manaraa.com

and CO_2, the concentration of the gas drives the magnitude of the lines. By using these magnitudes, the concentrations can be scaled along the same procedure as the temperatures. All the concentrations of a column are assigned to uniform value and scaled to best match the measurements. This is done for both gases. Finally, the rows are computed using the relative column concentrations and the entire row is adjusted by the same increment to arrive at the concentration values that best match the measured projections.

This approach gives reasonable initial guesses that allow the minimization function to reach the same minimum for multiple runs. Figure 41 shows the arrival of multiple minimization runs with the same initial conditions. While the error is still being reduced with the number of iterations, the changes in the solution set are well below the uncertainty associated with the measurements; that is they are on the order of 0.01 K.

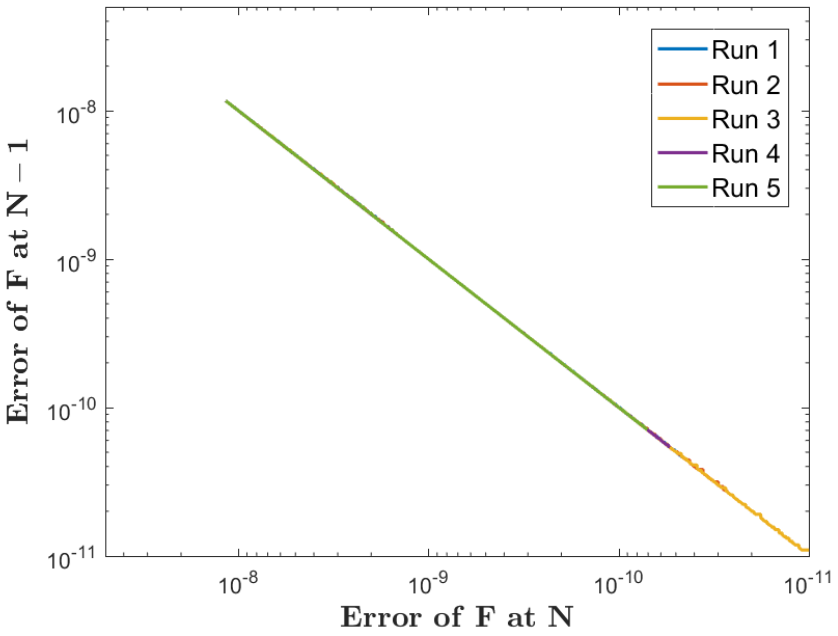

Figure 41: Multiple minimization routines for the same initial conditions.

www.manaraa.com

7.4 Smoothing For Domain Edges

Figure 42 shows profiles of measured radiances of exhaust planes and shows how quickly the average radiance falls off near the edges of the domain. This is especially true near the exit plane. This transitioning layer must be incorporated to capture attenuation effects of the cooler gases at the edges of the domain. However, this large change from one voxel to the next would be computed as unfavorable in the minimization function due to the smoothing portion. As a result, smoothing is enforced separately along the edges and for the interior of the domain. This allows the solution sets to arrive at solutions where the temperatures along the edges can be significantly lower than in the interior of the domain.

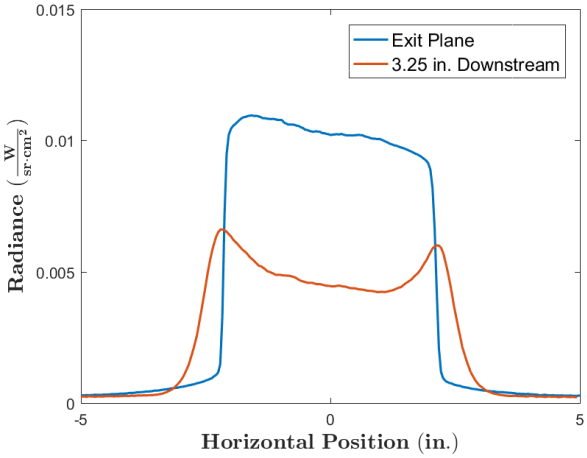

Figure 42: Radiance profiles of exit plane and 3.25 *in*. downstream.

7.5 Solution Set

The solution set for the exit plane associated with the HT algorithm is shown in Figure 43 and aligns well with thermocouple measurements that were made throughout the flow of the exhaust gases, which reported temperatures in the $940-$ to $970-K$ range throughout the center portions of the flow. In Figure 44, six exhaust planes are

www.manaraa.com

solved to arrive at solution sets throughout the flow. The red lines in (a) correspond to the solution sets shown in (b). These solution sets provide reasonable temperature values when compared to those measured by thermocouples. For the first three exhaust planes from the exit plane, the core temperatures of the solution sets agree to within $\pm 35\ K$ of those measured with the thermocouples. As the distance from the nozzle increases, an increasing deviation from the thermocouple data is observed peaking at approximately $+85\ K$ at $4.25\ in$. These larger differences result from different quantities being measured by the two instruments. The mean temperature is measured by the thermocouple while the IFTS HSI is measuring a mean spectrum resulting from fluctuating temperatures. As a result, when the turbulent fluctuations become large, the non-linear relationship between temperature and radiance largely impacts the HSI measurements. These deviations, caused by increasing turbulence in the flow will analyzed further.

Figure 43: Temperature solution set for the exit plane of the high-aspect-ratio nozzle.

7.6 Hyperspectral Tomography Summary

IFTS HSI measurements have been shown to be an effective data set on which to employ HT algorithms. Using two orthogonal measurements of a jet turbine exhaust

www.manaraa.com

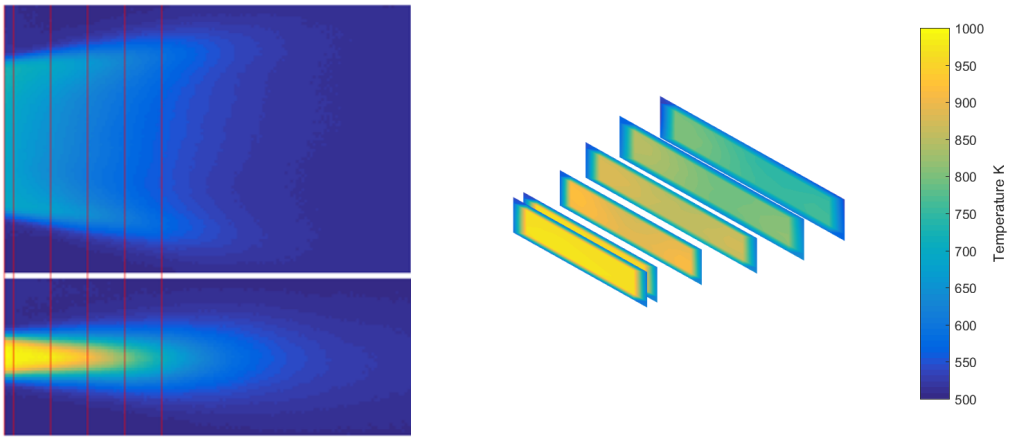

(a) **(b)**

Figure 44: Temperature solution sets for six exhaust planes of a high-aspect-ratio nozzle at (1) the exit plane and (2) 0.25, (3) 1.25, (4) 2.25, (5) 3.25, and (6) 4.25 in. downstream from exit plane.

plume, this algorithm provided a temperature and species concentration solution for 2D planes in the flow. The smoothing parameters used in the computations were approximately the same values as those used by Ma and for the exhaust plane solution sets near the nozzle, the error was well within the $35K$ that Ma observed [19]. Further from the nozzle, the difference between the solution sets and thermocouple data increased. These deviations are a result of the measurement devices responding differently to turbulence in the flow. While the thermocouple measures a mean temperature, the IFTS HSI measures a temporally averaged spectrum due to the temperature fluctuations. This distinction requires further analysis and refinement in the HT algorithm.

www.manaraa.com

VIII. Turbulence Effects On Hyperspectral Tomography

8.1 Introduction

The solution sets evaluated in Chapter VII represent a reasonable solution. However, a trend exists with the solution sets when compared with collected thermocouple data. In Figure 45 (a), both the average core temperature values of the solution set (solid line) and collected thermocouple data (dashed line) are shown for the six exhaust planes depicted in Figure 44. In Figure 45 (b), the residuals are plotted for each plane. Ma found in his application of hyperspectral tomography a solution within 35 K of measured temperatures [19]. The first three planes here give solutions within this tolerance when compared to the thermocouple data. However, as the planes get further from the nozzle exit, the solution set is increasingly over-predicting the temperature values.

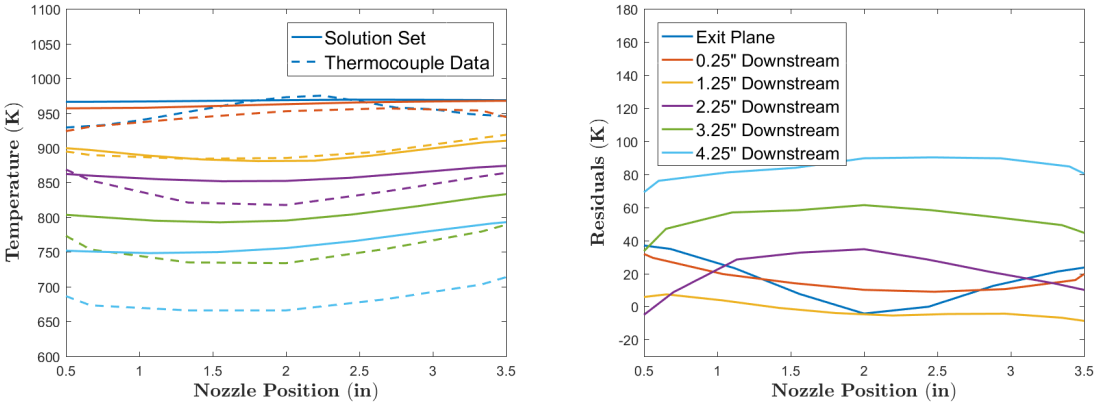

Figure 45: Solution sets compared with measured thermocouple data for six exhaust planes.

As will be shown, this effect is a result of turbulent fluctuations in the exhaust plume and how these fluctuations are measured with both a thermocouple and an interferometer-based hyperspectral imager. Calibrated infrared imagery spanning the

www.manaraa.com

CO_2 emission lines centered at $4.25\mu m$ was collected during this test which provides a measurement of radiance fluctuations in the scene. By examining the relation of radiance to temperature of the CO_2, these fluctuations can be related to the temperature fluctuation in the path. Using a model of isotropic turbulence, these fluctuations can be recreated using a simulated domain. This synthetic data set provides insight into not only the cause of the over-prediction of temperature shown in Fig. 45, but how to address it to achieve a more accurate solution set.

8.2 Turbulent Fluctuations

In addition to hyperspectral imagery of this exhaust flow, calibrated infrared imagery was also collected as discussed in Chapter V. This data provides spectrally integrated imagery of the flow at $180Hz$ which provides valuable information on the radiance variation of the flow due to CO_2. The variation seen in Figure 46 shows the changes in radiance associated with the temperature and concentration fluctuations in the flow field observed at two snapshots of time. As this imager is measuring a 2D projection, it is important to note the resulting radiance measured is due to local temperature and concentration variations that propagate through other fluctuating layers within the flow.

By selecting a portion of the flow and observing it in time, the radiance fluctuations can be plotted. This is shown in Figure 47 where a point was selected close to the exit plane and at 4.25 *in.* downstream in the flow. Radiance fluctuations in (a) are shown for the points identified in (b). To better observe the distribution, a histogram can be plotted for each of these two locations. Figure 48 shows a histogram for (a) the location near the nozzle, and (b) 4.25 *in.* downstream in the flow.

These histograms show how the radiance fluctuations increase with distance from the exit plane. Also, the distribution observed here does not appear Gaussian. While

www.manaraa.com

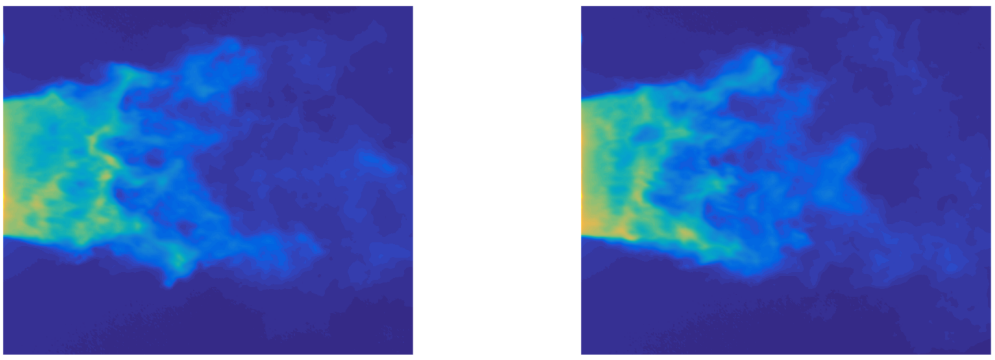

(a) **(b)**

Figure 46: Infrared radiance images taken at two time instances show CO_2 temperature and concentration fluctuations.

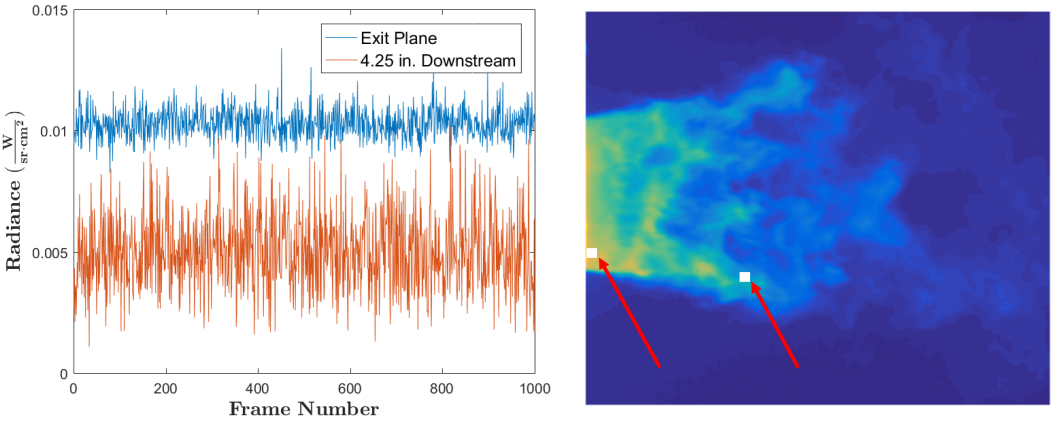

(a) **(b)**

Figure 47: (a) Temporal turbulent fluctuations for points selected in Image (b).

for isotropic turbulence, a Gaussian distribution of temperature is required, for measured radiance associated with the flow, this is not the case. The non-linear relationship between temperature and radiance (in this case due to gases) produces a histogram that appears weighted on the upper end. The relationship between temperature and radiance can be shown for this particular flow field using the spectroscopic databases. During the process of hyperspectral tomography in Chapter VII, the mean concentration of CO_2 for the flow and atmospheric path were determined. In conjunc-

www.manaraa.com

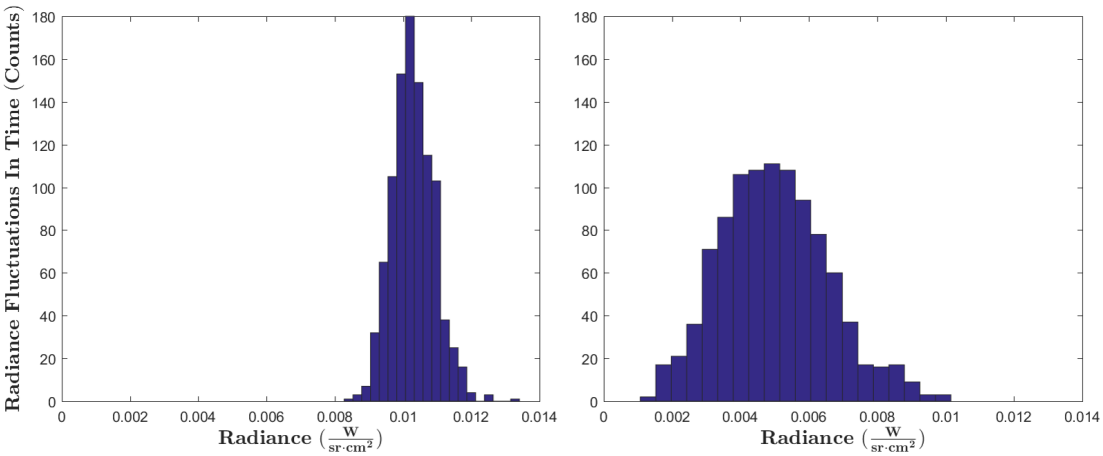

Figure 48: Radiance histograms for the exit plane and 4.25 *in.* downstream in the flow.

tion with path lengths, a relation between the temperature of a homogeneous plume and radiance associated with it can be determined. This relation is plotted in Figure 49 where the temperature was varied from 500 to 1200 K to arrive at the in-band radiance. Observing this relation of radiance to temperature of CO_2, the radiance distribution should not be expected to be Gaussian. Connecting the radiance distribution to a local temperature distribution within a voxel will be further examined later.

8.3 Mean Temperature and Radiance in Turbulence

For isotropic turbulence, the temperature at a given location in the flow fluctuates in some uniform distribution about a mean. To measure this mean temperature, thermocouples may be used. For many flows, the rapid changes in temperature due to turbulent eddies in the flow are too fast for the thermal mass of the thermocouple to respond to. As a result, the thermocouple reaches an equilibrium state where it is relatively constant over time, which is the mean temperature. The total mean temperature can then be calculated as a function of the Mach number and the specific-

www.manaraa.com

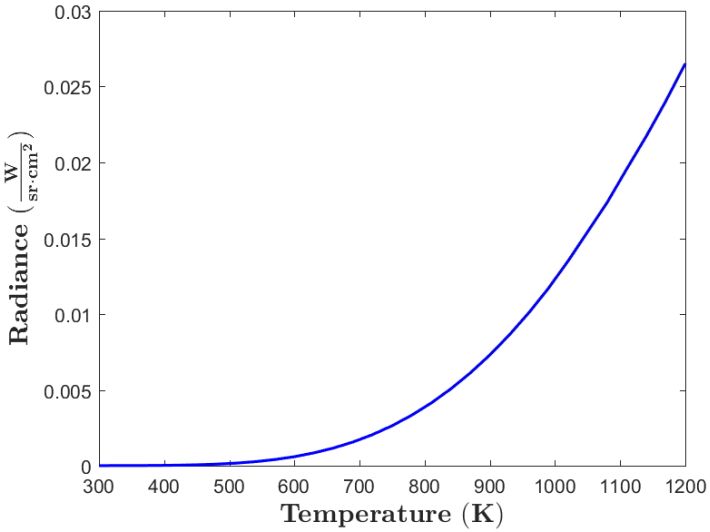

Figure 49: In-band radiance as a function of temperature relationship for the apparent 1 *in*. flow.

heat ratio of the gas [33]. These total mean temperatures are the values which were compared with solution sets in Fig 45.

In the hyperspectral tomography algorithm, an implicit assumption was made about how these temperatures relate to the measured spectral radiance. Specifically, that a mean temperature solution would reproduce the spectrum measured with an interferometer-based HSI. However, in order to reduce the effects of turbulent fluctuation on the measured spectra, many interferograms from the HSI are averaged together as seen in Chapter V. The resultant spectrum of the measurement represents not a spectrum of the mean temperature but a mean spectrum produced by the temperature variations. In other words, the HSI data represents the average spectral distribution over time. How then do the average spectra and the spectra generated by the average temperature compare? As previously shown, for a single homogeneous layer, the relationship between temperature and radiance is non-linear and therefore more analysis is necessary.

www.manaraa.com

8.4 Statistical Turbulence Modeling for Radiative Transfer

In order to resolve this, a statistical model of isotropic turbulence can be generated to produce both of the conditions just described. In the first case, the mean temperature of a hypothetical flow, with similar conditions to that which was measured, is used to compute the spectral projections. For the second condition, the temperatures throughout the flow will be randomly distributed about some mean value of temperature to reproduce an isotropic turbulent case. In each random instance, the spectral projections associated with that grid will be calculated. In the end, all the spectra for each projection will be averaged to represent the HSI measurement conditions. These two methodologies can then be compared for different turbulence cases and the impact of the implicit assumption quantified.

Projection Computations for a Mean Temperature Grid.

The domain was generated to be a similar shape to the measurements performed. A distribution of mean temperatures was chosen to give values that span the approximate temperature range encountered in the exhaust planes. The mean temperatures selected are shown in Figure 50 where the 7×15 voxel domain is shown. Mean concentration values of H_2O and CO_2 were set to approximately those which were measured. The distribution of the mean concentrations follows the same relative shape as the temperature profile as they are driven by the same turbulent eddies. In measurements, the domain is observed through an atmospheric path. The atmospheric path from the measurements is inserted into this scenario to give the same effect on the spectra. Using this domain setup, the projections were calculated as described in Chapter VII. The 22 projections associated with the synthetic domain are plotted in Figure 51. Qualitatively, these projection values are of similar shape and order to the measured data.

www.manaraa.com

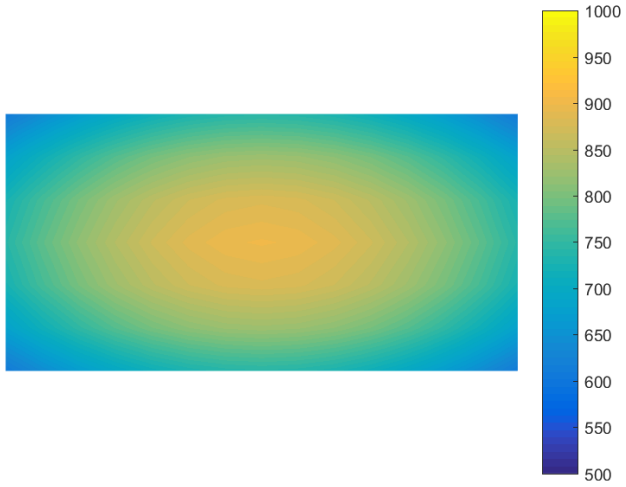

Figure 50: Mean temperature distribution in synthetic domain.

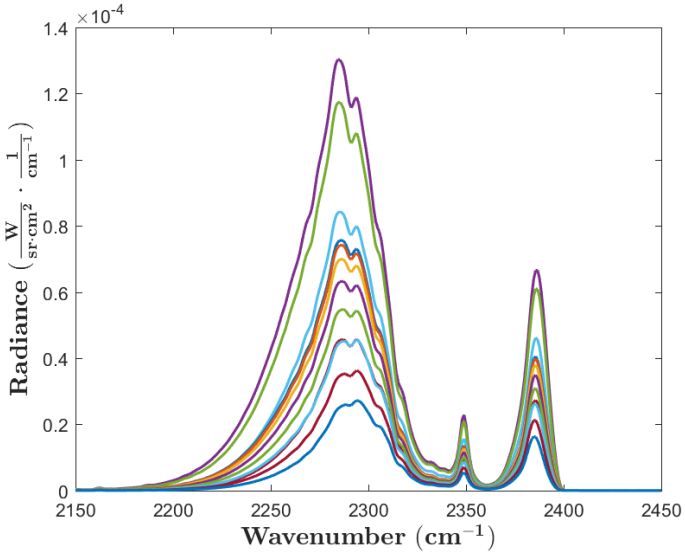

Figure 51: Computed projections of synthetic domain using mean temperatures as shown in Fig 50.

Projection Computations for a Gaussian Temperature Distribution.

Each mean temperature in this grid is now used as the center of a Gaussian distribution of temperature with some standard deviation. The probability distribution

www.manaraa.com

is

$$f(x \mid \mu, \sigma^2) = \frac{1}{\sqrt{2\pi\sigma^2}} e^{-\frac{(x-\mu)^2}{2\sigma^2}} , \tag{31}$$

for a temperature (x), occurring about a mean temperature (μ), with a standard deviation of σ.

A temperature for a given voxel is randomly chosen with a probability associated with Equation 31. This random selection of temperature is performed for each voxel which has its own mean temperature and distribution. Figure 52 shows the selection of a temperature, represented by the red dots, for four voxels about a mean.

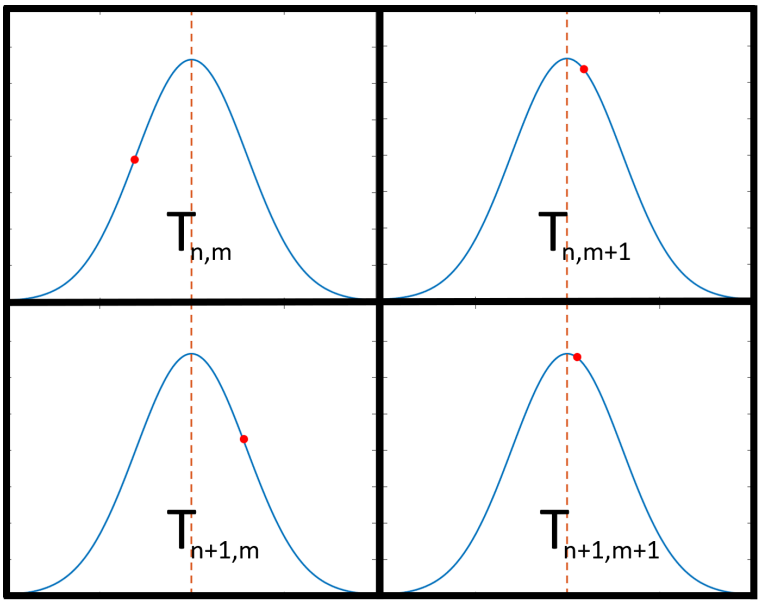

Figure 52: Temperatures randomly selected with Gaussian probability centered at each voxel's mean temperature.

When applied to the entire grid domain, this represents a set of temperatures for one instance in time. For this instance, the 22 spectral projections are now calculated for the domain. The random selection is then repeated for many instances in time. At each instance, the 22 projections are calculated. This is continued until additional instances no longer significantly change the mean spectrum for each projection. In Figure 53, 1000 instances for a single projection are plotted. This plot represents

www.manaraa.com

a single line-of-sight spectral measurement in time. By averaging these spectra, the value that the FTIR-based HSI measures is arrived at, which is the time-averaged spectrum due to temperature fluctuations. This is also shown in red in Fig. 53.

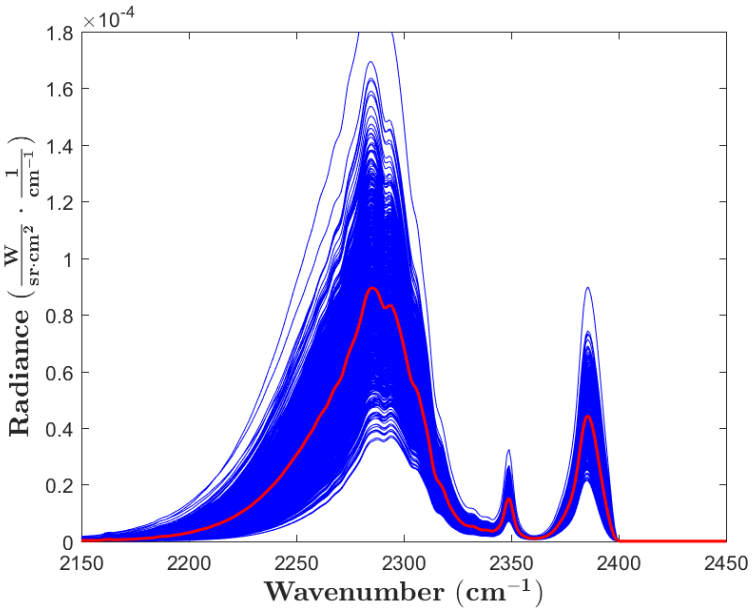

Figure 53: A single projection with 1000 randomly chosen instances. The mean spectra is also plotted in red.

Interestingly, each of the spectral instances can be band-integrated to produce a radiance value as a function in time. This is equivalent to the radiance fluctuations measured by the imager in a single pixel over time. This synthetic imager data is shown in Figure 54 with the temporal fluctuations shown in (a) and the histogram in (b). This distribution reasonably represents the measured data observed for the turbulent case. Like the measured data, a high side weighted distribution is observed in the histogram with a mean radiance of similar magnitude.

Projection Computations for Varying Levels of Turbulence.

The variation in the band-integrated radiance can be used to generate a desired level of turbulence. By adjusting σ for the synthetic domain, a correlated turbulence

www.manaraa.com

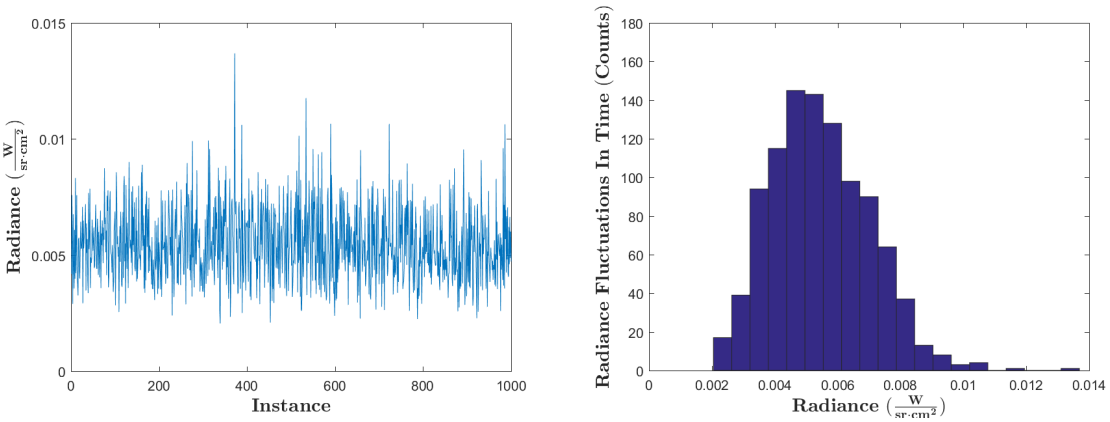

Figure 54: (a) Integrated radiance for a single projection per randomly chosen instance and (b) a histogram of the these radiance fluctuations per instance.

condition for a measured plane is generated. The spectrum for each of these turbulence conditions is compared to the mean temperature spectrum for a single projection in Figure 55. As the turbulence is increased, the temporally averaged spectrum for this projection increases in radiance, departing further and further from that of the mean temperature projection. This departure and the direction of the departure are of particular interest as they indicate the degree to which the temperature solution set for more-turbulent planes will deviate from the measured mean temperatures.

8.5 Significance of Turbulence Model

From these synthetic turbulent cases, the mean temperature and the temporally averaged spectra are generated as a function of turbulence. This connects the error induced by the temporal averaging of spectra to a directly measurable turbulence condition. This also shows that for the exhaust planes close to the nozzle, where the turbulence is lower, the impact of the temporal averaging is minimal (as was shown in Fig. 45).

www.manaraa.com

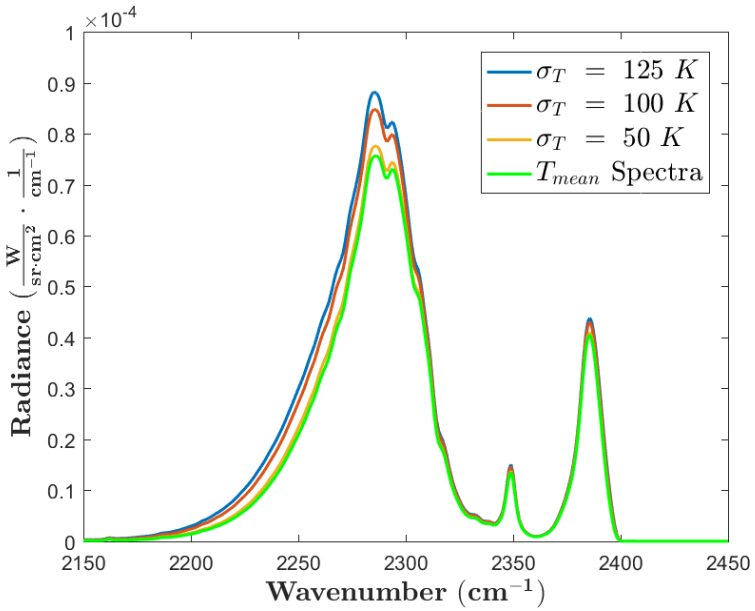

Figure 55: Mean Turbulent Spectra and Spectra for the Mean Temperature for a Single Projection.

8.6 Resolving Turbulent Effects

To quantitatively evaluate the effects of turbulence and proposed solutions, a high turbulence case ($\sigma_T = 125\ K$) will be used. In Figure 56, the residuals of all 22 projections of the synthetic domain between the mean temperature and temporally averaged spectra are plotted. The solutions discussed will be an attempt to reduce the magnitudes of these residuals. The residuals in each of these projections are positive, indicating that the actual mean temperature grid solution will produce spectral curves that are too low in the case of turbulent flow (again, as shown in Fig. 45).

Elevated Temperature Solution.

To reduce the residuals of Fig. 56, one approach is to use elevated temperatures throughout the synthetic domain to compensate for the radiance differences. By incrementing the temperature of the grid up by small amounts, the best possible fit is plotted in Figure 57. In order to generate this best fit, the domain was increased

www.manaraa.com

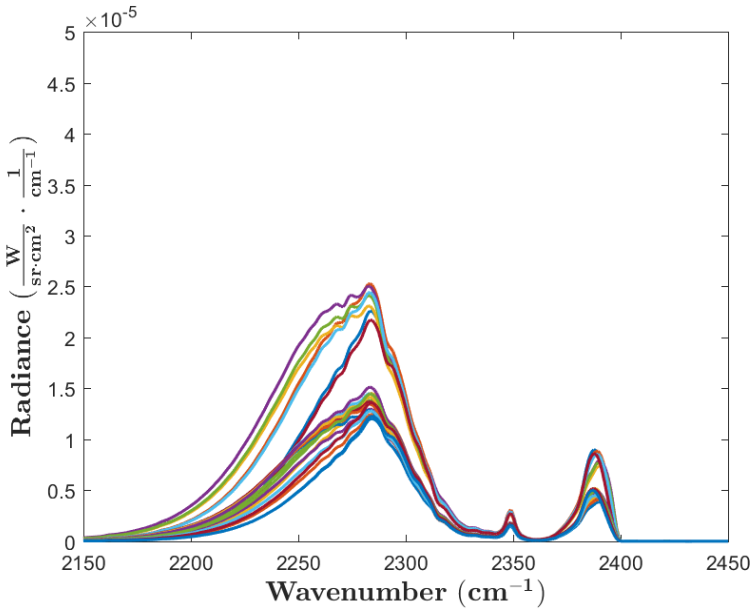

Figure 56: Residuals between mean temperature spectrum and temporally averaged spectrum for all 22 projections of the synthetic domain.

in temperature (and corresponding concentration) by approximately 41 K. Because elevated temperatures were used to minimize the residuals, the spectral distribution is not completely accurate which is shown in the residuals of Fig. 57. This solution presumes that the best possible fit is a result of a uniform increase in temperature to the entire grid domain.

Fit To Mean Temperature.

To find the best possible single temperature solution, the synthetic domain can be inserted into the HT algorithm from Chapter VII. This allows for any solution, and gives a more analogous situation to that of the measurements. Because the actual mean temperatures are known, a comparison of error of the optimal solution can be assessed. In Figure 58 (a), the temperature solution using the HT algorithms is shown. In (b), the difference between this solution and the mean temperature solution is displayed. The HT algorithm found the best solution possible given the

www.manaraa.com

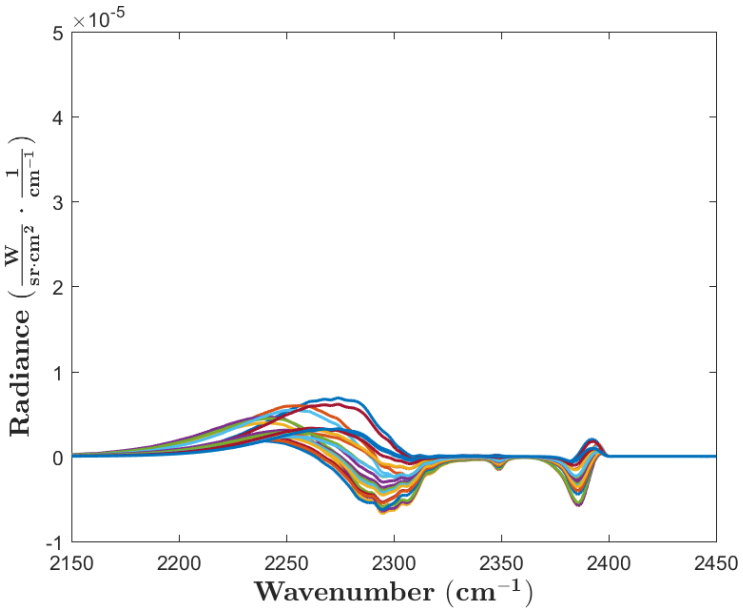

Figure 57: Residuals of all the projections between the mean temperature spectrum and mean turbulent spectrum with uniformly elevated mean temperatures.

constraints of smoothness and the projection comparisons. Because the actual solution is a result of fluctuations in temperature and concentrations, this best solution is just a combination of incorrect temperatures that best approach the solution. In this turbulent case, the algorithm found that an increase in the temperature throughout the grid better matched the spectral distribution, and consequently lowered the concentrations throughout the solution grid to appropriately adjust the magnitude. This is seen in the residuals of the projections shown in Figure 59.

Mean Spectrum Inside a Voxel Solution.

For a given voxel, a composite spectrum can be generated made up of multiple temperatures to generate a spectral distribution that is a combination of multiple temperatures instead of a single temperature. To do this, a high resolution spectrum is generated for each of six discrete values about a mean. These values and their weights are determined by a Gaussian distribution. The weighted average is then

www.manaraa.com

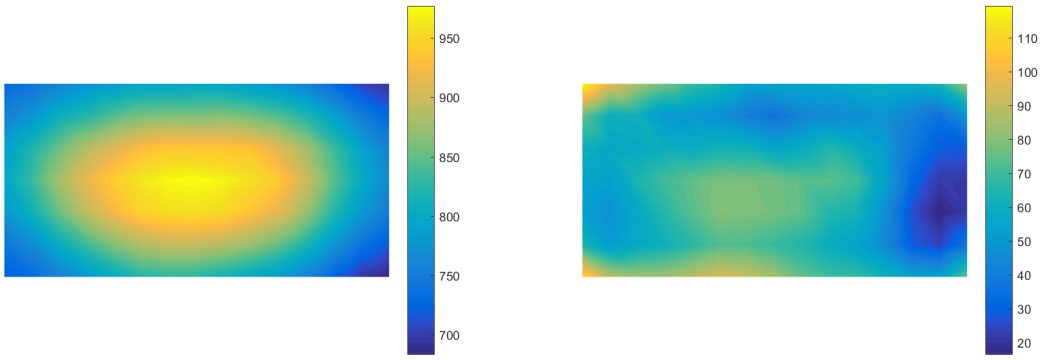

(a) **(b)**

Figure 58: (a) Temperature solution of synthetic domain using HT algorithm and (b) the difference between HT solution and the mean temperature distribution.

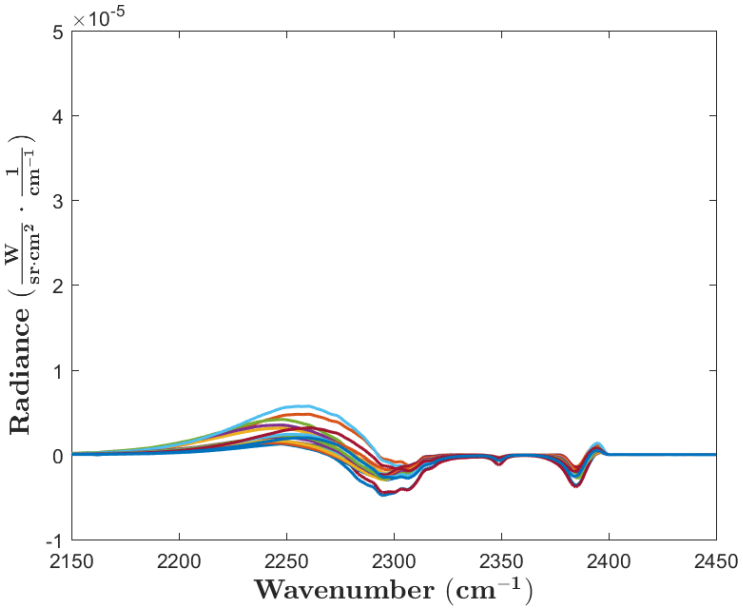

Figure 59: Residuals between all the projections using the HT algorithm on the synthetic domain and that of the temporally averaged spectrum.

taken to generate a weighted absorption cross-section and emission spectrum. By using a spectrum associated with a distribution of temperatures, a better solution can be found. The best match achieved in this case however, does not match the actual distribution of temperatures. In this case, a standard deviation of over 200 was required to achieve the best overall solution. Because this distribution of temperatures

www.manaraa.com

does not match the actual projection spectral distribution, it results in errors in other portions of the spectra. The residuals of this solution are seen in Figure 60. Again, the overall error is decreased for the projections, but the correct spectral shape is not achieved. In a similar approach with the elevated mean temperature, the HT algorithms can be run with this computational method and lower residuals can be achieved. However, the same problem exists whereby the best solution is achieved by incorrectly adjusting temperatures and concentrations.

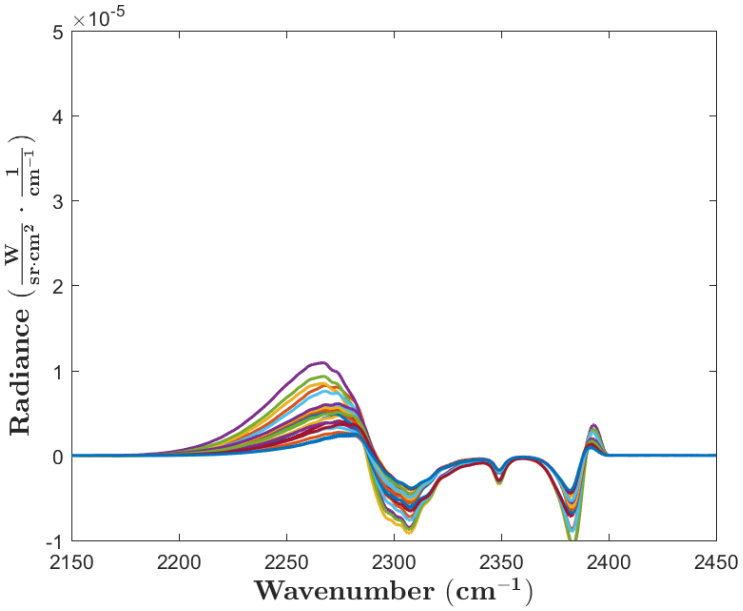

Figure 60: Residuals between all the projections using the mean temperature and that of the mean spectrum per voxel approach.

Discrete Temperature Fluctuation Solution.

The turbulent flow and resulting average spectral projections were generated based on a Gaussian distribution about a mean temperature. As such, it seems appropriate to use the same mechanism to reproduce better results. However, computationally, a continuous distribution of temperatures about the mean value requires evaluation of the absorption cross-sections and emission spectra associated with every temperature

www.manaraa.com

and concentration of H_2O and CO_2 for every iteration. When considering $100s$ to $1000s$ of iterations being evaluated at high spectral resolution, it is much more advantageous to use only several discrete values about a mean temperature if possible.

For the following approach, multiple discrete values will be used for each voxel instead of the continuous distribution used to generate the turbulence. A number of iterations will be used to examine how many are necessary to get reasonable agreement with the original projections. The random Gaussian distribution is now effectively binned into discrete values so that for each iteration, the absorption spectra and emission spectra have already been evaluated, leaving only the projection evaluation to be done. Figure 61 shows a histogram of 1000 iterations with a mean temperature of 900 K. For the projections to be computed, this is performed on every voxel. The projections are then computed with a given voxel being one of these five discrete values.

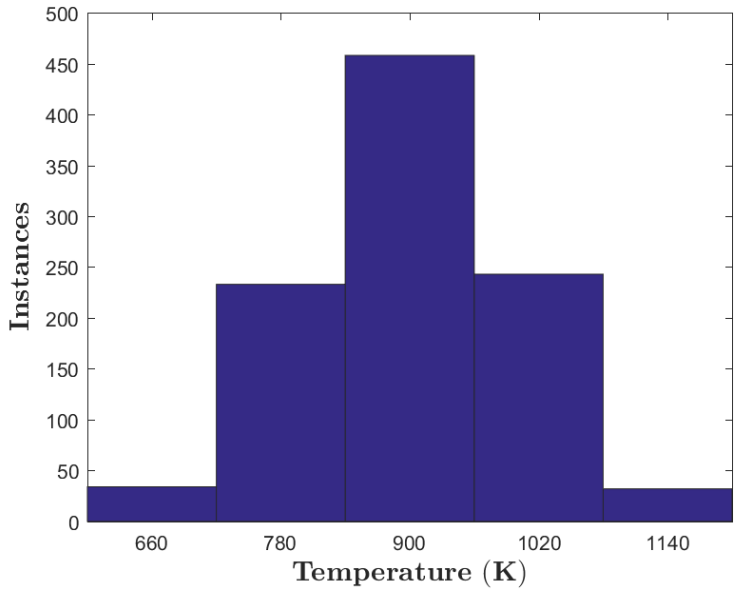

Figure 61: Histogram of 1000 instances using five discrete temperature values to represent a voxel with a mean temperature of 900 K.

The projections are now computed for each instance and compared to the contin-

www.manaraa.com

uous distribution solution. In Figure 62, the solution of one projection as well as the residuals for all the projections are plotted in (a) for 10 iterations and in (b) for 50 iterations.

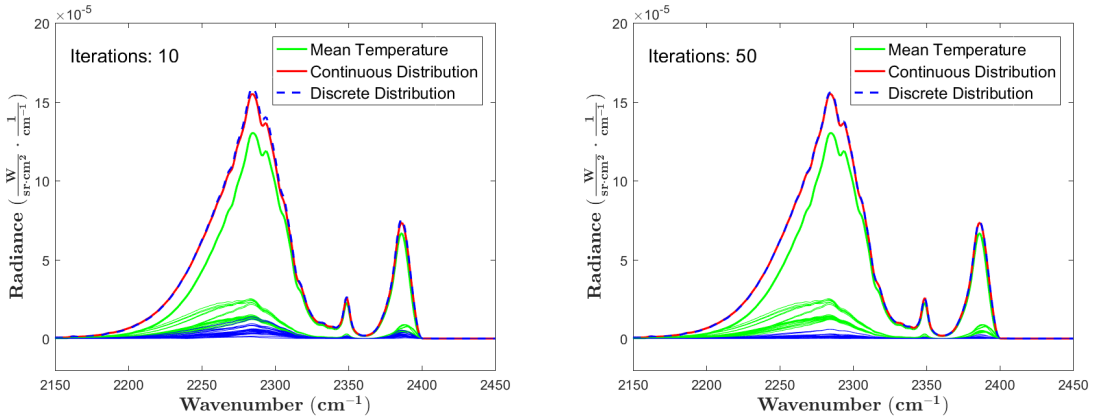

(a) (b)

Figure 62: Residuals between all the projections using the continuous temperature distribution and that of the discrete temperature fluctuation for (a) 10 iterations and (b) 50 iterations.

While the continuous distribution of temperature solution was performed for 1000 iterations, after only 50 iterations using just five discrete temperature values, a solution very close to the actual solution was achieved. This was further minimized by continued iterations. These plot were based off of five discrete values that spanned three times the standard deviation. Various numbers of bins were used to test the minimum necessary in order to balance computational time and accuracy. Below five, the error was not adequately reduced, and beyond this, unnecessary computations were performed. While the discrete temperature solution is more computationally intensive than the other solution methods, it is a balanced way to provide a much closer representation of the actual spectra.

www.manaraa.com

Continuous Temperature Fluctuation Solution.

The continuous temperature fluctuation solution is the mechanism by which the solution projections were produced. As such, this logic is circular to show it produces a valid solution. However, what can be analyzed is the number of iterations within the continuous distribution necessary to produce the average spectra used. Previously, 1000 iterations were used to compute the temporally averaged spectra. In Figure 63, a 10 iteration solution is compared to the 1000 iteration solution and the residuals for all the projections are computed. By using just 10 iterations, the overall errors are greatly reduced. This solution, because very few iterations are necessary, could be implemented directly into the algorithms with an overall computational impact directly proportional to the number of iterations.

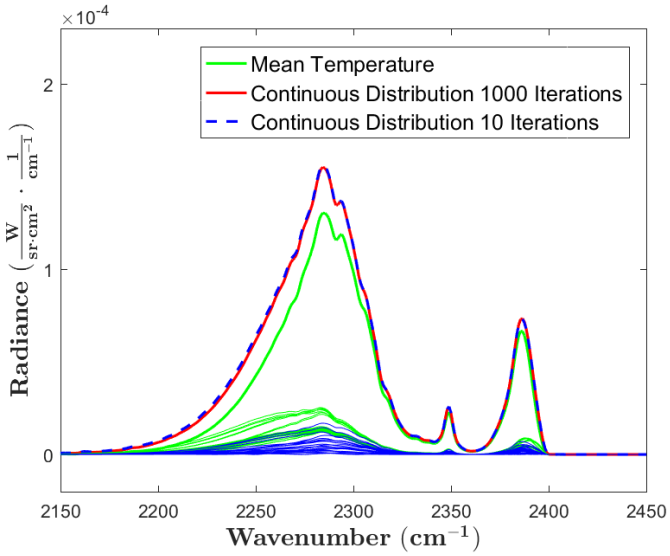

Figure 63: Residuals of all the projections using the mean temperature solution and a continuous distribution with 10 iterations compared with the continuous distribution solution for 1000 iterations.

www.manaraa.com

8.7 Turbulence Modeling and Hyperspectral Tomography

In order to implement turbulence effects into the HT algorithms, the influence must be considered at every iteration. At each step, the change under test is evaluated to see if it reduces the minimization function. The turbulent fluctuations about a mean temperature and concentrations only affect the projection portion of the minimization function in Equation 27. Whatever turbulence solution is implemented must account for its influence prior to the comparison with the HSI measurement data. As was shown in the Chapter VII, the propagation and emission of each voxel must be computed at a high resolution as to not introduce errors. After this computation, the high resolution spectra is convolved down to the resolution of the HSI. Because the measurements are being made at this resolution, the temporal effects of turbulence are also measured at this resolution. Thus, the turbulence solution implementation will occur at this point in the HT algorithm.

For flexibility and ease of implementation, an array is input into the algorithm that specifies a change in temperature and concentration for each voxel relative to a mean for each instance. With this implementation, the solution set is still a single mean temperature value. However, during each computation of projections, the entire domain is fluctuated around the mean values for a number instances. Using this approach, the algorithm isn't affected by the distribution chosen or the number of iterations chosen. A continuous distribution, discrete values, and different numbers of iterations can be evaluated.

Determination of Temperature Fluctuation By Histogram Comparison.

For a given solution set, the amount of temperature fluctuation must be determined. The same approach as in the synthetic domain can be used, but now with the actual solution domain. The mean temperature solution was achieved through

www.manaraa.com

the HT algorithm in Chapter VII. Each voxel in this mean solution is now fluctuated with some standard deviation to generate a spectrum for each projection for multiple instances. Each of these instances is band integrated and the radiance fluctuations from a given projection is produced. This radiance fluctuation for a particular line of sight is then compared to the SBFP Imager radiance fluctuations at the same location.

For a given solution plane, a single standard deviation of temperature is first evaluated. While the implementation does not require this, the turbulence increases downstream of the exit nozzle and as such the fluctuations are more influence by the distance from the nozzle. In order to evaluate a specific standard deviation for a particular plane, the SBFP Imager radiance histograms are used as the measure. As shown in Figure 64, for each of the pixels selected in (a), a histogram of 1000 frames is produced in (b). These selected pixels correspond to the projections computed from the solution sets.

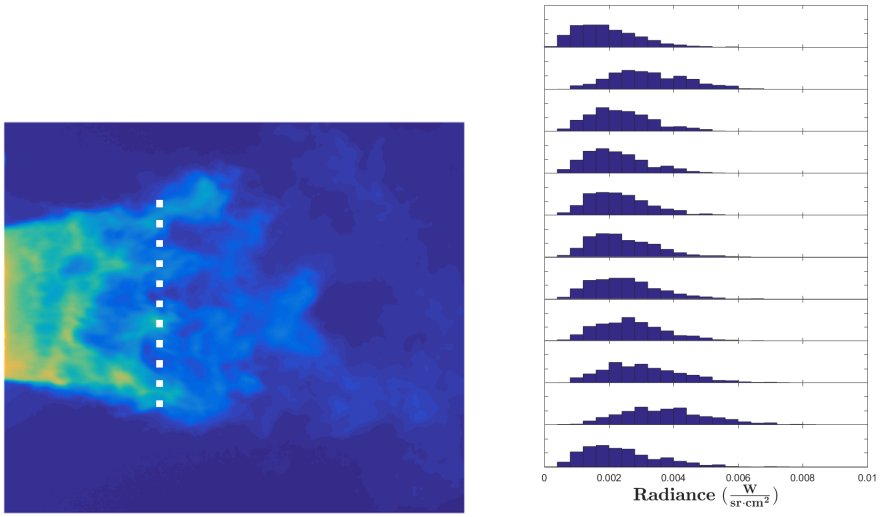

Figure 64: (a) Selected pixels in the SBFP imager and (b) the histograms of the their radiance fluctuations.

In the high turbulent cases, the mean temperature achieved by the algorithm was

www.manaraa.com

higher than that measured by the thermocouples. This presents a problem because the thermocouple temperature solution is that which is fluctuating, resulting in the histograms shown in Figure 64. Consequently, an iterative approach must be taken in which an amount of fluctuation is used in the HT algorithm to produce a better solution set of temperatures, which then is used to determine a better amount of fluctuation.

To compare the histograms of the fluctuating solution set with the SBFP imager fluctuations, the Bhattacharyya distance, $D_B(p,q)$, is used [3]. This is defined as

$$D_B(p,q) = -\ln\left(BC(p,q)\right) , \tag{32}$$

where the two distributions are p and q. The Bhattacharyya coefficient, $BC(p,q)$, is defined as

$$BC(p,q) = \sum_{x \in X} \sqrt{p(x) \cdot q(x)} , \tag{33}$$

where $p(x)$ and $q(x)$ are over the same discrete points in the domain X.

The Bhattacharyya distance is at a minimum when the two distributions best overlap. Additionally, elevated temperatures are expected in the initial fit so the distribution is offset. The mean radiance of each distribution, prior to being compared, is corrected to the mean radiance observed by the imager. This emphasizes the importance of the radiance distribution over its magnitude. By the last iteration of calculating the fluctuation amount, the adjustments to the mean are no longer necessary.

The Bhattacharyya distance is calculated for each line of sight specified in Figure 64. The mean of these Bhattacharyya distances is computed for a given standard deviation. The standard deviation is then adjusted until the minimum distance is reached. For each test case, 1000 instances are produced. For the exhaust plane 4.25

www.manaraa.com

inches downstream, the histograms for standard deviations of (a) 100 K, (b) 110 K, and (c) 120 K are plotted in Figure 65. Based on the Bhattacharyya distances of $D_B = 0.0108,\ 0.0078,\ 0.0124$ respectively, the best fit standard deviation is $110K$. Again, this fluctuation is centered about an elevated mean temperature and therefore the standard deviation providing the best fit is artificially low.

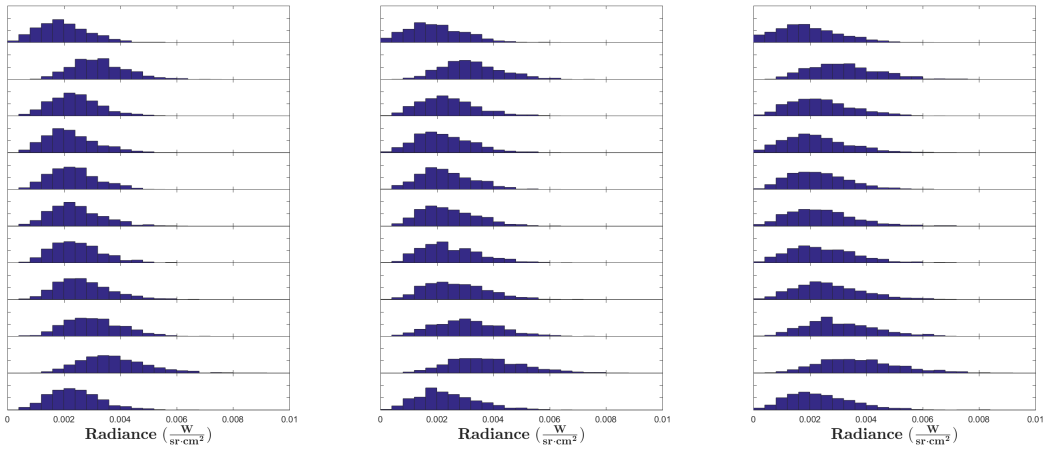

(a) **(b)** **(c)**

Figure 65: Histograms for fluctuating temperature about the single temperature solution for a standard deviation of (a) 100 K, $D_B = 0.0108$ (b) 110 K, $D_B = 0.0078$ (c) 120 K, $D_B = 0.0124$.

The HT algorithm is now resumed using the previous single temperature solution as a starting point. At each step, the fluctuations with a standard deviation of 110 K are now used. In Figure 66 (a), the solution set for the fluctuating temperature is plotted and in (b), both the single and fluctuating core temperature profiles are shown. By adding the fluctuations, the mean core temperatures have clearly been lowered.

Using this new solution set, the fluctuation histograms are regenerated and compared to the SBFP Imager. Where before the best fit aligned to a standard deviation of 110 K, now the lowest Bhattacharyya distance is achieved with a standard deviation of 130 K as shown in Figure 67. Using the updated standard deviation value,

www.manaraa.com

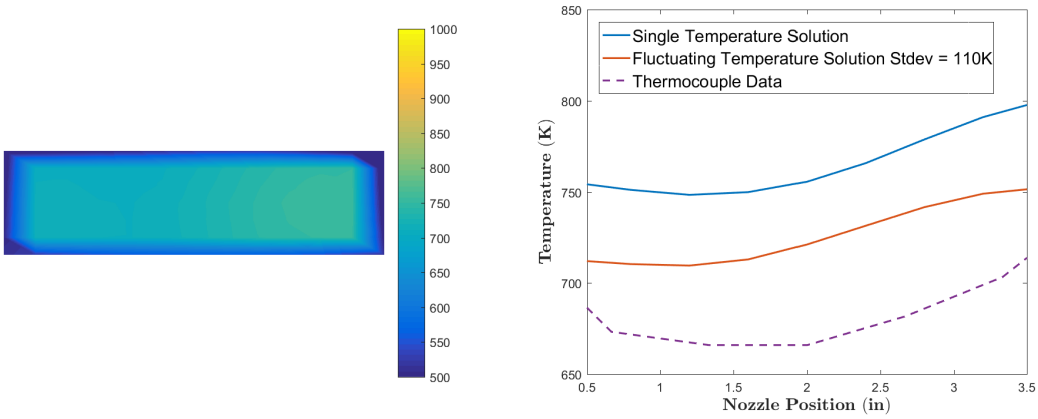

(a) **(b)**

Figure 66: (a) Solution set of the 4.25 in. downstream exhaust plane and (b) mean core temperature profile of the single temperature solution and fluctuating temperature solution with standard deviation of 110 K compared with the thermocouple data.

the HT algorithm is employed again. For the second implementation for the fluctuating temperature HT algorithm, the solution is initialized with the previous results and again a lower mean temperature solution is reached due to the higher standard deviation value. The core temperatures of the three solution sets are shown in Figure 68. Upon further iterations, the minimum Bhattacharyya distance specifies the same standard deviation.

This strategy is now applied to each of the exhaust planes. The more turbulent cases require multiple iterations to find the optimal standard deviation while the exhaust planes with less turbulence require only one. This parallels the case seen in the synthetic domain where the single mean temperature solution adequately represents the temporally averaged spectrum. At the exit plane, the Bhattacharyya distance from the SBFP imager at the exit plane indicates a standard deviation of 37 K as shown in Figure 69. This small standard deviation results in such a case where no large temperature impact is produced on the solution set by adding the fluctuations. While the temperatures are not largely affected by incorporating fluctuations, there

www.manaraa.com

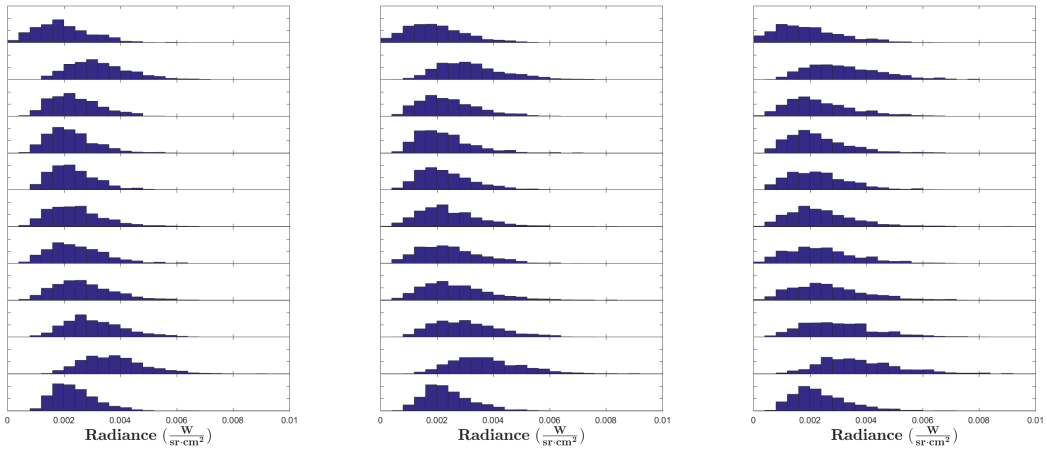

Figure 67: 4.25 in. exhaust plane histograms for fluctuating temperature about the fluctuating temperature solution for a standard deviation of (a) 120 K, $D_B = 0.0171$ (b) 130 K, $D_B = 0.0101$ (c) 140 K, $D_B = 0.0141$.

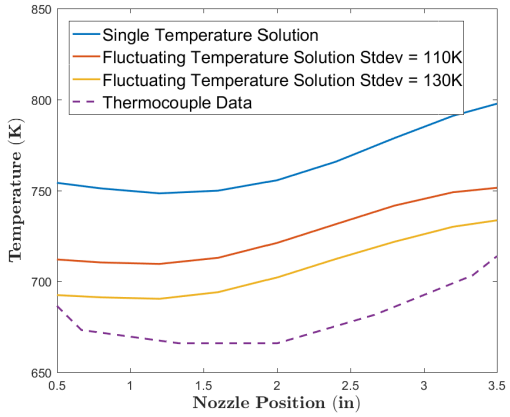

Figure 68: 4.25 in. exhaust plane mean core temperature profiles of the single temperature solution and fluctuating temperature solution with standard deviation of 110 K and 130 K compared with the thermocouple data..

is still an impact on the temperature profile. Where the temperatures and concentrations are fluctuating throughout, a slightly different minimum is found in the HT algorithm. Because the distribution is random and the number of samples is small, each solution set run has a variation that ranges from 5 to 10 K.

www.manaraa.com

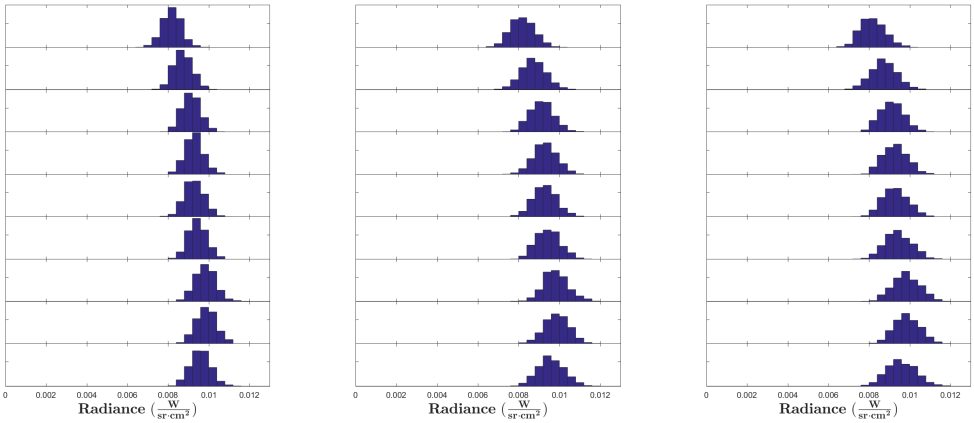

(a) **(b)** **(c)**

Figure 69: Exit plane histograms for fluctuating temperature about the single temperature solution for a standard deviation of (a) 30 K, $D_B = 0.0210$ (b) 37 K, $D_B = 0.0098$ (c) 40 K, $D_B = 0.0116$.

8.8 Exhaust Planes With Temperature Fluctuations

For each exhaust plane with corresponding thermocouple measurements, this iterative turbulent HT solution is used. The more turbulent planes further downstream in the flow are impacted more. The average core temperatures of the solution set produced using the turbulent HT algorithms are shown in (a) and their residuals are shown in (b) of Figure 70. Largely, the solution sets now agree well with the thermocouple data to within ± 35 K for the mean core temperatures. All the solution sets are shown in Figure 71.

8.9 Summary of Turbulence and Hyperspectral Tomography

The solution sets resulting from adding in turbulent effects agree within ± 35 K compared to the thermocouple data. For most applications of this approach, the thermocouple measurements would not be an available data set. The approach described enables a tomographic solution of turbulent flows to be generated from only remote sensing with no *a priori* knowledge of the actual mean temperature. While

www.manaraa.com

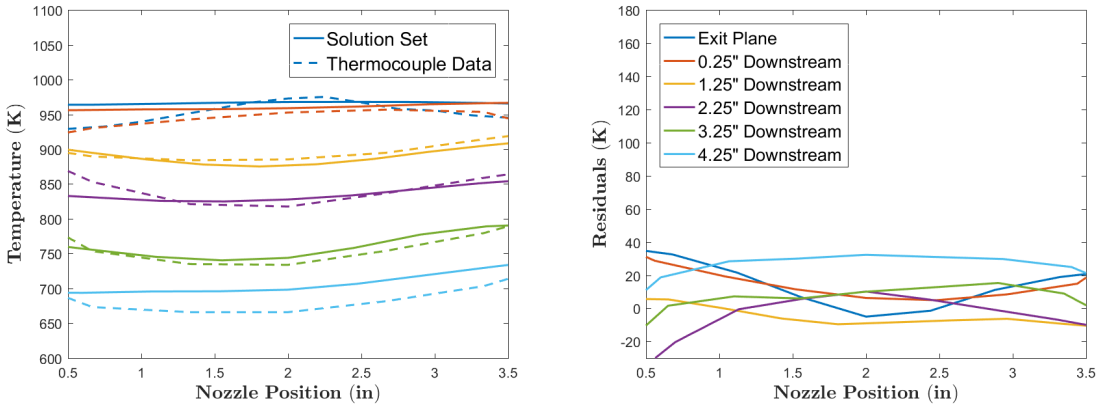

Figure 70: (a) The average core temperature values of the solution set using the turbulent HT algorithm and collected thermocouple data for the six exhaust planes and (b) the residuals for each plane.

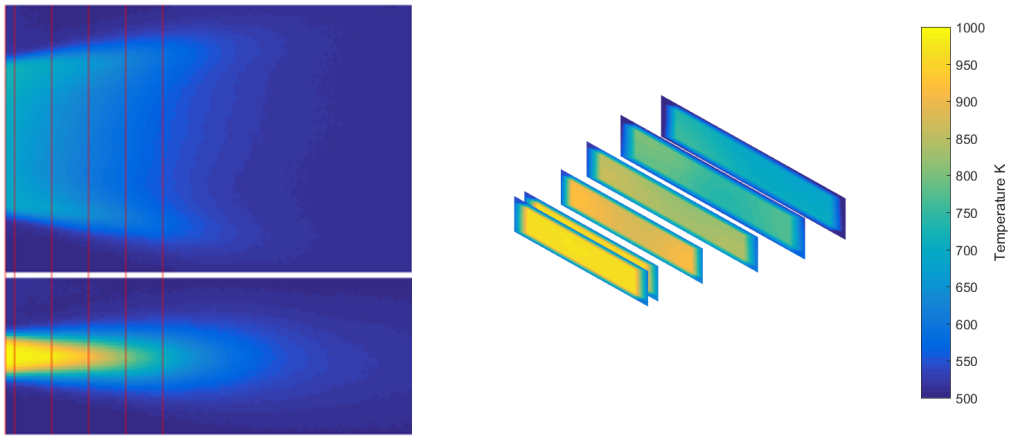

Figure 71: Temperature solution sets for six exhaust planes using the fluctuating HT algorithm at (1) the exit plane and (2) 0.25, (3) 1.25, (4) 2.25, (5) 3.25, and (6) 4.25 in. downstream from exit plane.

in this case the turbulence was measured using a separate infrared imager, data collected with the HSI can provide information about the turbulent fluctuations. The SBFP imager was a better choice in this case due to the limiting band-pass filter that isolated the fluctuations due to CO_2 giving a very good signal-to-noise ratio for the measurement. Further refinement of this technique could be applied in the selection of the standard deviation. For this case, a single standard deviation was used for

www.manaraa.com

each exhaust plane by using the mean Bhattacharyya distance for all the histograms. Alternatively, the Bhattacharyya distance along each line of sight could be calculated to give a different standard deviation for each line of sight along one dimension.

www.manaraa.com

IX. Conclusion

Previous methods of combustion diagnostics of exhaust gases, *i.e.* determination of temperatures and species concentrations, were limited to intrusive and local measurement methods. These methods provide only single point or plane measurements throughout a turbulent flow. This presents difficulties where remote sensing is the only possible means of data collection or if the measurement of multiple planes is desired.

The IFTS HSI provides a dense data set that has been used for the first time to determine concentration of species and temperature of combustion byproducts throughout a turbulent exhaust flow. In order to determine these values, HSI data was collected from multiple aspects of a representative jet engine exhaust and calibrated against known radiation sources. These measured projections act as the solution to which the algorithm compares. A grid space was then generated for each plane in the exhaust flow field and the hyperspectral tomography algorithm was used. This process incorporates first principle modeling of short homogeneous paths based on spectroscopic databases in which the gases attenuate radiation and re-emit radiation based on their local temperature, pressure, and concentration of CO_2 and H_2O. Using a populated grid space of concentrations and temperatures, projections were computed to compare directly to measurements. The grid space was initialized to values of temperatures and concentrations that gave moderate approximations to the measured spectra and then the minimization algorithm was begun to converge to a solution. To determine how well the algorithm performed, local temperatures were measured using thermocouples. For exhaust planes near the exit plane, where turbulence was low, agreement was within other published results of $\pm 35\ K$. Where turbulence was high, the algorithm increasingly over-predicted the temperatures.

This disagreement resulted from the thermocouples measuring a mean tempera-

www.manaraa.com

ture while the IFTS HSI measured a mean spectrum. The fluctuations were modeled using a synthetic domain and shown to produce the same effect as was seen in the collected data. Isotropic turbulence was inserted into the HT algorithm in which the temperature in the domain fluctuates randomly about this local mean temperature. The projections were then computed for multiple instances in time and then averaged in a comparable way to averaging of multiple IFTS HSI scans. These fluctuations were performed at every iteration during the hyperspectral tomography. In order to determine the standard deviation for an exhaust planes fluctuation, an IR imager was used. The solution domain from the HT algorithm was fluctuated until the same radiance distribution was produced as that of the IR imager. This was iteratively done until the solution set, with the standard deviation used to produce it, matched the IR imager histogram best. This approach allowed for the reconstruction of the 3D temperature distribution of the jet turbine exhaust that agreed well with the collected thermocouple data for all exhaust planes.

This research is the first application of the HT algorithms to calibrated IFTS HSI data of a turbulent jet engine exhaust. Additionally, it allows for compensation for the effects that turbulence has on averaged HSI measurements. These developments are directly applicable to infrared scene rendering applications which affect aircraft survivability and susceptibility. Additionally, they provide the data set most directly comparable to CFD solutions and can therefore assist in evaluating approximations made in these codes.

Further research and applications include modifications of measurement techniques, different turbulent flows, and usage of the developed algorithms in CFD code. By selecting specific portions of the measurement spectrum using band-limiting filters, the SNR of the measurements could be increased and the calibration sources could be better adjusted to span the dynamic range. Adjusting the resolution of the

www.manaraa.com

instrument could be used as well to increase SNR depending on the gas being measured. The techniques shown here utilized the emission of CO_2 within the flow where the individual rotational-vibrational lines were not resolved and as such lowering the resolution would likely not impact algorithm performance. With H_2O, the lines were resolved and therefore the impact of lowered resolution would need to be explored.

A natural extension of these techniques is on a full-scale jet turbine. The longer path length through these flows will impact the optical depth and can in turn effect the algorithm performance. However, because this instrument spans H_2O and CO_2, a portion of the spectrum that has a lower optical depth could be selected to ensure algorithm effectiveness.

While this research focused on developing the temperature and concentration domain that is directly comparable to CFD, the techniques for computing the radiative transfer through this domain was a necessary step. These techniques provide a first principles approach to rendering infrared scenes from CFD solutions and could be implemented into CFD code and infrared rendering codes.

www.manaraa.com

Bibliography

1. Alexander Berk, Patrick Conforti, Rosemary Kennett, Timothy Perkins, Frederick Hawes, and Jeannette Van Den Bosch. MODTRAN 6: A major upgrade of the MODTRAN radiative transfer code. *Proc. SPIE Vol. 9088*, page 90880H, 2014.

2. Peter F Bernath. *Spectra of atoms and molecules*. Oxford university press, 2015.

3. Anil Bhattacharyya. On a measure of divergence between two statistical populations defined by their probability distributions. *Bull. Calcutta Math. Soc.*, 35:99–109, 1943.

4. S J Bowen. Hyperspectral Imaging of a Turbine Engine Exhaust Plume to Determine Radiance, Temperature, and Concentration Spatial Distributions. *Thesis, Air Force Inst. Technol.*, pages 1–20, 2012.

5. L C Burmeister. *Convective Heat Transfer*. Wiley-Interscience publication. Wiley, 1993.

6. M Chamberland, V Farley, J Giroux, A Villemaire, J F Legault, and K Schwantes. Development and testing of a hyper-spectral imaging instrument for standoff chemical detection. *Chem. Biol. Standoff Detect. Ii*, 5584(418):135–143\r284, 2004.

7. S A Clough, M W Shephard, E J Mlawer, J S Delamere, M J Iacono, K Cady-Pereira, S Boukabara, and P D Brown. Atmospheric radiative transfer modeling: a summary of the AER codes. *J. Quant. Spectrosc. Radiat. Transf.*, 91(2):233–244, 2005.

www.manaraa.com

8. Xiaobing Dai, Xiangyan Liu, and Li Liu. Development and testing of an image-guided FT-IR instrument for field spectroscopy. *Proc. SPIE Vol. 9611*, page 961119, 2015.

9. Michael Theodore Eismann. Hyperspectral remote sensing. SPIE Bellingham, 2012.

10. C A J Fletcher. *Computational Techniques for Fluid Dynamics 2: Specific Techniques for Different Flow Categories*. Scientific Computation. Springer Berlin Heidelberg, 2012.

11. Marc-André Gagnon, Jean-philippe Gagnon, Pierre Tremblay, Simon Savary, Vincent Farley, Philippe Lagueux, and Martin Chamberland. Infrared hyperspectral imaging of ship plumes. *SPIE Newsroom*, (C):10–12, 2016.

12. Marc-Andre Gagnon, Pierre Tremblay, Simon Savary, Marc Duval, Vincent Farley, and Martin Chamberland. Airborne Midwave and Longwave Infrared Hyperspectral Imaging of Gases. *Proc. SPIE*, 9106:91060C, 2014.

13. Kevin C Gross, Chris Borel, Allen White, Stephen Sakai, Rebecca DeVasher, and Glen P Perram. First imaging Fourier-transform spectral measurements of detonation in an internal combustion engine. *Proc. SPIE*, 7812, 2010.

14. Kevin C. Gross, Kenneth C. Bradley, and Glen P. Perram. Remote identification and quantification of industrial smokestack effluents via imaging fourier-transform spectroscopy. *Environ. Sci. Technol.*, 44(24):9390–9397, 2010.

15. Jacob L Harley, August J Rolling, Charles F Wisniewski, and Kevin C Gross. Spatially resolved infrared spectra of F109 turbofan exhaust. *Proc. SPIE*, 8354(937):1–10, 2012.

www.manaraa.com

16. Katharina Kohse-Höinghaus and Jay Barker Jeffries. Applied combustion diagnostics. 2002.

17. Lin Ma and Weiwei Cai. Numerical investigation of hyperspectral tomography for simultaneous temperature and concentration imaging. *Appl. Opt.*, 47(21):3751–3759, 2008.

18. Lin Ma, Weiwei Cai, Andrew W Caswell, Thilo Kraetschmer, Scott T Sanders, Sukesh Roy, and James R Gord. Tomographic imaging of temperature and chemical species based on hyperspectral absorption spectroscopy. *Opt. Express*, 17(10):8602–8613, 2009.

19. Lin Ma, Xuesong Li, Scott T Sanders, Andrew W Caswell, Sukesh Roy, David H Plemmons, and James R Gord. 50-kHz-rate 2D imaging of temperature and H2O concentration at the exhaust plane of a J85 engine using hyperspectral tomography. *Opt. Express*, 21(1):1152–62, 2013.

20. Michael F. Modest. *Radiative Heat Transfer*. Elsevier Science, San Diego, third edition, 2013.

21. Elizabeth a. Moore, Kevin C. Gross, Spencer J. Bowen, Glen P. Perram, Martin Chamberland, Vincent Farley, Jean-Philippe Gagnon, Philippe Lagueux, and Andre Villemaire. Characterizing and overcoming spectral artifacts in imaging Fourier-transform spectroscopy of turbulent exhaust plumes. *Proc. SPIE*, 1(937):730416–730416–12, 2009.

22. J J Olivero and R L Longbothum. Empirical fits to the Voigt line width: A brief review. *J. Quant. Spectrosc. Radiat. Transf.*, 17(2):233–236, 1977.

23. M R Rhoby, D L Blunck, and K C Gross. Mid-IR hyperspectral imaging of laminar flames for 2-D scalar values. *Opt.Express*, 2014.

www.manaraa.com

24. L S Rothman, D Jacquemart, A Barbe, D Chris Benner, M Birk, L R Brown, M R Carleer, C Chackerian, K Chance, L H Coudert, V Dana, V M Devi, J.-M. Flaud, R R Gamache, A Goldman, J.-M. Hartmann, K W Jucks, A G Maki, J.-Y. Mandin, S T Massie, J Orphal, A Perrin, C P Rinsland, M A H Smith, J Tennyson, R N Tolchenov, R A Toth, J Vander Auwera, P Varanasi, and G Wagner. The HITRAN 2004 molecular spectroscopic database. *J. Quant. Spectrosc. Radiat. Transf.*, 96(2):139–204, 2005.

25. L.S. Rothman and I.E. Gordon. The HITRAN2012 molecular spectroscopic database. *J. Quant. Spectrosc. Radiat. Transf.*, 130:4–50, nov 2013.

26. L.S. Rothman, I.E. Gordon, R.J. Barber, H. Dothe, R.R. Gamache, A. Goldman, V.I. Perevalov, S.A. Tashkun, and J. Tennyson. HITEMP, the high-temperature molecular spectroscopic database. *J. Quant. Spectrosc. Radiat. Transf.*, 111(15):2139–2150, oct 2010.

27. Klaus Schaefer and Rainer Haus. Remote sensing and gas analysis of aircraft exhausts using FTIR emission spectroscopy. *Proc. SPIE Vol. 2506*, pages 62–71, 1995.

28. Klaus Schafer, Carsten Jahn, Selina Utzig, Edgar Flores-Jardines, Roland Harig, and Peter Rusch. Remote measurement of the plume shape of aircraft exhausts at airports by passive FTIR spectrometry. *Proc. SPIE - Int. Soc. Opt. Eng.*, 5571:334–344, 2004.

29. F. S. Simmons, H. Y. Yamada, and C.B. Arnold. Measurmentof temperature profiles in hot gases by emission-absorption spectroscopy. *Tech. Rep. CR-72491, NASA*, 1969.

www.manaraa.com

30. Peter R. Solomon, Philip E. Best, Robert M. Carangelo, James R. Markham, Po-Liang Chien, Robert J. Santoro, and Hratch G. Semerjian. FT-IR emission/-transmission spectroscopy for in situ combustion diagnostics. *Symp. Combust.*, 21(1):1763–1771, jan 1988.

31. S.A. Tashkun and V.I. Perevalov. CDSD-4000: High-resolution, high-temperature carbon dioxide spectroscopic databank. *J. Quant. Spectrosc. Radiat. Transf.*, 112(9):1403–1410, jun 2011.

32. Jack R White. Aircraft infrared principles, signatures, threats, and countermeasures. Technical report, 2012.

33. David C Wilcox. *Basic fluid mechanics*. DCW industries, 2000.

www.manaraa.com

Appendix

Acronyms

Acronym	Description
AFIT	Air Force Institute of Technology
CDSD	Carbon Dioxide Spectroscopic Databank
CFD	Computational Fluid Dynamics
FPA	Focal Plane Array
HSI	Hyperspectral Imager
HT	Hyperspectral Tomography
IFTS	Infrared Fourier Transform Spectrometer
InSb	Indium Antimonide
IR	Infrared
LWIR	Long-Wave Infrared
MWIR	Mid-wave Infrared
NAWCWD	Naval Air Warfare Center Weapons Division
OPD	Optical Path Difference
RTC	Real-Time-CHAMP
SBFP	Santa Barbara Focal Plane
SNR	Signal to Noise Ratio
TDI	Test Devices Inc.
ZPD	Zero Path Difference

www.manaraa.com

REPORT DOCUMENTATION PAGE

Form Approved
OMB No. 0704–0188

The public reporting burden for this collection of information is estimated to average 1 hour per response, including the time for reviewing instructions, searching existing data sources, gathering and maintaining the data needed, and completing and reviewing the collection of information. Send comments regarding this burden estimate or any other aspect of this collection of information, including suggestions for reducing this burden to Department of Defense, Washington Headquarters Services, Directorate for Information Operations and Reports (0704–0188), 1215 Jefferson Davis Highway, Suite 1204, Arlington, VA 22202–4302. Respondents should be aware that notwithstanding any other provision of law, no person shall be subject to any penalty for failing to comply with a collection of information if it does not display a currently valid OMB control number. **PLEASE DO NOT RETURN YOUR FORM TO THE ABOVE ADDRESS.**

1. REPORT DATE *(DD–MM–YYYY)*	2. REPORT TYPE	3. DATES COVERED *(From — To)*
07–17–2018	PhD Dissertation	June 2016 — September 2018

4. TITLE AND SUBTITLE

RECONSTRUCTION OF THE 3D TEMPERATURE AND SPECIES CONCENTRATION SPATIAL DISTRIBUTION OF A JET ENGINE EXHAUST PLUME USING AN INFRARED FOURIER TRANSFORM SPECTROMETER HYPERSPECTRAL IMAGER

5a. CONTRACT NUMBER

5b. GRANT NUMBER

5c. PROGRAM ELEMENT NUMBER

6. AUTHOR(S)

Mason D. Paulec

5d. PROJECT NUMBER

5e. TASK NUMBER

5f. WORK UNIT NUMBER

7. PERFORMING ORGANIZATION NAME(S) AND ADDRESS(ES)

Air Force Institute of Technology
Graduate School of Engineering and Management (AFIT/EN)
2950 Hobson Way
WPAFB OH 45433-7765

8. PERFORMING ORGANIZATION REPORT NUMBER

AFIT-ENP-DS-18-S-025

9. SPONSORING / MONITORING AGENCY NAME(S) AND ADDRESS(ES)

Department of Engineering Physics
2950 Hobson Way
WPAFB OH 45433-7765
DSN 271-0690, COMM 937-255-3636
Email: mason.paulec@afit.edu

10. SPONSOR/MONITOR'S ACRONYM(S)

11. SPONSOR/MONITOR'S REPORT NUMBER(S)

12. DISTRIBUTION / AVAILABILITY STATEMENT

DISTRIBUTION STATEMENT A:
APPROVED FOR PUBLIC RELEASE; DISTRIBUTION UNLIMITED.

13. SUPPLEMENTARY NOTES

14. ABSTRACT

Using an infrared Fourier transform spectrometer (IFTS) hyperspectral imager (HSI), measurements where made of a turbulent exhaust plume. Using these data, hyperspectral tomography algorithms were used to solve for the 3D temperature and species concentration spatial distributions. Turbulent effects were incorporated into the algorithms and the resulting solutions were compared directly to thermocouple temperature data collected throughout this exhaust flow.

15. SUBJECT TERMS

infrared, hyperspectral, spectroscopy, tomography

16. SECURITY CLASSIFICATION OF:			17. LIMITATION OF ABSTRACT	18. NUMBER OF PAGES	19a. NAME OF RESPONSIBLE PERSON
a. REPORT	b. ABSTRACT	c. THIS PAGE			Mason D. Paulec, AFIT/ENP
U	U	U	U	131	19b. TELEPHONE NUMBER *(include area code)* (805) 989-3098; mason.paulec@navy.mil

Standard Form 298 (Rev. 8–98)
Prescribed by ANSI Std. Z39.18

www.manaraa.com